Integrated single photon sources:

Development to benchmarking

by

Nicola Montaut

A thesis submitted in partial fulfillment for the
degree of Doctor of Philosophy
at
Paderborn University

October 2019

Contents

Summary

Quantum optics is one of the most attractive fields today showing immense potential in global applications. The fundamental resource here, is a single photon, which is the quantised state of light. Several high quality sources have been developed using a spontaneous parametric down conversion (SPDC) process, however, an ideal SPDC source is far from being realised. Depending on the application, a trade-off in the quantum features must be introduced to successfully implement such sources.

In the first part of this dissertation, we present a ”plug-and-play” source of telecom wavelength heralded single photons developed on a periodically poled lithium niobate waveguide platform. The adopted fabrication and pigtailing protocols are discussed. Finally, the source is mounted in an alignment-free package and is designed to show desirable quantum properties, thus making it suitable for long distance applications. Classical and quantum characterisations are performed to benchmark the source quality. This device presents high stability and ease-of-use, together with quantum performances which exceed by far the packaged devices shown in literature. Owing to mature source engineering technology, a complete flexibility over a large range of PDC wavelengths is possible and by using a variety of filters, source properties can be tailored.

The second part of the thesis focuses on an efficient tool for characterisation of photon pairs generated through SPDC in the spatial and spectral degrees of freedom. We utilise compressive sensing (CS) and a time-of-flight spectrometer to demonstrate a proof-of-principle measurement to discretise high-dimensional states with billions of elements. We experimentally demonstrate the benefits of using CS as opposed to conventional methods. The simplicity and robustness of this technique opens the possibility of realising complex photonic states in quantum protocols.

Zusammenfassung

Die Quantenoptik ist eines der attraktivsten aktuellen Forschungsgebiete, das ein immenses Potenzial in globalen Anwendungen aufweist. Das grundlegende Element ist hier ein einzelnes Photon, der quantisierte Zustand des Lichts. Mehrere qualitativ hochwertige Einzelphotonen-Quellen, basierend auf einem Parametrische Fluoreszenz (SPDC)-Prozess wurden bereits entwickelt, eine ideale SPDC-Quelle ist jedoch noch lange nicht realisiert. Deshalb muss, je nach Anwendung, ein Kompromiss bezüglich den Quanteneigenschaften eingegangen werden, um solche Quellen erfolgreich zu implementieren.

Im ersten Teil dieser Dissertation stellen wir eine "Plug-and-Play"-Quelle für Einzelphotonen, sogenannte "heralded single photons" im Bereich der Telekom-Wellenlängen vor, die auf der Plattform von periodisch gepolten Lithiumniobat-Wellenleitern entwickelt wurden. Die angepassten Herstellungs- und Faserkopplungsverfahren werden diskutiert. Schließlich wird die Quelle in einem justagefreien Gehäuse montiert und so konzipiert, dass sie die gewünschten Quanteneigenschaften aufweist, wodurch sie für Anwendungen über große Entfernungen geeignet ist. Klassische und Quanten Charakterisierungen werden durchgeführt, um die Qualität der Quelle zu bewerten. Dieses Bauteil zeichnet sich durch hohe Stabilität und leichte Bedienbarkeit aus, in Kombination mit Quanten Eigenschaften, die weit über die in der Literatur gezeigten integrierten Bauelemente hinausgehen. Dank ausgereiften Optimierungstechniken ist eine hohe Flexibilität über einen großen Bereich von PDC-Wellenlängen möglich und durch den Einsatz verschiedener Filter können die Eigenschaften der Quelle zielgerichtet angepasst werden.

Der zweite Teil der Arbeit konzentriert sich auf eine effiziente Methode zur Charakterisierung von Photonenpaaren, die durch SPDC in den räumlichen und spektralen Freiheitsgraden erzeugt werden. Mit Hilfe von sogenanntem Compressive Sensing (CS) und einem Laufzeit-Spektrometer demonstrieren wir eine Proof-of-Principle-Messung zur Diskretisierung hochdimensionaler Zustände mit Milliarden von Elementen. Wir zeigen experimentell die Vorteile der Verwendung von CS im Vergleich zu herkömmlichen Methoden. Die Einfachheit und Robustheit dieser Technik eröffnet die Möglichkeit, komplexe photonische Zustände in Quantenprotokollen zu realisieren.

Part A.

High-efficiency fibre-pigtailed heralded source of single photons

Chapter 1

Introduction

Over the last few decades, quantum information technology (QIT) has gained a lot of attention in research communities [1, 2]. At its core, QIT deals with the manipulation of information into quantum resources to perform tasks that are deemed otherwise impossible in a classical context [3]. The promise of this technology is profound for future innovations such as in secure communication [4, 5], computing and simulation [3, 6–9], non-classical spectroscopy and imaging [10, 11] etc. The key conceptual block to QIT is the unique properties of quantum states, like superposition and entanglement. Several physical systems like trapped ions [12], nuclear spins and semiconductor circuits were exploited as tools to test the capabilities of QIT, however over time it was photons [5,13–15] that played the leading role.

Photons, the fundamental constituent of light, holds several inherent advantages over other particles: i) they propagate at extremely high speeds, ii) they can be easily transmitted through freespace and fibre optic networks [4,16,17] iii) they are inert to environmental noise and hence suffer from low losses and iv) they can be easily manipulated [18]. The basic building block of an optical QIT device is a ”single photon source” [19–22] that is capable of emitting a single photon on demand at any given time. An ideal source [23] will produce single photons with long lifetimes and that are completely indistinguishable with zero probability of multi-photon components. Realisation of such a source is extremely hard but several deserving candidates have emerged recently that have shown great potential in quantum experiments.

Practical single photon sources are divided into two:

1. a single quantum emitter that can be developed on several platforms like quantum dots [24–26], defect centres [27–30], nanowires [31, 32] etc.

2. a heralded photon source that exploits nonlinear quantum processes like spontaneous parametric down conversion (SPDC) [33–39] and four-wave mixing [40, 41].

In this work, we focus on SPDC-based sources to generate high quality quantum states of light. Here, low energy photon pairs are created from the interaction between a nonlinear medium and a high energy pump photon. For these sources, the generation of photons are probabilistic, rather than deterministic. This process was predicted in 1961 by Louisell *et al* [42], following which, in the year 1969, Klyshko and Zeldovic [43] experimentally demonstrated an SPDC-based source of quantum light. Burnham *et al* [33] in 1970 first reported the existence of correlations between the photon pairs emitted from an ammonium dihydrogen phosphate crystal. Since then, SPDC has been the central ingredient for a variety of quantum applications. SPDC is produced in several material platforms like microresonators [44, 45] and semiconductors [46, 47]; however, in dielectric media, the most common SPDC-based sources come in periodically poled bulk- (freespace) or waveguide- (integrated) material systems. When constructing a quantum source, this is one of the most critical choices to be made as the performance metrics vary significantly between the two.

Traditionally, SPDC-based single photon devices were built using bulk crystals, since freespace alignment of sources offer many advantages over integrated systems: a) the guiding medium is air, losses are minimal; b) freespace optical components are readily available; c) spatial and spectral properties can be easily manipulated and d) the alignment strategies are well understood. Generation of photon pairs at telecom wavelengths from periodically poled bulk crystals was initially attempted by Albota *et al* [48] to benchmark its performance for quantum optical communication systems. The overall design efficiency and photon generation rates reported were low, but it provided valuable insight to the challenges that need to be overcome such that quantum optical techniques can be considered as a viable solution for real-world applications. Several research groups began investigating various material systems to improve these metrics and optimise photon collection efficiencies. Ljunggren *et al* [49] first addressed the effect of focusing conditions of the input beam on the coupling efficiencies between photon pairs emitted from bulk sources and fibres under collinear emission conditions. Theoretical simulations suggested that by engineering the input mode with respect to the fibre modes, coupling efficiencies > 93 % can be achieved irrespective of the crystal length. Experimentally however, the pair coupling efficiency into a single-mode fibre reported was only 11 %. Similar studies on the importance of spatial mode matching and spectral mode selection for high efficiency sources were put forward by Castelleto *et al* [50], where they were able to experimentally improve their source efficiencies after significant post-processing.

So far, the best efficiency sources are obtained with bulk crystals; capable of producing high quality, non-degenerate, polarisation-entangled sources [51, 52]. However, bulk sources have serious drawbacks like lack of integrability and scalability, low photon pair generation rates, substantial space requirements and multimode outputs. A common method to assure good mode preparation for interference experiments in such sources is to use strong spatial and spectral filtering, at the cost of generation rates of useable photons. A more efficient method is the use of waveguides for optimal light guiding and high nonlinear conversion efficiencies achieved through large intensity optical confinement.

Waveguide-based sources have much to offer in terms of inherent spatial mode filtering [53], decorrelation of spatial and spectral degrees of freedom and increased source brightness. Apart from this, with mature fabrication techniques, photonic waveguides show the capability of high-level integration of multiple components on chip [54–56] and compatibility with existing fibre networks [57–60]. The highest waveguided SPDC efficiency of 85 % was seen in 2004, reported by U'Ren *et al* [37]. The source was realised through a type II SPDC interaction in a periodically poled potassium titanyl phosphate waveguide to produce 800 nm photons. The first promising efficiencies for sources operating in the telecom regime was obtained by Alibart *et al*, with efficiency of 38 % for a non-degenerate source at 1550 nm by heralding photons at 1310 nm wavelength [61]. The best configuration for telecom photons was achieved by Zavriyev *et al* in 2007 [62] by heralding the photons in the visible, where single photon detectors are more efficient. A list of sources and their relevant properties with respect to this thesis is shown in Table 4.2.

Here, we present a ”plug-and-play” photon pair source that is capable of producing telecom photons whose quantum properties can be tailored in the spectral domain by temperature tuning and photon indistinguishability by spectral filtering. The source is engineered on a periodically poled titanium-indiffused lithium niobate (Ti:PPLN) waveguide platform due to its inherently low losses and high nonlinearity. The fabricated device is completely free of bulk components; made possible by the use of fibre pigtails permanently attached at the input and output faces of the waveguide. Photon splitting, routing and filtering is also performed using commercial telecommunications components available in the market. By attaching a pumping laser at the input and single photon detectors at the output, the final alignment-free source package is extremely simple to use within or outside the lab for long distance quantum applications and proof-of-principle experiments.The resultant source shows high heralding efficiencies and brightness, only limited by the losses of the fibre-optical elements.

Organisation of Part A: Chapter 2 describes the theory behind nonlinear optical processes and source engineering strategies used within this part. A brief overview on spontaneous parametric down conversion (SPDC) and tools required to characterise SPDC sources are explained. In Chapter 3, we introduce the fabrication procedures and techniques we adopted to ensure best possible performance of the source. The classical and quantum characterisation outcomes are discussed in Chapter 4 along with a short comparison of state-of-the-art sources already presented by various research groups. Chapter 5 focuses on the need for filtering and its effects on the quantum characteristics of the source, namely heralding efficiency and spectral purity. The unsolved mysteries in terms of source performance and future outlook is presented in Chapter 6. Chapter 7 summarises the results and discussions in this part.

Chapter 2

Foundation

2.1. Nonlinearity in materials

Nonlinear optical processes heavily rely on the response of a material to an external electric field. When electromagnetic waves travel through a dielectric medium, their electric field induces a dipole moment to the atoms in the path of the radiation. In the case of linear optics, the induced dipole moment per unit volume, or polarisation ($\vec{P}(t)$) depends linearly upon the strength of the external electric field $\vec{E}(t)$ that can be described as

$$\vec{P}_L(t) = \epsilon_0 \chi^{(1)} \vec{E}(t) \tag{2.1}$$

where $\vec{E}(t)$ is given by $\vec{E}(t) = \vec{E}\exp(i\omega t)$, $\vec{E}$ is the time-dependant amplitude of the electric field component, $\chi^{(1)}$ is the first-order (or linear) electric susceptibility which is related to the refractive index (n) of the medium, $\chi^{(1)} = n^2 - 1$ and ϵ_0 is the vacuum electric permittivity. These linear effects occur as long as the external electric fields are of sufficiently low strengths, such that the system behaves like a harmonic oscillator. In this case, the input and output optical frequencies do not change on transmission, like in common optical components such as mirrors, lenses, waveplates etc. However, when high intensity electromagnetic radiation is introduced to certain materials, the induced polarisation no longer follows a linear relationship, but a nonlinear one (given by a power series expansion) with the applied electric field $\vec{E}(t)$

$$\begin{aligned}\vec{P}(t) &= \epsilon_0(\chi^{(1)}\vec{E}(t) + \chi^{(2)}\vec{E}(t)\vec{E}(t) + \chi^{(3)}\vec{E}(t)\vec{E}(t)\vec{E}(t) + ... \\ &= \vec{P}_L(t) + \vec{P}_{NL}(t)\end{aligned} \tag{2.2}$$

$$\vec{P}_{NL}(t) = \epsilon_0(\chi^{(2)}\vec{E}(t)\vec{E}(t) + \chi^{(3)}\vec{E}(t)\vec{E}(t)\vec{E}(t) + ...) \tag{2.3}$$

The first term in Equation 2.2 corresponds to the linear polarisation shown in Equation 2.1. The rest of the terms contributes to the nonlinear polarisation $\vec{P}_{NL}(t)$ induced within the medium (See Equation 2.3). The quantites $\chi^{(2)}$ and $\chi^{(3)}$ are the second- and third-order nonlinear susceptibilities which causes interesting phenomena in nonlinear crystals.

In classical and quantum optics, second-order nonlinear materials, commonly referred to as $\chi^{(2)}$ materials, play an important role in frequency conversion processes. In this work, we exploit second harmonic (classical) and spontaneous parametric down conversion (quantum) processes in crystalline dielectric media, which are produced as a result of this effect. The third-order term is associated with third-harmonic generation, for e.g. Kerr effect, self-phase modulation etc. where there is an intensity dependent change in the refractive index of the material. Since higher-order χ processes are significantly less probable in $\chi^{(2)}$ materials like lithium niobate (optical material used as the active medium in our source), we neglect all the higher-order terms for further discussions.

Nonlinear processes in $\chi^{(2)}$ materials can be understood in more detail by considering a circumstance in which the incident optical field consists of two distinct frequency components given by

$$\vec{E}(t) = \vec{E}_1 \exp(i\omega_1 t) + \vec{E}_2 \exp(i\omega_2 t) + c.c. \tag{2.4}$$

where, E_1 and E_2 are the amplitudes of the interacting electric fields; ω_1 and ω_2 are their corresponding frequencies respectively. In some cases like second harmonic generation, ω_1 is equal ω_2 as shown in Figure 2.1. Considering only the second-order nonlinear response of the active material, the nonlinear polarisation term in Equation 2.3 becomes

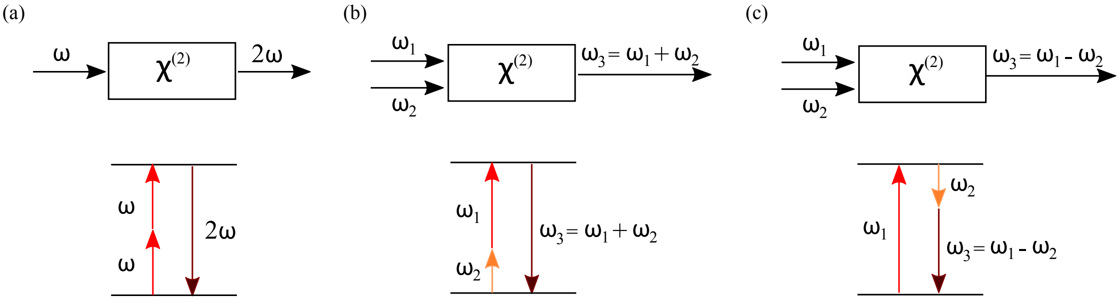

Figure 2.1.: Nonlinear frequency conversion processes: (a) second harmonic generation, (b) sum-frequency generation and (c) difference-frequency generation.

$$\begin{aligned}
\vec{P}^{(2)}(t) = {} & \epsilon_0 \chi^{(2)} \left[E_1^2 \exp(2i\omega_1 t) + c.c \right] && (SHG) \\
& + \epsilon_0 \chi^{(2)} \left[E_2^2 \exp(2i\omega_2 t) + c.c. \right] && (SHG) \\
& + \epsilon_0 \chi^{(2)} \left[2E_1 E_2 \exp(i(\omega_1 + \omega_2)t) + c.c. \right] && (SFG) \\
& + \epsilon_0 \chi^{(2)} \left[2E_1 E_2^* \exp(i(\omega_1 - \omega_2)t) + c.c. \right] && (DFG) \\
& + 2\epsilon_0 \chi^{(2)} [E_1 E_1^* + E_2 E_2^* + c.c.] && (OR)
\end{aligned} \tag{2.5}$$

We have labeled each part of the Equation by the name of the physical process that it describes, such as second harmonic generation (SHG) (See Figure 2.1 (a)), sum-frequency generation (SFG) (See Figure 2.1 (b)), difference-frequency generation (DFG) (See Figure 2.1 (c)) and optical rectification (OR).

Despite the presence of different non-zero frequency components in the expression for nonlinear polarisation, typically only one of the processes will occur with sufficient intensity. This is because every conversion process obeys a different phasematching rule; therefore under a defined set of conditions, only one phasematching rule is satisfied within the dielectric medium. Experimentally, different frequency conversion processes can be accessed by manipulating the polarisation of the input fields and by the orientation of the nonlinear crystal. All the afore-mentioned processes must fulfil the energy (Equation 2.6) and momentum (Equation 2.7) conservation equations,

$$\sum \hbar\omega_{input} = \sum \hbar\omega_{output} \tag{2.6}$$

$$\sum \hbar\vec{k}_{input} = \sum \hbar\vec{k}_{output} \tag{2.7}$$

where $\vec{k}$ is the momentum vector given by

$$\vec{k} = \frac{2\pi\vec{n}(\lambda)}{\lambda} = \frac{\omega\vec{n}(\omega)}{c} \tag{2.8}$$

λ is the wavelength of the photon and c is the vacuum speed of light.

Spontaneous parametric down conversion (SPDC), otherwise known as optical parametric generation is a special case of DFG, where a high energy input (pump) photon is destroyed within a nonlinear medium to generate a pair of lower energy daughter photons, namely signal and idler. The classical representation of SPDC generated photons to a DFG process can be understood from Figure 2.1(c) by taking the signal frequency as $\omega_s = \omega_2$ and idler frequency as $\omega_i = \omega_1 - \omega_2$. Both photons can have same- (degenerate) or different- (non-degenerate) energies depending on the operating conditions of the process. In Section 2.36 the SPDC process will be explained in detail, but first we take a look at the coupling equations of different fields in nonlinear materials.

2.2. Lithium niobate waveguides

Lithium niobate (LN) is an attractive material for integrated optics because of its excellent electro-optic and nonlinear optical properties. It is naturally birefringent and exhibits very strong photovoltaic and photorefractive effects. The crystallographic struc-

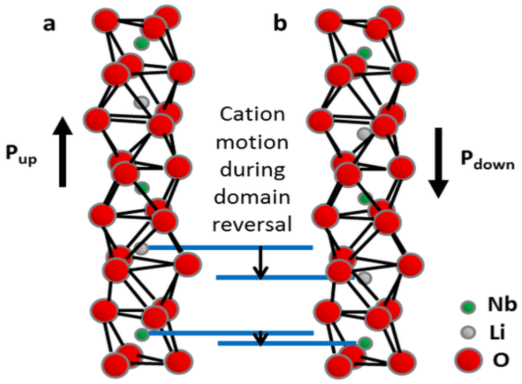

Figure 2.2.: The atomic structure of LN before (a) and after (b) the application of an external electric field [67]. The displacement along the crystallographic axis of the Nb (green) and Li (grey) atoms from their positions causes a reversal of the spontaneous polarisation.

ture of LN consists of planar layers of oxygen atoms forming a centrosymmetric array. The octahedral interstices formed are one-third filled by lithium atoms, one-third filled by niobium atoms and one-third vacant. This causes a slight displacement of Li and Nb from the centrosymmetric position relative to the oxygen octahedral along the c-axis resulting in a spontaneous polarisation along this direction as shown in Figure 2.2 a.

Figure 2.2 a) shows the crystallographic structure of lithium niobate with its spontaneous polarisation along the $+c$ axis. Being ferroelectric, it is possible to reverse this spontaneous polarisation by the application of an electric field as (described in Section 2.3) shown in Figure 2.2 b), a method commonly referred to as periodic poling. By engineering the poling structures, various interactions can be exploited to develop highly tunable nonlinear devices.

Fabrication of waveguides in LN is a primary requisite for its application in the field of integrated optics. Waveguides provide confinement to electromagnetic waves in one- or two- dimensions thereby enabling the transmission of light to long distances with minimal losses. Apart from this, waveguides also provide a medium for large intensity confinement resulting in high efficiencies for a variety of frequency conversion processes. In LN, waveguides are commonly introduced into the substrate either by an indiffusion of a high refractive index material or by a proton exchange method. In this work, we use titanium indiffused waveguides in LN to produce telecom photons by exploiting a type II SPDC process. The fabrication methodology for these waveguides are extremely mature resulting in robust and reliable structures. These waveguides can guide both - TE and TM polarisations with very low propagation losses, thereby making them an excellent candidate for quantum processes.

2.2.1. Waveguide model - indiffused structures

Due to the high versatility of LN, tremendous research has been conducted to induce localised changes in its optical properties. Literature reveals much investigations being performed by the indiffusion of a variety of metals like Ti [68–72], Mg [73–76], Ni [77, 78], Zn [79–81], Cr [82, 83], V [84, 85], Hf [86–88] and In [89, 90] into LN. One of the most desirable requirements was to produce a light-guiding medium or a ”waveguide” by introducing a small change in the refractive index of the substrate. We study the local indiffusion of titanium into a LN crystal to form channel (Ti:LN) waveguides on the surface of the substrate. This method has received much attention since 1974 [91] because Ti incorporation yields a good light confinement with sufficiently large increase to both ordinary and extraordinary refractive indices.

Ti waveguides in LN are fabricated by depositing a Ti layer of a certain width ($w_{Ti}(x)$) and thickness ($\tau_{Ti}(y)$) on the surface of the substrate. This forms a finite Ti reservoir along the x- and y- directions, which on indiffusion, forms a waveguiding structure of higher refractive index than the substrate. Considering the surface concentration of Ti to be c_0 and the diffusion time to be t, the concentration profile of Ti after in-diffusion ($c_{Ti}(x, y, t)$) obeys the Fick's laws [92] and hence follows a two-dimensional diffusion equation written as

$$\frac{\partial c_{Ti}(x,y,t)}{\partial t} = \mathcal{D}_x \frac{\partial^2 c_{Ti}(x,y,t)}{\partial x^2} + \mathcal{D}_y \frac{\partial^2 c_{Ti}(x,y,t)}{\partial y^2} \tag{2.9}$$

where $\mathcal{D}_x$ and $\mathcal{D}_y$ are the diffusivities of Ti in LN given by $\mathcal{D}_{x/y} = \mathcal{D}_{x/y,0} \exp(-\mathcal{T}_0/\mathcal{T})$, $\mathcal{T}$ is the absolute temperature, $\mathcal{T}_0$ is the temperature related to the activation energy of the diffusion process and $c_{Ti}(x, y, t) = c_0 f(x, t)g(y, t)$. The solution for $f(x, t)$ and $g(y, t)$ for long diffusion times can be obtained from Equation 2.9 [69, 92] as

$$\begin{aligned} f(x) &= \frac{1}{2}\left[\operatorname{erf}\left(\frac{x + w_{Ti}}{d_x}\right) + \operatorname{erf}\left(\frac{x - w_{Ti}}{d_x}\right)\right] \\ g(y) &= \exp\left(-\frac{y^2}{d_y^2}\right) \end{aligned} \tag{2.10}$$

where d_x and d_y are the diffusion lengths along the x- and y- directions respectively. The total Ti-concentration (after indiffusion) per unit length along the propagation direction is given by an integration of Equation 2.10, $\int\int c_{Ti}(x, y, t)\ dxdy = \sqrt{\pi} c_0 d_y w_{Ti}/2$ and c_0 is given by $c_0 = 2\rho_{Ti}\tau_{Ti}/(\sqrt{\pi} d_y)$, where ρ_{Ti} is the bulk density of titanium [93].

The principle behind Ti:LN waveguide formation lies in the localised increase of the refractive index, $\delta n_i(\lambda, c_{Ti})$, due to the indiffusion process of Ti. The resultant refractive index of the waveguide $n_i(\lambda, c_{Ti})$ can be written as the sum of the bulk refractive index $n_{B,i}(\lambda)$ and the corresponding localised change due to indiffusion.

$$n_i(\lambda, c_{Ti}) = n_{B,i}(\lambda) + \delta n_i(\lambda, c_{Ti}) \tag{2.11}$$

where $\delta n_i(\lambda, c_{Ti})$ depends on the dispersive properties and the Ti-concentration profile of the waveguide. The subscript i stands for the two guided polarisations - TE (ordinary (o)) and TM (extraordinary (e)). This index change was modelled as a function of wavelength (λ) and concentration ($c_{Ti}(x, y)$) as follows:

$$\begin{aligned} \delta n_e &= \frac{0.839\ \lambda^2}{\lambda^2 - 0.0645}\ V_e\ c_{Ti}(x, y) \\ \delta n_o &= \frac{0.8\ \lambda^2}{\lambda^2 - 0.08066}\ [V_o\ c_{Ti}(x, y)]^{0.55} \end{aligned} \tag{2.12}$$

where V_e and V_o was experimentally determined to be $V_e = 1.2 \times 10^{-23}$ cm^3 and $V_o = 1.3 \times 10^{-25}$ cm^3 [93–95]. From Equation 2.12, we see that on indiffusion, the change in the refractive index in the extraordinary polarisation is linear and the ordinary one follows a power law with a power of 0.55. Figure 2.3 published in Reference [95] shows the trend followed by the refractive indices on increasing Ti-concentration.

Next, we study the guided spatial mode distributions within the waveguide. Using Maxwell's Equations, we described the electric field of an electromagnetic wave in Equation 2.17 given by $\vec{E}_j(\vec{r}, t) = E_j(z)\vec{\mathcal{E}}_j(x, y) \exp[i(\omega_j t - (\vec{k}_j \vec{r})]$. Considering that we have a lossless medium (which is approximately the case in our waveguides) and that Ti-indiffused structures form weakly guiding structures, we can restrict the propagation of em-waves to the z-direction with a time-invariant electric field,

$$\vec{E}(x, y, z) = \vec{\mathcal{E}}(x, y)\ \exp(-ik_{j,z}z) + c.c. \tag{2.13}$$

where $k_{j,z}$ is the propagation constant of the guided modes in the z-direction, sometimes referred to as $\beta_{j,z}$. Similarly the magnetic field is given by

$$\vec{H}(x, y, z) = \vec{\mathcal{H}}(x, y)\ \exp(-ik_{j,z}z) + c.c. \tag{2.14}$$

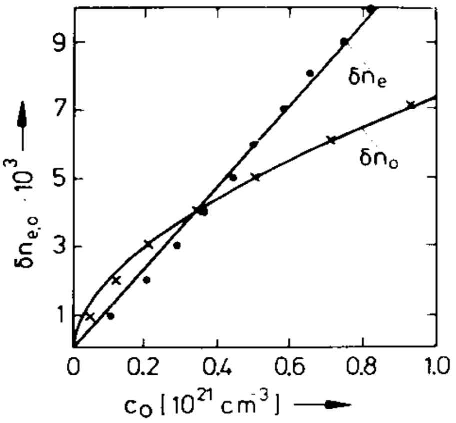

Figure 2.3.: a) Experimental results showing the dependance of ordinary (x marks) and extraordinary (points) refractive index on the Ti-concentration (here, $c_o = c_{Ti}$). Calculated values from Equation 2.12 are shown in solid lines [95].

Since the Ti-diffused profile does not change along the propagation direction, we have $\partial\vec{\mathcal{E}}(x,y)/\partial z = \partial\vec{\mathcal{H}}(x,y)/\partial z = 0$. Due to our waveguide model, we get quasi-transverse electric (qTE) and quasi-transverse magnetic (qTM) terms [95,96] by inserting Equation 2.13 - 2.14 to the Maxwell's Equations given by

$$\begin{aligned} \text{qTE}: \quad & \left[\frac{\partial^2}{\partial x^2} + \frac{\partial^2}{\partial y^2} + k_0^2(n_{B,o}^2 - n_{eff,o}^2)\right]\mathcal{E}_x = 0 \\ \text{qTM}: \quad & \left[\frac{\partial^2}{\partial x^2} + \frac{n_{B,e}^2}{n_{B,o}^2}\frac{\partial^2}{\partial y^2} + k_0^2(n_{B,e}^2 - n_{eff,e}^2)\right]\mathcal{H}_x = 0 \end{aligned} \tag{2.15}$$

By using mode-solvers like RSoft, we solve for these qTE and qTM modes using finite element method (FEM) to determine the guided modes in a waveguide under a set of fabrication parameters. In the rest of the thesis, we refer to the qTE and qTM modes as TE and TM modes respectively.

2.2.2. Coupled wave equations

The coupled wave equations are used to analyse how electromagnetic fields interact in a nonlinear environment. The classical representation of DFG and SPDC processes are similar, hence for simplicity a DFG interaction is considered to express the coupled-wave equations (any deviation from the two is outlined). Using Maxwell's Equations, we can derive the following nonlinear wave equation for a dispersionless medium

$$-\frac{d^2}{d\vec{r}^2}\vec{E}(\vec{r},t) + \frac{\epsilon}{c^2}\frac{\partial^2}{\partial t^2}\vec{E}(\vec{r},t) = -\frac{4\pi}{c^2}\frac{\partial^2}{\partial t^2}\vec{P}_{NL}(t) \tag{2.16}$$

So far, for simplicity, we have considered only the effect caused by the temporal evolution of an electric field (See Equation 2.4). However, $\vec{E}(\vec{r},t)$ in Equation 2.16 requires a full description of $\vec{E}$ which can be obtained after considering the spatial evolution of the field as well. The expression for the electric field is re-written as

$$\vec{E}_j(\vec{r},t) = E_j(\hat{z})\vec{\mathcal{E}}_j(x,y)\exp[i(\omega_j t - \vec{k}_j\vec{r}] + c.c. \tag{2.17}$$

where the subscript, $j = 1, 2, 3, ...$ is used as a notation for the interacting fields, $\vec{r}$ is the vector describing the spatial component, $\vec{\mathcal{E}}_j(x,y)\exp(-i(\vec{k}_j\vec{r}))$ is the spatial mode distribution of the field in the medium, $\exp(i\omega_j t)$ is the temporal evolution of the field and $E_j(z)$ is the space-dependent electric field amplitude for a field propagating along the z direction. $\vec{k}_j$ is the wave-vector of the propagating field (See Equation 2.8) described as $\vec{k}_j(\omega_j) = \frac{\omega_j}{c}\vec{n}_j(\omega_j)$ where, $\vec{n}(\omega)$ is the frequency-dependent refractive index of the medium. As shown in Section 2.1, this k-vector has a crucial role to play in frequency conversion processes, since it forms the basis of momentum conservation of the different interacting fields in an optical medium. The momentum conservation for three interacting fields (See Figure 2.1) is expressed as

$$\hbar[\vec{k}_1(\omega_1) - \vec{k}_2(\omega_2) - \vec{k}_3(\omega_3)] = 0 \tag{2.18}$$

where $\vec{k}_{1,2}(\omega_{1,2})$ are the input k-vectors and $\vec{k}_3(\omega_3)$ is the output k-vector for DFG (in SPDC, $\vec{k}_1(\omega_1)$ is the input k-vector and $\vec{k}_{2,3}(\omega_{2,3})$ are the output k-vectors).

The polarisation term ($\vec{P}(t)$) is the same as shown in Equation 2.5 (DFG). Using the definition for the field vectors in Equation 2.17, and by restricting the propagation of the jth field in the z direction (collinear propagation of all fields like in waveguides), the amplitude of the nonlinear polarisation for each field is dependent on the field amplitudes of the other fields. The amplitudes of the polarisation terms become

$$P_1(z,t) = \epsilon_0\chi^{(2)}E_2(z)E_3(z)\mathcal{E}_2(x,y)\mathcal{E}_3(x,y)\exp[i(\omega_1 t - (k_2+k_3)z] + c.c. \tag{2.19}$$

$$P_2(z,t) = \epsilon_0\chi^{(2)}E_1(z)E_3^*(z)\mathcal{E}_1(x,y)\mathcal{E}_3(x,y)\exp[i(\omega_2 t - (k_3-k_1)z] + c.c. \tag{2.20}$$

$$P_3(z,t) = \epsilon_0\chi^{(2)}E_1(z)E_2^*(z)\mathcal{E}_1(x,y)\mathcal{E}_2(x,y)\exp[i(\omega_3 t - (k_1-k_2)z] + c.c. \tag{2.21}$$

When the active medium (e.g. in lithium niobate) shows normal dispersion effects on the interacting fields, meaning when $\chi^{(2)}_{ijk}$ does not depend on the interacting frequencies, we use the tensor

$$d_{ijk} = \frac{1}{2}\chi^{(2)}_{ijk} \tag{2.22}$$

Here, d_{ijk} is a tensor matrix representing the (lack of) symmetry of the crystalline nonlinear material and the polarisation-dependent parametric interaction. Dependent on the type of interaction in the optical medium, the d_{ijk} matrix is reduced to a set of specific components called d_{eff} which acts as the effective nonlinear optical coefficient of the process, given by $d_{eff} = 2/\pi d_{ijk}$. Hence, Equation 2.19 - 2.21 becomes

$$P_1(z,t) = 2\epsilon_0 d_{eff}E_2(z)E_3(z)\mathcal{E}_2(x,y)\mathcal{E}_3(x,y)\exp[i(\omega_1 t - (k_2+k_3)z] + c.c. \tag{2.23}$$

$$P_2(z,t) = 2\epsilon_0 d_{eff}E_1(z)E_3^*(z)\mathcal{E}_1(x,y)\mathcal{E}_3(x,y)\exp[i(\omega_2 t - (k_3-k_1)z] + c.c. \tag{2.24}$$

$$P_3(z,t) = 2\epsilon_0 d_{eff} E_1(z) E_2^*(z) \mathcal{E}_1(x,y) \mathcal{E}_2(x,y) \exp[i(\omega_3 t - (k_1 - k_2)z] + c.c. \tag{2.25}$$

By substituting Equation 2.23 - 2.25 into Equation 2.16 and by performing certain approximations (see Reference [63] for the whole description), we get the coupled amplitude equations for the three fields as

$$\begin{aligned}
\frac{\partial E_1(z)}{\partial z} &= -i\kappa_1 \vartheta^* E_2^*(z) E_3(z) \exp(-i\Delta k z) \\
\frac{\partial E_2(z)}{\partial z} &= -i\kappa_2 \vartheta^* E_3(z) E_1(z)^* \exp(-i\Delta k z) \\
\frac{\partial E_3(z)}{\partial z} &= -i\kappa_3 \vartheta E_1(z) E_2(z) \exp(-i\Delta k z)
\end{aligned} \tag{2.26}$$

where $\Delta k = k_1 - k_2 - k_3 = 2\pi\left(\frac{n_1}{\lambda_1} - \frac{n_2}{\lambda_2} - \frac{n_3}{\lambda_3}\right)$ is the phasematching term which equates to zero under perfect circumstances, ϑ is the overlap integral between the three fields and κ is the coupling constant given by

$$\kappa_j = \sqrt{\frac{8\pi^2 d_{eff}^2}{n_1 n_2 n_3 c \epsilon_0 \lambda_j^2}} \tag{2.27}$$

where $j = 1, 2, 3$ representing the different fields. Assuming that the interacting fields are normalised, the overlap integral ϑ is expressed as

$$\vartheta = \int\limits_{-\infty}^{\infty} \int\limits_{-\infty}^{\infty} \tilde{\mathcal{E}}_1(x,y) \tilde{\mathcal{E}}_2(x,y) \tilde{\mathcal{E}}_3(x,y) \; \mathrm{d}x\mathrm{d}y \tag{2.28}$$

which provides us with the area of overlap (A_{eff}) between the interacting fields given by $A_{eff} = \vartheta^{-2}$. These equations form the basis of guided wave optics and on incorporating the properties of the optical medium, we can tailor the nonlinear optical responses through device engineering.

2.3. Quasi-phasematching

As shown in Equation 2.8, the wave vector for each field is not a constant due to the dispersion effects in dielectric materials. This results in a residual phase mismatch between the interacting fields in a DFG process given by $\Delta k_{DFG} = k(\omega_1) - k(\omega_2) - k(\omega_1 - \omega_2)$ from which we can determine the phase relation of a SPDC process,

$$\Delta k_{SPDC} = k(\omega_p) - k(\omega_s) - k(\omega_i) \neq 0 \tag{2.29}$$

In order to compensate for the phase mismatch in nonlinear optical materials, a process known as quasi-phasematching is introduced. This method can be implemented on ferroelectric materials that already have an orientation of spontaneous polarisation (along the crystallographic (c or z) axis) which can be periodically inverted on the application of external electric fields. This applied field depends on the coercive field of the crystal and is usually of the order of a few kV. The periodic inversion of the c axis causes a

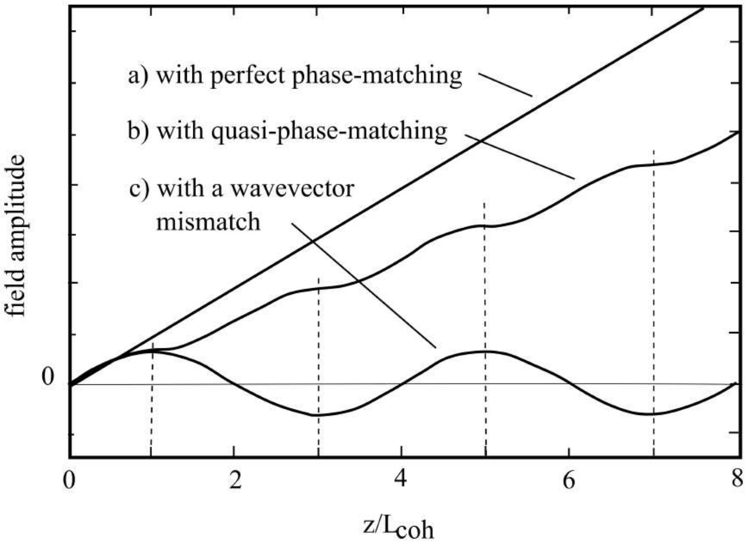

Figure 2.4.: The plot [64] shows the amplitude of the generated field under three conditions: a) with perfect phasematching, there is a linear increase in the output field with propagation length, b) with quasi-phasematching, there is a slower rise in the generated field strength which shows a periodic increase with twice the coherent length buildup and c) with a wavevector mismatch, the output field oscillates periodically with propagation distance.

periodic inversion of the nonlinear coupling coefficient d_{eff}; which in turn compensates for the phase mismatch in the propagation medium. Figure 2.4 shows the dependence of the generated field with respect its propagation length within the medium under three conditions: a) with perfect phasematching $i.e.$ $\Delta k = 0$, b) with quasi phasematching, $i.e.$ $\Delta k = \frac{2\pi}{\Lambda}$, where Λ is the constant of periodicity and c) with a wavevector mismatch, $i.e.$ $\Delta k \neq 0$. In the plot, the L_{coh} is the coherence length of the generated field given by $L_{coh} = \pi/\Delta k$.

To understand quasi phasematching in detail, we consider a grating with a periodic spatial variation along the propagation length z. This results in an alternation of the nonlinear coupling coefficient along the same axis as shown below.

$$d(z) = d_{eff} \sum_{m=-\infty}^{m=\infty} G_m \exp(ik_m z) \tag{2.30}$$

where m is the order of the Fourier series, $k_m = 2\pi m/\Lambda$ is the grating period and G_m is the amplitude of the mth order Fourier coefficients given by $G_m = 2/(\pi m) \cdot \sin(m\pi/2)$. The coupled amplitude equations shown in Equation 2.26 remain the same even for quasi phasematched processes except d_{eff} and Δk is replaced by d_G and Δk_G respectively where $d_G = d_{eff} G_m$ and $\Delta k_G = k_p - k_s - k_i - k_{\Lambda,m}$. Since the nonlinear coefficient decreases with increasing order of the frequency conversion process, it is most desirable to achieve quasi phasematching through a first-order ($m = 1$) interaction. In the fundamental case, the effective nonlinear element is $d_{G,1} = \frac{2}{\pi} d_{eff}$ and the phasematching condition is $\Delta k_{G,1} = k_p - k_s - k_i - \frac{2\pi}{\Lambda}$. In SPDC, Λ will follow the relation shown in [64]

$$\Lambda = \frac{2\pi}{k_p - k_s - k_i} = 2L_{coh} \tag{2.31}$$

Equation 2.31 has huge implications in tailoring the classical and quantum frequency conversion processes. Using Sellmeier equations [65, 66] to calculate the bulk refractive indices of lithium niobate (optical medium used in this work) and the energy conservation in Equation 2.6, we can estimate the poling periods required for type 0 / II (refer Section 2.36) SHG, SFG, DFG and SPDC processes quite accurately.

2.4. Spontaneous parametric down conversion

As mentioned in Section 2.1, spontaneous parametric down conversion is a special case of a DFG process when the amplitude of the input field corresponding to ω_2 is reduced to zero. In this case, the DFG process is suppressed; however the non-zero vacuum fluctuations induces a spontaneous decay of some of the high energy photons (ω_1) to lower energy photons ω_2 and ω_3. This is purely a quantum effect, known as spontaneous parametric down conversion (SPDC). Since vacuum fields are completely random, SPDC will occur for any ω_2 that obeys the energy conservation law. Despite the creation of these lower energy fields, a detectable output can be generated only if these fields constructively interfere within the optical medium; meaning the process needs to be phasematched. The energy and momentum conservation rules are specified in Equation 2.6 - 2.7. The depiction of these fundamental laws are as shown in Figure 2.5.

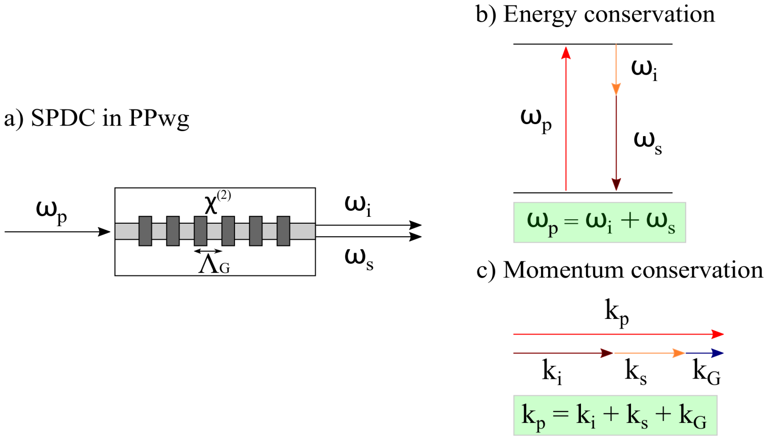

Figure 2.5.: a) Spontaneous parametric down conversion (SPDC) in a periodically poled waveguide (PPwg) and conservation laws in SPDC: b) energy conservation and b) momentum conservation between interacting pump and generated - signal and idler fields. In momentum conservation, we have drawn the phase diagram for a waveguided optical medium with a poling period of Λ_G having a k-vector, k_G.

2.4.1. Theoretical background

SPDC is a three-mode optical process where a high-energy pump photon in one mode (ω_p) decays into two low-energy daughter photons in different modes (ω_s and ω_i) where the conservation laws in Figure 2.5 are obeyed. The quantum mechanical notation, *i.e.* Hamiltonian for SPDC can be derived from the quantisation of classical electric fields interacting within a nonlinear medium and propagating in the z-direction (as is in the case in waveguides). The induced second order polarisation operator becomes

$$\hat{P}^{(2)}(z,t) = 2\epsilon_0 d_{eff} \hat{E}^2(z,t) \tag{2.32}$$

where $\hat{E}(z,t)$ is the quantised electric field given by $\hat{E}(z,t) = \hat{E}^+(z,t) + \hat{E}^-(z,t)$. Each term of the electric field operator describing the interacting fields can be defined using the creation ($\hat{a}^\dagger$) and annihilation ($\hat{a}$) operators.

$$\hat{E}^+(z,t) = E_0 \int \exp[i(k(\omega)z - \omega t)]\ \hat{a}(\omega)\ d\omega \tag{2.33}$$

$$\hat{E}^-(z,t) = E_0' \int \exp[i(k(\omega)z - \omega t)]\ \hat{a}^\dagger(\omega)\ d\omega \tag{2.34}$$

describe the input and output fields respectively. In SPDC, the input (pump) field (E_p^+) is negligibly depleted, hence it can be treated classically as $\hat{E}_p^+ = E_p^+ = \alpha_p(\omega_p)\exp(i(k_p z - \omega_p t))$, where $\alpha_p(\omega_p)$ depicts the envelope of the pump field. The signal ($\hat{E}_s^-$) and idler ($\hat{E}_i^-$) fields are in the single photon levels and hence need to be quantised. The three wave mixing of a SPDC process can be expressed using Equation 2.32 - 2.34 to generate the following Hamiltonian

$$\begin{aligned} \hat{H}_{SPDC}(t) &= \int_z \hat{P}^{(2)}(z,t) E_p^+(z,t) \mathrm{d}z + h.c. \\ &= 2\epsilon_0 d_{eff} \int_z E_p^+(z,t)\ \hat{E}_s^-(z,t)\ \hat{E}_i^-(z,t)\ \mathrm{d}^3 z + h.c. \end{aligned} \tag{2.35}$$

The quantum state produced by this hamiltonian is

$$|\psi(t)\rangle = \exp\left[-\frac{i}{\hbar}\int_0^{t'} \hat{H}_{SPDC}(t')dt'\right]|\psi(0)\rangle \tag{2.36}$$

where $\psi(0)$ is the initial quantum state.

Solving for this Equation over the entire interaction length z, the hamiltonian produces a unitary transformation of the input vacuum state given by

$$\hat{U} = \exp\left[-\frac{i}{\hbar}\left(A\int\int f(\omega_s,\omega_i)\hat{a}_s^\dagger(\omega_s)\hat{a}_i^\dagger(\omega_i)\mathrm{d}\omega_s\mathrm{d}\omega_i\right)\right] \tag{2.37}$$

where A is the product of all the field amplitudes and $f(\omega_s,\omega_i)$ describes the joint spectral amplitude (JSA) of the SPDC process. JSA is a function that describes all the spectral correlations between the signal and idler photons; this makes it a very effective tool to determine various quantum properties of a source (See Section 2.5). The JSA is defined as the product of the input pump distribution ($\alpha_p(\omega_p = \omega_s + \omega_i)$) and the phasematching function ($\phi(\omega_s, \omega_i)$) of the medium.

$$f(\omega_s, \omega_i) = \alpha_p(\omega_p = \omega_s + \omega_i)\phi(\omega_s, \omega_i) \tag{2.38}$$

$\phi(\omega_s, \omega_i)$ in a quasi-phasematched material produces a sinc-shaped output intensity profile given by $\phi(\omega_s, \omega_i) = \operatorname{sinc} \Delta k(\omega_s, \omega_i)L/2$, where L is the interaction length of the waveguide.

2.4.2. SPDC in LN waveguides

The goal of this work is to produce a high efficiency source of single photons using SPDC in LN waveguides. At perfect phasemathching conditions, *i.e.* when $\Delta k = 0$, the output generated from SPDC was shown in [97] by formulating a simple expression:

$$P_s^{wg} = \frac{\hbar d_{eff}^2 P_p \omega_p^3}{6\sqrt{2\pi |GVD(\frac{\omega_p}{2})| \epsilon_0 c^3 n_s n_i n_p}} \frac{L^{3/2}}{A_I} \tag{2.39}$$

where P_s^{wg} is the power of signal generated in the waveguide, P_p is the pump power, GVD is the group velocity dispersion and A_I is the interaction area (in our case, the area of the periodically poled region) of the waveguide. L and A_I can be well controlled in LN using mature source engineering strategies.

As shown in Equation 2.39, the SPDC process is dependent on the inherent properties of the material itself, its nonlinear coefficient d_{eff}. In LN based sources, only two coefficients, d_{33} and d_{31}, have sufficiently high values to trigger a nonlinear process. The largest nonlinear coefficient in LN is d_{33}, which therefore produces the highest conversion efficiency to produce single photons. The SPDC process involved is called type 0 process, where all the interacting fields possess the same polarisation. In the degenerate case, the generated photons are separated either by a 50:50 beam splitter, which results in the loss 50 % of the photons due to splitting conditions, hence lowering the heralding efficiency. A more promising solution is to operate such sources to produce non-degenerate photon pairs so they can be easily separated using wavelength-division-multiplexers, unfortunately limiting their use in quantum interference experiments.

Type 2 processes use the d_{31} coefficient for photon pair generation, which is more than six times smaller than d_{33}. In this case, the signal and idler are orthogonally polarised; hence degenerate photons (which are crucial for interference experiments) can be easily separated based on their polarisation. These photons have long coherence lengths in the picosecond range and hence, exhibit low dispersion on transmission through fibres [98,99]. This process inherently produces narrowband photons as opposed to type 0 processes that generates a broadband spectrum. Furthermore, source engineering and/or spectral filtering can lead to generating pure states [100] which are a crucial resource for efficient quantum interference experiments.

2.5. Characterisation of single photon sources

The performance of photon pair sources are benchmarked using a multitude of characterisation techniques. One of the most important tools required for stable and reliable measurement conditions is a high quality means of photon detection. Below, a brief description on the operation mechanism behind the detectors used in this experiment, namely superconducting nanowire single photon detectors (SNSPDs), is provided. Later, the methods of single photon characterisation is also discussed.

2.5.1. Superconducting nanowire detectors

Superconducting nanowire detectors is one of the most promising technologies invented in the field of quantum optics and high speed optical communications [101]. This technology came to be in the year 2001 when Gol'tsmann *et al* [102] experimentally demonstrated the capabilities of a NbN nanowire at cryogenic superconducting temperatures. Since then, the superconducting properties of various materials were investigated, especially for the detection of telecom photons. Until the arrival of this technology, telecom photons were detected using avalanche photodiodes that showed efficiencies upto 30 %, which caused significant problems for the study of quantum information protocols [103–105].

Principle of operation

Superconducting nanowire detectors are made out of nanowires of Nb(Ti)N [101, 102, 106, 107], MoSi [108], WSi [109] etc. that are maintained well below its superconducting critical temperature and direct current biased close to its critical current. When a photon is absorbed by the nanowire, a local hotspot is created which causes the transition from a superconducting state to a normally conducting region. Due to this, the resistance across the nanowire changes from zero to a measurable value. This is the basis of photon detection in these type of detectors. After a certain period of time (dead time), the nanowire cools down and returns back to its superconducting state.

The efficiency of a superconducting detector depends on three factors [101]:

- the photon has to couple into the active area of the detector, given by η_c
- the photon has to be absorbed by the material, which depends on its absorption coefficient α
- the nanowire must then pass from the superconducting state to a resistive state, given by its internal quantum efficiency η_Q

The efficiency of the detector is thus defined using the product of these three quantities,

$$\eta_{det} = \eta_c \cdot \alpha \cdot \eta_Q$$

.

In the past decade, major advances have been made in the development of high quality superconducting nanowire detectors. Present day commercial detectors show detection efficiencies, $\eta_{det} > 90\%$ [109], dead times $< 10\,\mathrm{ns}$ [110–112], jitter times $< 30\,\mathrm{ps}$ [113] and dark count rates near to zero [109].

2.5.2. Quantum characterisation methods of photon sources

The quality of single photon devices are quantified using a few performance metrics (See 1) to characterise the output generation of sources. These methods are briefly shown below.

Heralding efficiency

Heralding efficiency, also known as Klyshko efficiency [114], is the most important attribute to discern the performance of photon pair sources. As described in Section 2.36, SPDC is a process that generates a photon pair, namely signal and idler, when a pump photon degrades within a $\chi^{(2)}$ nonlinear material. The benefit from this process arises from the ability to determine the presence of one photon (signal) by detecting the other (herald), known as heralding efficiency. The principle can be understood as follows: When 'N_p' pump photons are injected into a nonlinear material, the number of signal (N_s) and idler (N_i) photons created and the rate at which they are generated (N_c) will depend on the conversion efficiency of the medium, η_s and η_i respectively. In a lossless medium, $\eta_s = \eta_i$, resulting in a 100 % heralding efficiency. However, since such an ideal material does not exist, the following equations are used to estimate the heralding efficiency.

$$N_s = \eta_s N_p + D_1, \qquad N_i = \eta_i N_p + D_2 \tag{2.40}$$

$$N_c = \eta_s \eta_i N_p \tag{2.41}$$

where D_1 and D_2 are the dark counts measured by the detector. In our case, since we use SNSPDs which have negligible dark counts, this term is removed in further calculations. η_s and η_i are equated to

$$\eta_s = \frac{N_c}{N_i}, \qquad \eta_i = \frac{N_c}{N_s} \tag{2.42}$$

This shows that the heralding efficiency of the signal is dependent on the coincidence rate between the two photons and the idler count rate; and vice versa for the idler photon. Equation 2.42 is used later to estimate the heralding efficiencies of our source in the experimental section.

Spectral purity

Purity (P) expresses the number of frequency modes (mode number) present in the spectral distribution of a photon pair source. In order to determine the spectral purity, we take the joint spectral amplitude (JSA) function shown in Equation 2.38 and perform a Schmidt decomposition to quantise the correlations present. The JSA can be rewritten [115–118] as

$$f(\omega_s, \omega_i) = C \sum_k c_k \phi_k(\omega_s) \psi_k(\omega_s) \tag{2.43}$$

where C is the normalisation constant given by $C = \sqrt{\int \mathrm{d}\omega_s \mathrm{d}\omega_i f(\omega_s,\omega_i) f^*(\omega_s,\omega_i)}$, k is the mode index, c_k are the normalised eigen values of the JSA with $\sum_k |c_k|^2 = 1$ and ϕ, ψ correspond to the orthonormal eigenvectors related to the JSA. The spectral properties of the signal and idler for mode k is defined by ϕ_k and ψ_k respectively.

The effective mode number (K) or Schmidt number [119] is defined as

$$K = \frac{1}{\sum_k |c_k|^4} \tag{2.44}$$

The purity (P) of the quantum state is given by

$$P = \sum_k |c_k|^4 = \frac{1}{K} \tag{2.45}$$

Indistinguishable sources consist of only one frequency mode and hence show the highest purity of $P = 1$.

Second order correlation function

Correlations function were first introduced by Glauber [120] in 1963 as a means to characterise the coherence properties of quantum states. In this work, we use the second order autocorrelation function $g^{(2)}(\tau)$ to quantify the presence of higher order photonic states. An ideal source will emit only one photon at a given time interval [23]; unfortunately, all light sources have a non-zero probability of producing more than one photon. Classically, the $g^{(2)}(\tau)$ is defined by the optical intensity [120, 121]

$$g^{(2)}(\tau) = \frac{\langle I(t) I(\tau + t)\rangle}{\langle I(t)\rangle^2} \tag{2.46}$$

where τ is the optical delay and $I(t)$ is the intensity at time t. By applying the Cauchy-Schwarz inequality on Equation 2.46, two general conditions are derived:

$$g^{(2)}(0) \geq 1, \qquad g^{(2)}(\tau) \leq g^{(2)}(0) \tag{2.47}$$

to explain the coherence between classical fields. A classical field of constant intensity will have a constant correlation function $g^{(2)}(\tau) = 1$.

For quantum fields these inequalities need not be satisfied, therefore requiring the need to use quantum mechanical operators to express the coherence between particles. Hence, $g^{(2)}(\tau)$ for single-mode light fields is described using the creation $(\hat{a}^\dagger)$ and annihilation $(\hat{a})$ operators.

$$g^{(2)}(\tau) = \frac{\int \langle \mathrm{d}t\ \hat{a}^\dagger(\tau + t)\hat{a}^\dagger(t)\hat{a}(\tau + t)\hat{a}(t)\rangle}{|\int \langle \mathrm{d}t\ \hat{a}^\dagger(t)\hat{a}(t)\rangle|^2} \tag{2.48}$$

In SPDC (refer to Figure 2.6), the output modes are described as

$$\hat{a}_3 = \frac{1}{\sqrt{2}}(\hat{a}_1 - \hat{a}_2) \qquad \hat{a}_4 = \frac{1}{\sqrt{2}}(\hat{a}_1 + \hat{a}_2) \tag{2.49}$$

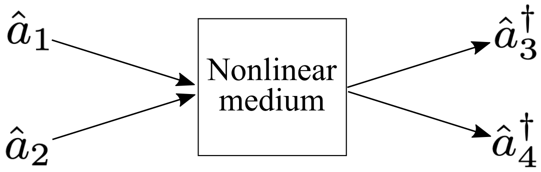

Figure 2.6.: Quantum mechanical operators - creation and annihilation, involved in a photon pair generation process. $\hat{a}_{1/2}$ are input modes and $\hat{a}^\dagger_{3/4}$ are output modes. In SPDC, $\hat{a}_1 = \hat{a}_p$, $\hat{a}_2 = |0\rangle$, $\hat{a}_3^\dagger = \hat{a}_s^\dagger$ and $\hat{a}_4^\dagger = \hat{a}_i^\dagger$, where p, s and i denotes the pump, signal and idler fields.

where the second input $\hat{a}_2 = |0\rangle$ since it corresponds to a vacuum state. The second-order correlation functions for τ and $\tau = 0$ is

$$g^{(2)}(\tau) = \frac{\langle \hat{a}_3^\dagger(t)\hat{a}_4^\dagger(\tau+t)\hat{a}_4^\dagger(t)\hat{a}_3^\dagger(\tau+t)\rangle}{\langle \hat{a}_3^\dagger(t)\hat{a}_3(t)\rangle\,\langle \hat{a}_4^\dagger(\tau+t)\hat{a}_4(\tau+t)\rangle} \tag{2.50}$$

$$g^{(2)}(0) = \frac{\langle \hat{a}_3^\dagger(t)\hat{a}_4^\dagger(t)\hat{a}_4^\dagger(t)\hat{a}_3^\dagger(t)\rangle}{\langle \hat{a}_3^\dagger(t)\hat{a}_3(t)\rangle\,\langle \hat{a}_4^\dagger(t)\hat{a}_4(t)\rangle} \tag{2.51}$$

Since ideal sources emit only one photon per time bin, at $\tau = 0$, the heralded $g^{(2)}(0)$ function becomes $g_h^{(2)}(0) = 0$, which is a characteristic of a pure quantum state [122].

The marginal statistics of each single photon can be described using the second-order autocorrelation function [123, 124] given by

$$g_3^{(2)}(0) = \frac{\langle \hat{a}_3^\dagger(t)^2\hat{a}_3^\dagger(t)^2\rangle}{\langle \hat{a}_3^\dagger(t)\hat{a}_3(t)\rangle^2} \qquad g_4^{(2)}(0) = \frac{\langle \hat{a}_4^\dagger(t)^2\hat{a}_4^\dagger(t)^2\rangle}{\langle \hat{a}_4^\dagger(t)\hat{a}_4(t)\rangle^2} \tag{2.52}$$

Reference [124] shows that $g^{(2)}(0)$ is directly related to the number of frequency modes of the quantum state,

$$\begin{aligned} g^{(2)}(0) &= 1 + \frac{1}{K} \\ &= 1 + P \end{aligned} \tag{2.53}$$

For a decorrelated state, the the marginal statistics of a SPDC photon follows a thermal distribution with $g^{(2)}(0) = 2$ [121]. A strongly correlated state shows Poissonian statistics with $g^{(2)}(0) = 1$. The $g^{(2)}(0)$ measurement is unaffected by losses and therefore plays a crucial role in understanding the quality of photon pair sources.

Hong-Ou-Mandel interference (HOM)

In 1987, Hong, Ou and Mandel put forward a famous interference experiment to measure the duration of photon wavepackets in SPDC photons [125]. This technique is now widely used as a standard method to determine the indistinguishability between photons in quantum systems [115, 126, 127]. HOM interference is also unaffected by losses and hence invaluable for the characterisation of SPDC states. The principle goes as follows: Consider a SPDC state given by Equation 2.37

$$|\psi\rangle = \int \mathrm{d}\omega_s \mathrm{d}\omega_i f(\omega_s, \omega_i)\, |\omega_s, \omega_i\rangle \tag{2.54}$$

is passed through a beam splitter with reflection R and transmission T, where $R+T=1$ and ideally $R=T=\frac{1}{2}$ as depicted in Figure 2.7. The coincidences between the two

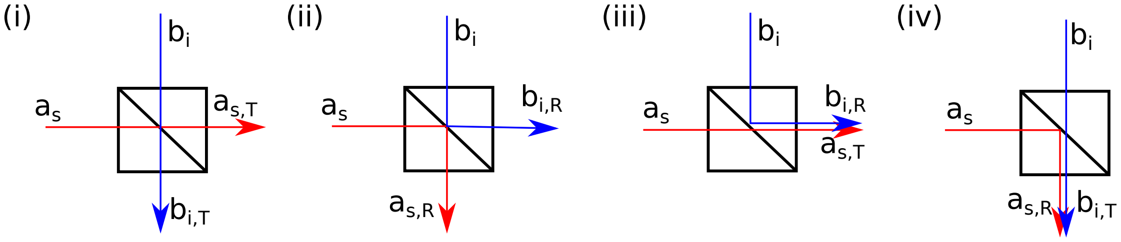

Figure 2.7.: Four possible outcomes for when two photons are incident on a 50:50 beam splitter - (i) both photons are transmitted, (ii) both photons are reflected, (iii) and (iv) one photon is transmitted and the other reflected. 's' and 'i' represents the signal and idler photons, 'T' and 'R' signifies if the photon is transmitted or reflected.

output ports will be

$$N_{cc} = C(T^2+R^2)\left[1 - \frac{2RT}{R^2+T^2}\exp(-(\Delta\omega\delta\tau)^2)\right] \tag{2.55}$$

where $\Delta\omega$ is the difference in the photonic bandwidths, $\delta\tau$ is a small time delay in the photon propagation times and C is a constant. When the light is monochromatic, no coincidences are seen, hence $N_{cc}=0$, thereby showing the highest "visibility (V)" between photon states. Visibility is a quantity that depicts the indistinguishability between the interfering photons as shown in the equation below,

$$V = \frac{N_{cc}^{max} - N_{cc}^{min}}{N_{cc}^{max} + N_{cc}^{min}} \tag{2.56}$$

where N_{cc}^{min} and N_{cc}^{max} is obtained when $\delta\tau = 0$ and $\delta\tau > \tau_{photon}/2$ respectively and τ_{photon} is the pulse duration of the photon wavepacket. Since SPDC light is not monochromatic, $V < 1$; but can be very close to unity through source engineering and effective spectral filtering [100].

Chapter 3

Device development

Indiffused waveguides in lithium niobate (LN) are fabricated by incorporating materials with a higher refractive index like titanium (Ti) [69,72,91,128,129] or zinc (Zn) [130–132] into the substrate. One of the most versatile methods is the indiffusion of Ti into LN substrates (Ti:LN) to form a low guiding structure with a refractive index contrast of $\Delta n \approx 10^{-3}$ [68,94,133]. In the application of quantum optics, these waveguides prove to be an invaluable asset due to their inherently low losses [72,91,129,134] in the telecom regime and well-defined single mode operation [135–137]. The fabrication techniques involved are very mature and hence a high level of integration is feasible [56,138,139]. Ti:LN waveguides guide both - horizontal (TE) and vertical (TM) polarisations [72,140], thereby making them good candidates to exploit various frequency conversion processes including type 0 [141–143] and type II SPDC processes [144–146], sum frequency generation [147–149], difference frequency generation [150–153] etc. Lastly, the guided optical modes within these waveguides can be coupled into commercially available fibres with high efficiencies [136,137,154] thereby making them a suitable candidate for long distance quantum communication protocols [99].

3.1. Plug-and-play device - the design

The schematic in Figure 3.1 reveals the complete design of our single photon source. We demonstrate a "plug & play" source of heralded single photons in the telecom regime which is fully packaged in an aluminium housing that is capable of producing desirable quantum properties in terms of heralding efficiency, brightness and indistinguishability. Here, a low loss titanium indiffused periodically poled lithium niobate (Ti:PPLN) waveguide acts as our type II SPDC-based degenerate source of single photons. Each face is coated with the required anti- and high- reflective coatings for high transmission and suppression of the SPDC and pump photons respectively. Since the output photons are polarised, the input and output faces of the waveguide are pigtailed with polarisation maintaining (PM) fibres. The orthogonality provides an easy separation of the degenerate photons by using a fibre polarisation beam splitter (fibre-PBS). Each end of the fibre-PBS is spliced to a pair of C-band in-line isolators to provide a 40- to 60- dB additional pump suppression at the pump wavelengths. A C-24 dense-wavelength-division-multiplexing (DWDM) filter with a bandwidth of 1.6 nm (200 GHz) is also attached to the signal (heralding) arm to increase spectral purity and remove noise. The idler arm remains unfiltered to ensure maximum transmission.

The steps required to develop our device is as follows:

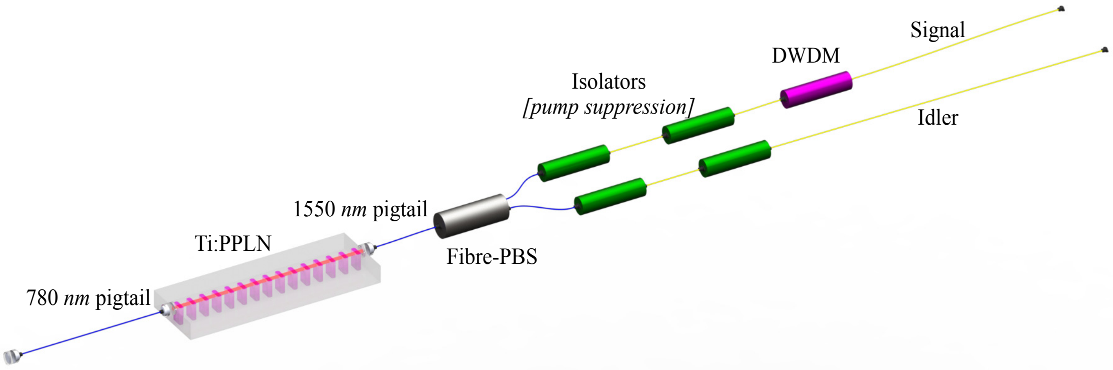

Figure 3.1.: Schematic of our type II heralded single photon source. A Ti:PPLN waveguide is pigtailed at the input and output end facets using polarisation maintaining fibres. The generated SPDC photons are split on the basis of their polarisation using a fibre polarisation beam splitter (fibre-PBS). A pair of isolators in each arm removes the pump and a dense wavelength division multiplexer (DWDM) in the heralding (signal) arm provides noise suppression and desirable spectral filtering.

1. Fabrication of titanium indiffused waveguides in lithium niobate
2. Periodic poling through domain inversion
3. End face coatings
4. Fibre pigtailing and packaging.

3.2. Fabrication of titanium indiffused waveguides in lithium niobate

Prior to fabrication, we deduce the fabrication parameters required to produce waveguides with desired properties. Using a commercial software (FEMSIM package, RSoft), we model Ti:LN waveguide designs with the following constraints - single mode operation at wavelengths near 1550 nm, low scattering losses for TE and TM polarisations and high butt-coupling efficiency with fibres. By taking into consideration the outcomes of the model and previous knowledge within the group, we determined the width and height of the titanium strip and indiffusion parameters like temperature, time etc.

The process of Ti:LN waveguide fabrication is shown in Figure 3.2. LN chips are exposed to high purity titanium e-beam evaporation to deposit a 80 ± 2 nm thick Ti layer on the $+c$ surface. A thin layer of photoresist (PR) is spin-coated to pattern waveguide structures onto the sample. A soft bake is then performed for 30 min at 105 °C to evaporate the solvents in the PR.

The next step is to pattern the Ti channels with width of 7 µm on the substrate using ultra-violet (UV) photolithography. For this process, a photo-mask with channel structures is aligned with respect to the sample and then placed in vacuum-contact during UV illumination for 80 s. The chip is developed to remove the UV-exposed PR regions. The uncovered Ti regions are etched away and the residual PR is then washed off, leaving behind only the desired channel waveguide structure on the surface. The sample is enclosed within a platinum box and inserted into an indiffusion oven for 8.5 h

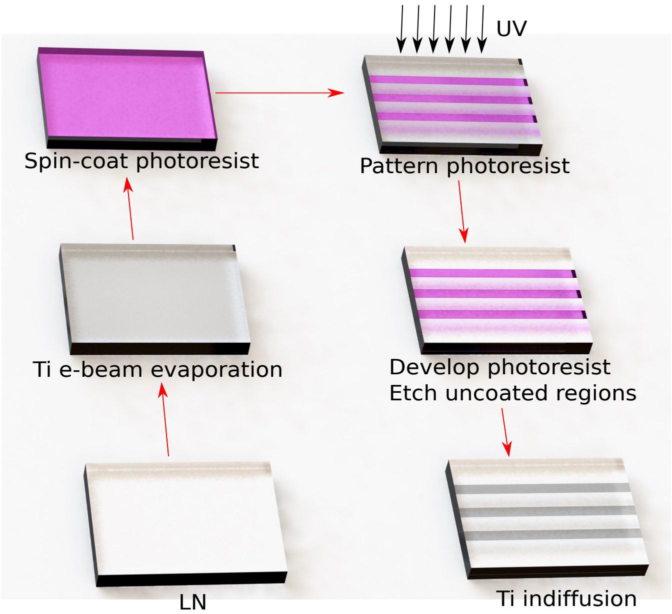

Figure 3.2.: Fabrication steps for Ti:LN waveguides.

at 1060 °C in an oxygen rich atmosphere. Once the sample reaches room temperature, the $-c$ face is ground carefully to remove a few tens of microns of the substrate material. This is done to remove the Li_2O build up that mainly occurs on the $-c$ face of LN during indiffusion [155] which acts as an insulating layer for electric field poling.

3.3. Periodic poling through domain inversion

As described in Section 2.3, periodic inversion of domains in LN is a much-required step to improve the nonlinearity of the material. A well known method is by applying pulses of high voltages across the substrate to induce a periodic pattern to reduce the phase-mismatch between the interacting fields. The poling period depends on the non-linear material in use, the type of the non-linear process and the desired frequency conversion. Here, we fabricate a degenerate type II SPDC source that is capable of generating telecom photons near 1550 nm. Using energy and momentum conservation Equations shown in Equation 2.6 - 2.7, the grating period required for this process is numerically calculated to be approximately $\Lambda = 9\,\mu\text{m}$. For this work, we use a grating mask that contains poling periods $\Lambda = 9.04\,\mu\text{m}$, $9.08\,\mu\text{m}$ and $9.12\,\mu\text{m}$.

The steps required for poling is as shown in Figure 3.3 (a). The Ti:LN sample is coated with a photoresist material to pattern electrodes for poling. The photoresist is structured using UV photolithography as mentioned in Section 3.2. Despite the requirement of a periodic pattern on the sample, the ratio of the uncovered to covered PR regions are always less than a 1:1 duty-cycle. This consideration is made due to the large difference in the domain growth along the lateral and vertical directions in LN.

Electrodes are deposited on the sample by sputter coating Au-Pd in a high vacuum chamber. The electrodes are only deposited on regions where no PR is present. The

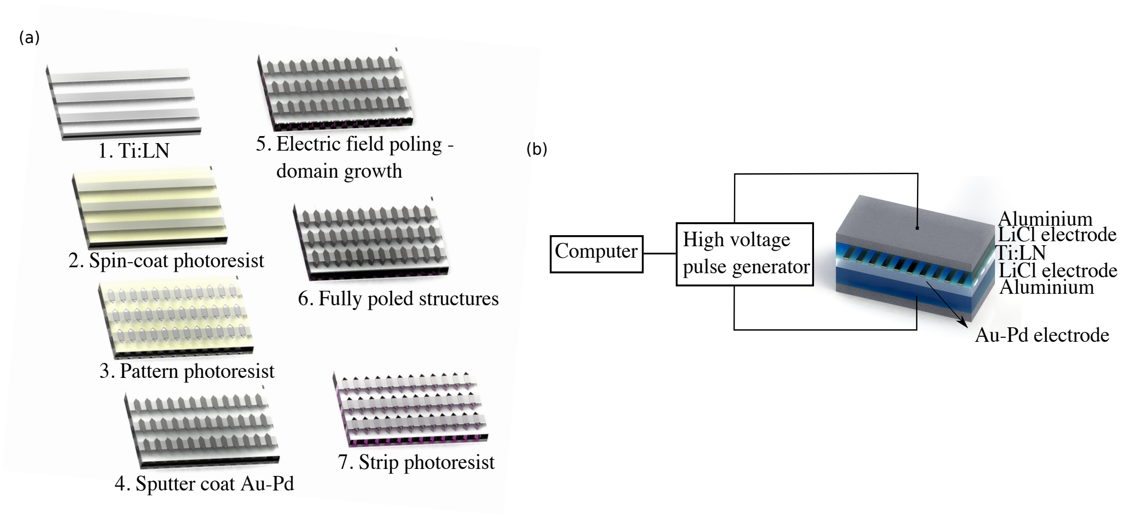

Figure 3.3.: (a) Steps used for periodic poling in Ti:LN using electric field domain inversion, (b) setup used for periodic poling.

chip is now ready to be poled using the setup shown in Figure 3.3 (b). A stream of high voltage pulses of duration $\tau_{pulse} = 2\,\mathrm{ms}$ and voltage greater than the coercive field of LN is applied. The poling process is monitored by measuring the current flow through the circuit. The termination point for the poling process is determined in advance by taking into account the thickness of the LN sample, the effective poling area and charge associated with spontaneous polarisation in LN.

After poling, the metal and PR layer is etched away. Then, the sample is cut to the desired length and polished on both end facets to minimise scattering losses. The final length of the sample is fixed to 25 mm with an effective poling length of 21 mm.

3.4. Classical characterisation

Classical measurements are conducted to obtain a preliminary understanding of the source performance. The linear and nonlinear methods used and the measurement results obtained are explained in this Section.

3.4.1. Loss measurement

Losses pose a serious challenge in quantum photonic applications. Unlike classical systems where losses can be compensated by amplification, quantum states cannot be deterministically replicated due to the no-cloning theorem [103]. Hence, minimising losses of each component in single photon sources is key to developing devices for important applications like quantum information processing [105] and tests of Bell's inequality [156] which are fundamentally intolerant to loss. The most important attribute of a heralded single photon source is its heralding efficiency, which is defined by the ability of a source to predict the presence of one photon by detecting the other (herald). To determine the heralding efficiency, we measure the losses introduced by each component involved from photon generation to detection and estimate the total transmission of the optical channel. In ‘plug & play’ geometries, losses arise in the waveguide, waveguide-fibre interface and the fibre optical components used for photon routing and filtering.

To estimate the propagation losses in our waveguide, we use a temperature-tuned Fabry-Perot [129] loss measurement schematic as shown in Figure 3.4. This measurement is reliable only for single-mode operation and therefore, we can estimate the losses of the waveguide only at the SPDC wavelength, $\lambda_{SPDC} \approx 1550\,\mathrm{nm}$ (the waveguide supports higher-order pump modes). The losses are measured prior to the application of end face coatings and pigtailing, since this method depends on the Fresnel reflections at the input and output faces of the waveguide.

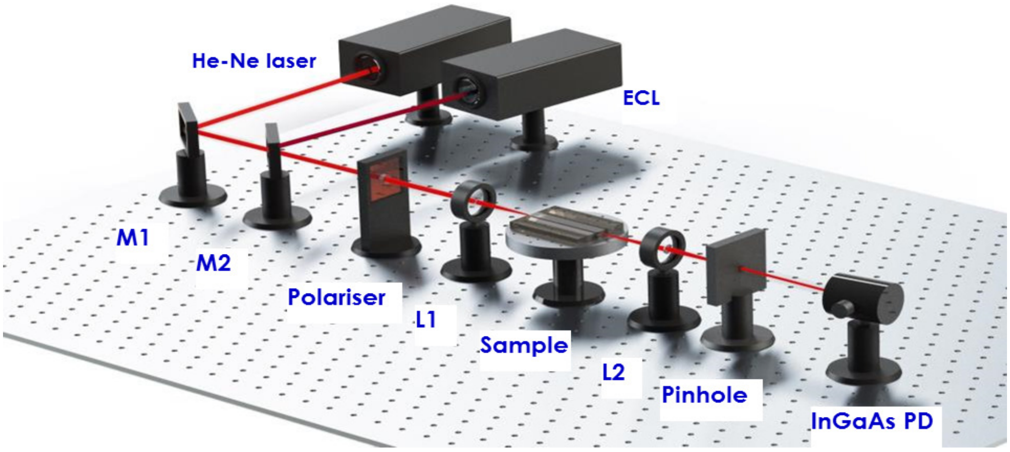

Figure 3.4.: Schematic of Fabry-Perot loss measurement setup. Light from a ECL is injected into the waveguide in the TE and TM polarisations and measured using an InGaAs PD while temperature tuning the sample. The He-Ne laser light is used only for rough alignment of the waveguide. Abbreviations: He-Ne laser, Helium Neon laser; ECL, external cavity laser; M1, M2, mirrors; L1, L2, aspheric lenses; InGaAs PD, Indium Gallium Arsenide photodiode.

Light from a narrowband external cavity laser (ECL) at $\lambda \approx 1550\,\mathrm{nm}$ is coupled in and out of the waveguide using C-coated aspheric lenses. A polariser is used to control the polarisation of the beam before entering into the waveguide. The sample is mounted on a holder consisting of Peltier elements to tune the temperature of the sample. A InGaAs p-i-n photodiode is used to measure the output light. The measured output intensity variations with respect to time is plotted in Figure 3.5. The waveguide losses are estimated from the expression,

$$\alpha = \frac{10}{L_{wg}} \cdot \log \left[R \cdot \frac{1 + \sqrt{I_{min}/I_{max}}}{1 - \sqrt{I_{min}/I_{max}}} \right] \tag{3.1}$$

where α gives the waveguide losses in decibels per centimeter, L_{wg} is the length of the waveguide in centimeters, I_{min} and I_{max} is the minimum and maximum detected photo-intensities on temperature tuning (See Figure3.5) and R is the Fresnel reflection given by $R = (\frac{n_{eff}-1}{n_{eff}+1})^2$. The n_{eff} is estimated from the polarisation and wavelength of the in-coupled light. The waveguide chosen for pigtailing showed losses of $\alpha_{TE} = 0.13 \pm 0.02$

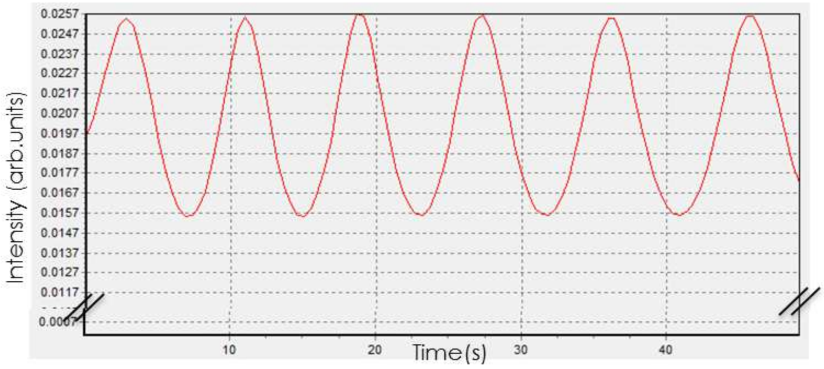

Figure 3.5.: Measured output intensity while temperature the sample to determine the losses of the waveguide using the Equation 3.1.

dB/cm and $\alpha_{TM} = 0.18{\pm}0.02$ dB/cm for TE (horizontal) and TM (vertical) polarisations respectively.

Next, we tested each fibre-optical component to determine their insertion losses. The fibre-PBS that is used to split the SPDC photons according to their polarisation is spliced to a pair of in-line C-band isolators to minimise losses through the channel. A narrowband ECL connected to a polarisation controller is injected into the input port of the fibre-PBS and the output power at each arm was measured when maximum extinction was seen in the other arm. The measured transmissions of the PBS-isolators combination are $(84.0 \pm 1.9)\%$ and $(81.5 \pm 1.9)\%$ respectively for the TE and TM polarisations respectively. The transmission of the DWDM filter attached to the signal (TE-polarised) arm is measured to be $(86.0 \pm 2.0)\%$. Since we use the signal arm for heralding, the total transmission of this arm does not affect the heralding efficiency of the source. Therefore, the maximum heralding efficiency achievable in the idler (TM polarised) arm is calculated to be $\eta_i^{calc} = \mathrm{T_{wg,TM}} \cdot \mathrm{T_{FP,TM}} \cdot \mathrm{T_{PBS,TM}} = (58.6 \pm 3.3)\,\%$ before detection, where $\mathrm{T_{wg,TM}}$, $\mathrm{T_{FP,TM}}$ and $\mathrm{T_{PBS,TM}}$ is the transmission of the waveguide, fibre pigtail and the PBS-isolator unit respectively for TM polarisation. This classical estimation is the maximum heralding efficiency that this device can experimentally demonstrate. In principle the quantum loss should be equal to the classical loss; but background noise from the pump, fluorescence, or parasitic nonlinear processes can show an increase in the heralding counts without its partner photon, resulting in a lowering of the heralding efficiency [57, 58, 157, 158]. We will prove in the following sections that these effects are negligible in our device, resulting in a heralding efficiency close to the classical value.

3.4.2. Mode size measurement

One of the most important steps towards designing a 'plug & play' SPDC source is obtain a high efficiency coupling between fibres and waveguides. An intuitive understanding of this parameter can be obtained by investigating the near field intensity profiles of the guided optical modes in the TE and TM polarisations and fibre-optic modes, at telecom (SPDC) wavelengths. We can estimate the waveguide to fibre coupling efficiency by calculating the overlap integral between the field distributions of the two corresponding systems using

$$\eta_{FC} = \frac{|\int\int E_{wg}(x,y)\cdot E_{fibre}(x,y)dxdy|^2}{\int\int E_{wg}^2(x,y)dxdy\cdot\int\int E_{fibre}^2(x,y)dxdy} \tag{3.2}$$

where, $E_{wg}(x,y)$ and $E_{fibre}(x,y)$ shows the field distributions along the width and height of the waveguide and fibre-optic spatial mode respectively.

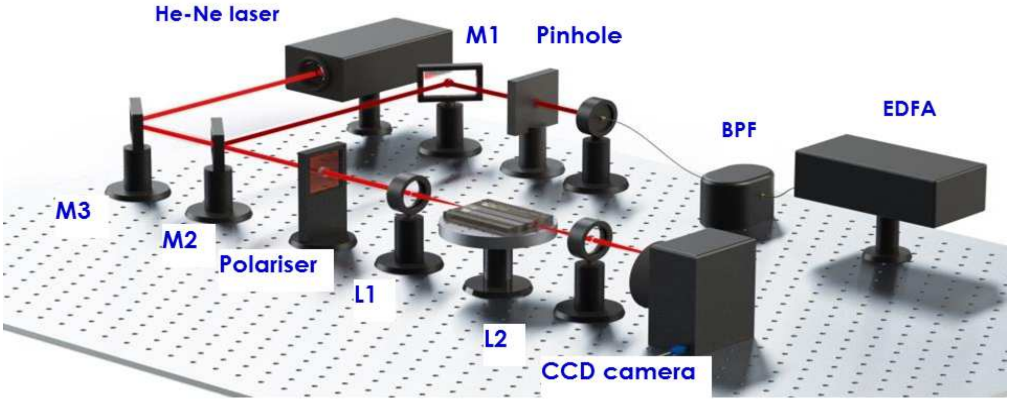

Figure 3.6.: Schematic of mode size measurement setup. Light from a EDFA is injected into the waveguide in the TE and TM polarisations after filtering down to 1 nm by a bandpass filter (BPF) and measured using a charge-coupled device (CCD). The He-Ne laser light is used only for rough alignment of the waveguide. Abbreviations: He-Ne laser, Helium Neon laser; EDFA, erbium doped light amplifier; M1, M2, mirrors; L1, L2, aspheric lenses.

The setup used to measure the near field intensities of waveguides and commercial polarisation maintaining fibres (PMFs) are as shown in Figure 3.6. A broadband white light source (EDFA) at 1550 nm with a bandwidth of $\Delta\lambda \approx 30$ nm is used to couple light into the waveguide in order to remove undesirable interference effects. Being extremely broad, the source can result in the production of blurry mode images due to dispersion, which is eliminated by adding a 1 nm bandpass filter to the setup. A 20× objective is used to inject light into the TE and TM polarisation modes of a waveguide (or optical fibre). A 100× objective is used to collect light and image it onto a Xenics InGaAs array with a resolution of 20 µm/pixel.

The intensity profiles of the TE (left) and TM (centre) polarised modes of the waveguide is shown in Figure 3.7 and the mode profile of the PMF is shown in Figure 3.7 (right). The full width at half maximum (FWHM) of the TE (ordinary) mode of a 7 µm waveguide are measured to be 7.0 µm for the width and 4.7 µm for the height, and for the TM (extra-ordinary) mode 5.3 µm and 3.4 µm respectively. Both TE and TM modes show a gaussian field distribution along the width and a hermite-gaussian distribution along its depth. The asymmetry in the mode shapes is consistent with typical titanium-indiffused waveguides [68,133,159] due to a concentration gradient of Ti during indiffusion.

The measured mode diameter of a PMF is almost perfectly symmetrical with a width of 6.08 µm. With this measured data the mode profiles are modelled (FemSIM package, RSoft) to find the maximum achievable coupling efficiencies between waveguide and fibre

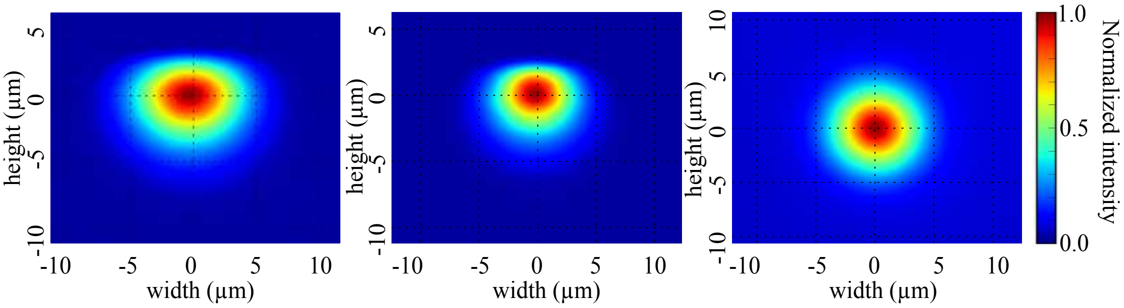

Figure 3.7.: Measured waveguide mode profiles in the TE (left) and TM (centre) polarisations and a polarisation maintaining PANDA 1550 nm fibre mode (right) profile.

modes (using 3.2) for TE and TM polarisations. It was estimated to be 92 % for the TE and 85 % for the TM mode. The main reason for losses in the coupling is due to the mismatch in the field distributions between fibres and waveguides. On pigtailing we see a further reduction in the out-coupling efficiencies as shown in Section 3.6 which arises from different guiding profiles of TE and TM modes in the waveguide [72]. In this work, we optimise the coupling to achieve similar transmissions for both polarisations through the PMF simultaneously.

3.4.3. Second harmonic generation (SHG)

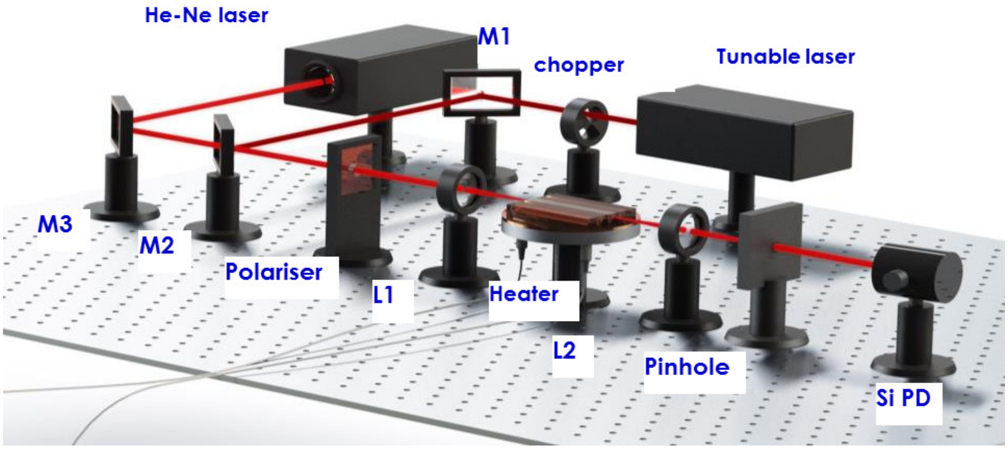

Figure 3.8.: Schematic of SHG measurement setup. Light from a tuneable laser (ECL) at $\lambda_{fund} \approx 1550\,\text{nm}$ is injected into the waveguide at a 45° polarisation to induce a type-II SHG process. A chopper is used to lock in to the frequency of the fundamental wavelength to detect small power outputs in the SHG wavelength regime. The generated frequency-doubled light is measured using a Si-PD (silicon photodiode). The He-Ne laser light is used only for rough alignment of the waveguide. Abbreviations: He-Ne laser, Helium Neon laser; M1, M2, M3 mirrors; L1, L2, aspheric lenses.

Testing of quantum information protocols requires high efficiency sources that are capable of producing large number of single photons; in other words, the source needs

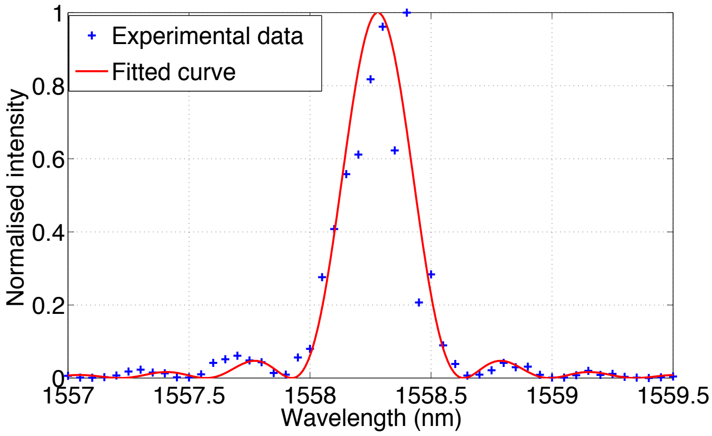

Figure 3.9.: Measured (blue markers) and fitted (red solid line) second harmonic intensity with respect to the injected fundamental wavelength.

to show high brightness. This property is indirectly related to the SHG efficiency, which is a classical substitute to determine the SPDC brightness, that is also affected by the nonlinearity of a periodically poled waveguide. SHG measurement is a powerful technique to give us some information on the quantum light, for e.g. the phase-matching bandwidth, the degeneracy point and the nonlinear conversion efficiency.

The setup used for SHG measurement is as shown in Figure 3.8. A tuneable continuous-wave external cavity laser at telecom wavelengths, TUNICS is used as the fundamental input. A chopper is used to modulate the fundamental power to help the detection of the smallest intensities of SH power using a lock-in amplifier. The polarisation of the input light is maintained at 45° to excite a type II SHG process in the waveguide. Since the central wavelength of the phasematching peak is highly dependent on the temperature, we stabilise the sample at 25 °C. C- and B-coated aspheric lenses are used to couple the fundamental power in and the SH power out of the waveguide respectively. The SH power is then measured using a Si p-i-n diode and the fundamental power is measured using a powermeter.

The detected SH power is traced out with respect to the input fundamental power as shown if Figure 3.9. The phasematching peak, which corresponds to the degeneracy wavelength of the SHG process, is observed at 1558.29 nm with a bandwidth of $0.30 \pm 0.02 nm$. The SHG efficiency was estimated using

$$\eta_{SHG} = \frac{P_{SHG}}{P_{f,in}^2 \cdot L^2} \cdot 100 \tag{3.3}$$

where P_{SHG} is the output SHG power, $P_{f,in}$ is the input power of the fundamental field and L is the length of the poled region. The highest SHG efficiency was measured to be $(2.36 \pm 0.21)\,\%\,\mathrm{W}^{-1}\,\mathrm{cm}^{-2}$. Since type II shows lower nonlinear efficiencies type 0 SHG processes due to a lower nonlinear coefficient, d_{31} (as opposed to d_{33} for type 0), the measured efficiency matches well with already published results [1], thereby showing

---

[1] d_{31} coefficient is nearly seven times smaller than the d_{33} coefficient. The highest type 0 SHG efficiencies reported so far in LN is $150\,\%\,\mathrm{W}^{-1}\,\mathrm{cm}^{-2} shownbyParameswaranetal$ [160].

that the device is capable of producing large number of photon pairs, also known as brightness, when operated in the quantum domain. We used the central SHG wavelength $\lambda_{SHG} = degeneracywavelength/2$ shown in Figure 3.9 for the production of degenerate heralded single photons.

3.5. End face coatings

When light is coupled in and out of materials, a certain percent is lost due to Fresnel reflections; in LN, there is a loss of nearly 14 % when transmitting telecom wavelengths. Since the feasibility of quantum protocols are highly susceptible to losses [105, 156], we aim at reducing these interface losses by applying dielectric coatings on the sample end faces. This is implemented by depositing alternating layers of a high- and low-index materials, namely titanium dioxide and silicon dioxide respectively. In this work, our output medium are fibres and hence we design coating layers to facilitate optimal transmission from LN to glass. Using a commercially available software (OptiLayer), we determine the geometrical requirements of the coatings (number of layers, thickness of each layer etc.) to minimise coupling losses from LN to fibres in the operating wavelength regime.

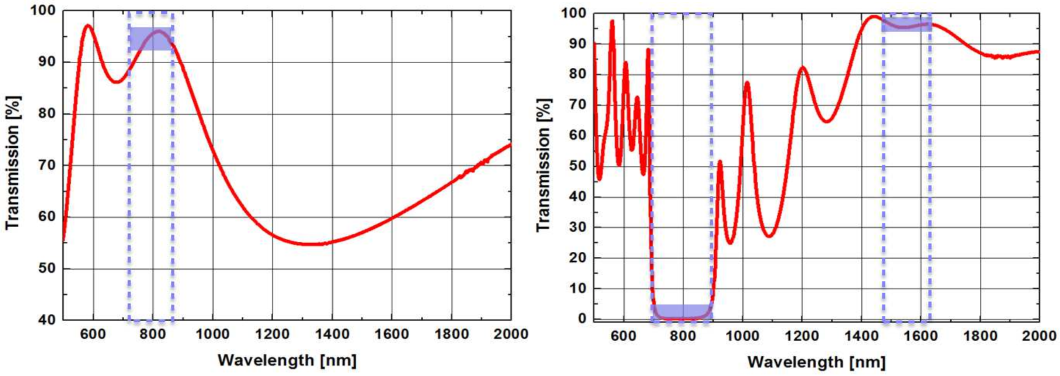

Figure 3.10.: Spectral characteristics of the (left) antireflective coating for $\lambda_{pump} \approx 775\,\mathrm{nm}$ (shaded region) applied to the input facet and (right) a complex stack of high- and anti- reflective coatings at the output facet for $\lambda_{pump} \approx 775\,\mathrm{nm}$ and $\lambda_{SPDC} \approx 1550\,\mathrm{nm}$ (marked regions) respectively.

As shown in Figure 3.1, the input port of our source is injected with wavelengths near 775 nm corresponding to our pump. Hence, we implement a simple three-layer dielectric stack to act as an anti-reflective coating within this spectral range (See Figure 3.10 (left)). At the output port however, we must take into account two major requirements: i) maximum transmission of the generated telecom SPDC photons and ii) maximum suppression of the pump field. Due to this, a more complex coating stack of 17 layers of the same alternating materials is required. The transmission spectra of the resultant coatings are shown in Figure 3.10 (right). The measured transmission of 775 nm at the input port is roughly 94 %; the output port showed a transmission of 95 % at 1550 nm and a pump suppression of approximately 22-dB. Since the coating design is optimised for coupling to fibres and the transmission characteristics are measured with respect to air, the measured output characteristics shows a slight under-estimation of the actual design.

3.6. Fibre pigtailing and packaging

Propagation of quantum light for a variety of applications requires coupling of these states into fibre transmission lines [99]. Thus low-loss interfaces between quantum devices, here Ti:PPLN single photon source, and optical fibre networks [161–165] are of considerable importance. A rather beneficial device design will consist of a ”black box” single photon source which only needs to be connected to a laser input. To implement this, it is vital to permanently attach fibres to the Ti:PPLN waveguide chip. Integration and packaging of optical elements often degrades the efficiency of quantum devices [57, 58, 166]; therefore, most photon sources rely on the careful alignment of external bulk components for high performance, limiting their usefulness outside the lab. Optimisation of fibre-pigtailing strategies could provide considerable advantages when building sensitive quantum devices in this regard.

To produce a fully fibre-integrated source, the front and rear ends of the waveguide chip is linked to fibres. In our case, we use polarisation maintaining fibres (PMFs) since type II SPDC produces orthogonally polarised photons. Pigtails at suitable wavelengths are prepared by fixing a glass ferrule on one end of the fibre and a fibre connector on other. For stability and precise control of the pigtail, the attached ferrule is ground out to produce a ’flat’ surface parallel to the stress rods in the fibre. To position the fibre with respect to the waveguide, the ’flat’ end of the ferrule is then set on a six-axis motorised stage attached with a vacuum tip.

The pigtailing protocol is carried out by injecting light into the sample and measuring the collected light transmitted through the waveguide and then into the fibre. The source is glued onto a copper platform that holds a thermoelectric cooler (TEC) for temperature stabilisation. The TEC can operate at temperatures up to 70 °C; but all measurements are conducted at 25 °C since the source is designed to produce degenerate telecom SPDC photons at room temperature. We begin by pigtailing the end face which out-couples 1550 nm (SPDC wavelength). We use a broadband pump (Erbium doped fibre amplifier (EDFA)) attached to a 1.6 nm filter as a light source for telecom wavelength coupling in order to limit interference effects. A polariser at 45° is used in the setup to imitate the output of the SPDC process, *i.e.* generation of orthogonally polarised photons. Firstly, the light is coupled in and out of the waveguide using aspheric lenses that shows high transmission in the telecom band, *i.e.* C-coated lenses, and measured using indium gallium arsenide photodiodes (InGaAs-PD). This is performed to get an intuition on the maximum power that can be obtained after the waveguide.

The output lens is then moved away and the fibre pigtail is used as the light collection medium. The output of the pigtail is connected to a fibre polarisation beam splitter (fibre-PBS) and the power at each port is measured using fibre connected InGaAs-PDs (See Figure 3.11). The pigtail is coarsely aligned to get a preliminary position that yields a maximum coupling efficiency. The fine alignment is performed by a programmable six-axis stage that holds the fibre pigtail. This stage allows manipulation of the fibre position in sub-micron resolutions, thereby making the setup extremely sensitive to fibre

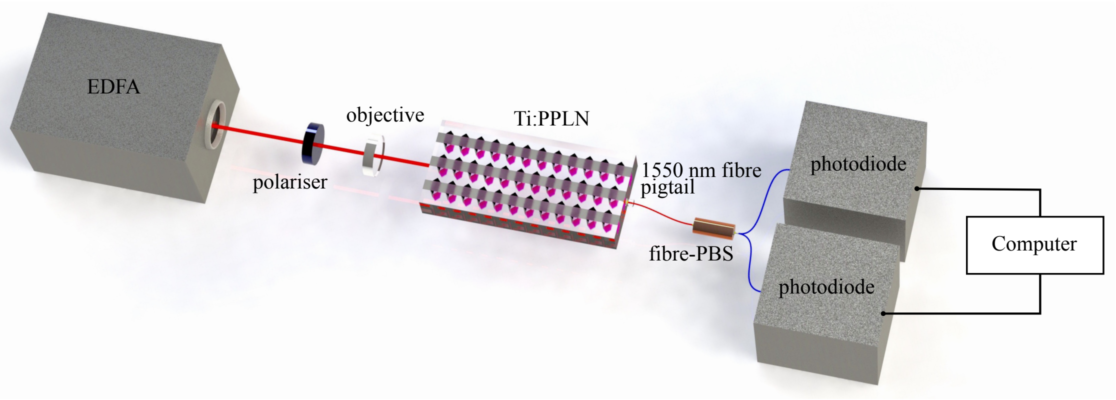

Figure 3.11.: Setup for pigtailing the 1550 nm polarisation maintaining fibre pigtail to waveguide.

positions. The fibre is scanned along the width and height of the waveguide end facet. After performing multiple scan iterations of increasing resolution, the optimal position is determined when the output power is highest for both polarisations.

For permanent fixture of the fibre, a UV curing glue (Norland Products Inc., NOA81) is applied at the interface between the fibre and waveguide. Due to the presence of the glue, the position of the fibre may shift slightly; hence, a minor re-alignment is performed to maximise transmission. The coupling efficiency measured at this stage is 88% for the TE mode and 80 % for the TM mode. A pre-curing step of 5 min is performed by a ring-shaped arrangement of LED diodes to provide uniform curing along the outer edges of the glue. The vacuum tip is switched off to release the fibre and then a final curing step is done by irradiating from top and botton of the fibre-waveguide interface by a high intensity UV gun for 30 s each. During the curing process, the position of the fibre may displace resulting in a slight reduction in the transmitted power. An invar holder is screwed into the sample holder to provide mechanical stability to the fibre-waveguide interface. To prevent the pigtail from detaching due to tension, a small droplet of quick-fastening two component epoxy adhesive (ECCOBOND 286) is applied to hold the fibre to the invar block. The UV curing glue and epoxy adhesive is left to stabilise overnight.

The pigtailing efficiency with respect to the lens coupling is estimated by the ratio between the two and the calibration parameters of the setup. The calibration parameters include the transmission values of the lenses used, the freespace polariser, the fibre-PBS, fibre connectors and the efficiencies of the InGaAs-PDs. The final fibre coupling efficiency at telecom wavelength is measured to be $\eta_{TE} = 83.8 \pm 1.8$ % and $\eta_{TM} = 75.7 \pm 1.6$ % for TE and TM polarisations respectively.

The next step is to pigtail the pump side (780 nm) of the source. To obtain a source with a high SPDC efficiency, it is crucial that the pump is maximally coupled into the fundamental waveguide mode. However, since the waveguide supports multiple pump modes, a simple injection of the pump wavelength into the waveguide and measuring the output power is not sufficient for an optimal pigtailing process. Hence, we exploit a type II second harmonic generation (SHG) in the waveguide to produce an inverse SPDC geometry, *i.e.* conversion of telecom light to 780 nm wavelength. The source of telecom

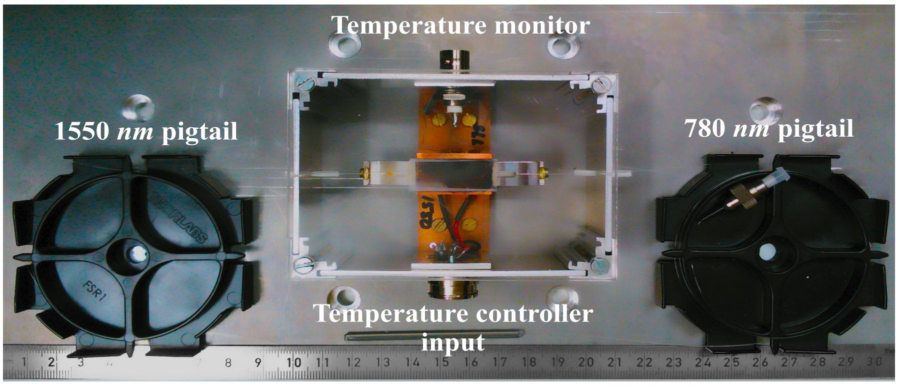

Figure 3.12.: Image of the fully packaged plug-and-play single photon source of telecom photons.

photons is a narrowband tunable TUNICS laser, that is injected into the telecom fibre pigtail. The output power is amplified using a lock-in amplifier and measured using a silicon photodiode (Si-PD). The optimisation protocol for fibre pigtailing at the pump end is performed in the same way as above. In this case, the pigtailing efficiency is measured to be $\eta_{pump} > 30\%$.

After pigtailing both end faces, the source is packaged in a home-made aluminium housing. The leads coming out of the TEC element is soldered to a D-sub connector. To verify the applied temperature, a thermistor attached to a female-BNC connector is also included in the package. The housing is mounted onto a larger aluminium plate that has fibre-optic reels to safely loop the input and output pigtails. In the final configuration of the source, the output arm is spliced to a fibre-PBS, a pair of isolators and a DWDM filter (only the signal arm). The fully fibre-integrated and packaged source is as shown in Figure 3.12.

Chapter 4

Quantum characterisation

Quantum light sources should possess desirable properties for quantum applications in terms of heralding efficiency, brightness and spectral correlations. The technological parameters take into consideration these requirements, yet a thorough investigation of the optical properties is elementary to determine the source specifications. Classical light is easier to generate and detect than quantum light, hence it is preferred to use classical characterisation tools to predict quantum behaviour. However, in order to get a thorough understanding of spectral bandwidth and correlations within the source, a full quantum characterisation is of vital importance. We determine the scattering losses of the waveguide and the fibre optical components used to build the source to estimate the maximum heralding efficiency that can be achieved by the source. Mode size measurements help determine the maximum waveguide to fibre coupling for both polarisations. We also look at the second harmonic generation (SHG) process, which is a reverse process of SPDC, to determine the nonlinear conversion rates of the periodically poled waveguide. The waveguide that shows the best performance on all these attributes is chosen for pigtailing and further quantum characterisations.

The quality of a single photon source can be benchmarked using features such as heralding efficiency, brightness, spectral and modal properties of the quantum light generated. Noise from fluorescence, parasitic nonlinear processes, pump photons and dark counts from detectors strongly degrade the quantum performance and hence it is of vital importance to design the source appropriately to minimise these effects.

Setup: The setup used for quantum measurements is as shown in Figure 4.1. A 76 MHz laser pulse-picked to 1 MHz is used to produce picosecond pump pulses with a FWHM bandwidth of 0.3 nm at 779.15 nm wavelength. The pump wavelength is obtained from half the degeneracy point of the fundamental wavelength measured with SHG. The input pump power is controlled by a half-wave plate (HWP) and a polarising beam splitter (PBS). The pump beam is set to the horizontal polarisation by using another HWP to trigger a type II SPDC process in the Ti:PPLN waveguide. The light is then coupled into our source through a lens-to fibre coupling to accurately determine the power injected into the source. The SPDC photons exiting the source are detected with low jitter, high-efficiency superconducting nanowire single photon detectors with detection efficiencies of $\eta_{det} = (85 \pm 5)\%$.

This is the most basic setup required to characterise the quantum properties of the source. However, in order to analyse specific features of the source, additional optical elements need to be introduced into the setup as shown in Figure 4.1 (b), (c), (d), (e),

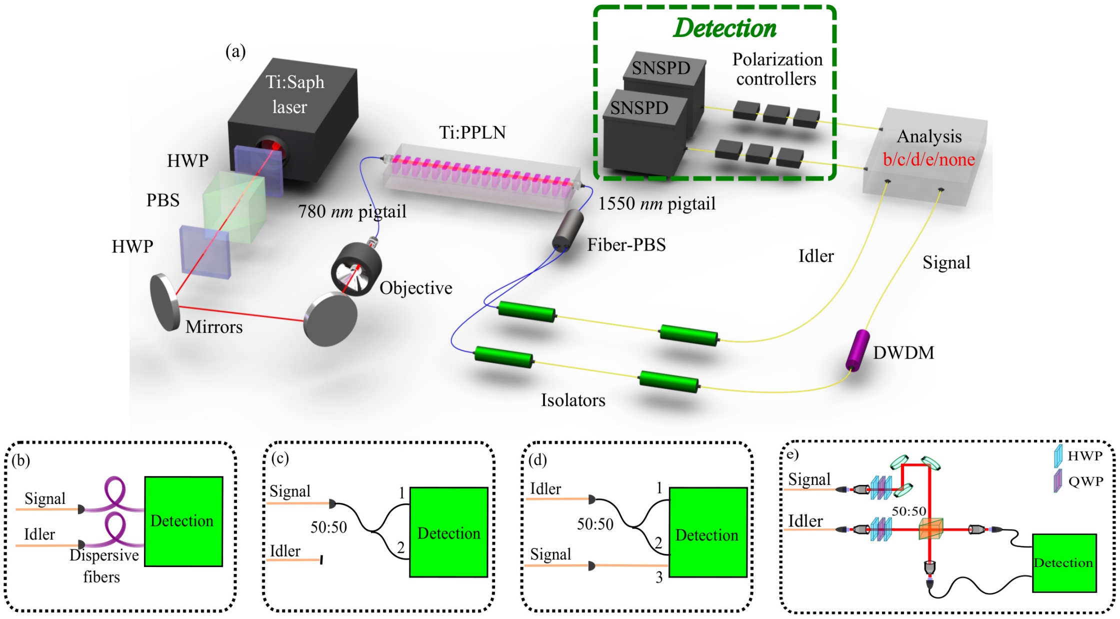

Figure 4.1.: Experimental setup for quantum characterisations: (a) Heralding efficiency measurement. (b) Joint spectral intensity measurement. (c) Unheralded $g^{(2)}(0)$ measurement. (d) Heralded $g^{(2)}(0)$ measurement (e) HOM measurement.

which will be further described in the following sections.

Our final source design includes the following components: 780-nm fibre pigtail, Ti:PPLN waveguide, 1550-nm pigtail, fibre-PBS, a pair of isolators and a DWDM filter (only in the signal arm).

4.1. Heralding efficiency

As mentioned earlier, the heralding efficiency of SPDC sources is one of the most important parameters to determine the usability of the device. The setup used to measure the heralding efficiency is shown in Figure 4.1 (a). To determine the best design of our source, we carried out an investigation of the heralding efficiency using a series of configurations. We test four different source combinations: (i) both arms are unfiltered, (ii) signal arm is filtered, (iii) idler arm is filtered and (iv) signal and idler arms are filtered. We used C-24 DWDM filters with 200 GHz channels corresponding to a bandwidth of $\delta\lambda_{DWDM}$ =1.6 nm at a central wavelength λ_{peak} ≈1558 nm. The raw heralding efficiency of the signal (s) and idler (i) photon is given in Equation 2.40 as $\eta_{s,i} = C/S_{i,s}$ where C are the coincidences between the two photons and S are the singles measured in each arm. The measured efficiency of the signal and idler arm is plotted against the input pump power in Figure 4.2. The true heralding efficiency is estimated from the y-intercept of the curves. A summary of the results collected from the four configurations is shown in Table 4.1.

It was observed that the highest heralding efficiency of $\eta_i = (46.2\pm0.6)\%$ was obtained

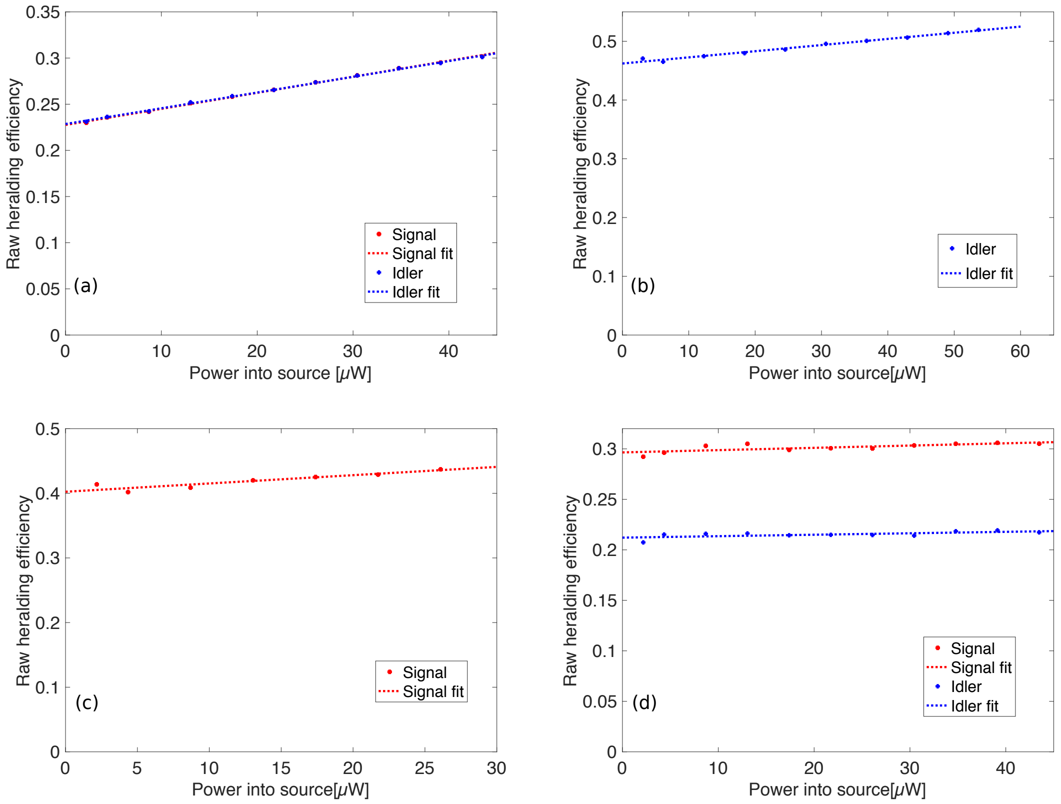

Figure 4.2.: Raw heralding efficiencies versus power coupled into the source measured when: (a) signal and idler photons remained unfiltered; (b) only signal photon was filtered; (c) only idler photon was filtered; (d) both photons were filtered.

when the DWDM filter was attached to the signal arm. This is the measured raw heralding efficiency of the source. By only correcting for the detector efficiency, and NOT the channel losses (in contrast with [58]) we estimated the efficiency of the complete device from generation to output to be $\eta_i^{corr} = \frac{\eta_i}{\eta_{det}} = (54.4 \pm 3.3)\,\%$. This value is very close to the classically estimated maximum heralding efficiency shown in Section 3.4 that can be achieved from this device ($\eta_h^{max} = (58.6 \pm 3.3)\%$). This implies that the device shows a high suppression of spurious events, a very desirable quality for "plug & play" sources. For completeness, we characterised the noise counts in the optical channel by measuring the background events. This was performed in two ways - i) by changing the polarisation to suppress SPDC and ii) by tuning the pump wavelength slightly away from the source phasematching condition. In both cases, we measured the singles count rates were approximately 9 % background noise which contributes to the slight lowering of the measured heralding efficiency with respect to the classically estimated value.

In table 4.2 we compare our device with other benchmarked photon-pair sources that exploit either type 0, I or II SPDC processes, with a focus on high heralding efficiency [60]. The state-of-the-art bulk sources show the highest heralding efficiencies so far, which comes at a price of reduced brightness. With respect to other fibre-pigtailed sources [57, 58] , our device represents the best raw and detector-corrected heralding efficiencies, but

Configuration	η_s (%)	η_i (%)	η_s^{corr} (%)	η_i^{corr} (%)
Both arms are unfiltered	22.8	22.9	26.8	26.9
Signal arm is filtered	-	46.2	-	54.4
Idler arm is filtered	40.2	-	47.3	-
Both arms are filtered	29.7	21.2	34.9	24.9

Table 4.1.: Comparison of the different configurations used to test the best design of our source with respect to raw ($\eta_{s/i}$) heralding efficiencies and detector-corrected ($\eta_{s/i}^{corr}$).

	Reference	Source	λ (*nm*)	$\Delta\lambda$ (*nm*)	$\eta_{s/i}^{corr}$ (%)	$\eta_{s/i}$ (%)
FREESPACE	Kaneda *et al* [167]	PPKTP/bulk	1590	1 - 4	87	7*
	Pomarico *et al* [168]	PPLN/bulk	1550	3	80	8*
	Krapick *et al* [169]	PPLN/wg	1575	-	60	13.8*
	Bock *et al* [170]	PPLN/wg	1312	-	64.1	16*
	Guerreiro *et al* [171]	$KNbO_3$/bulk	1550	-	74.8*	18*
	Harder *et al* [172]	PPKTP/wg	1536	5.1	80*	20.5
	Pereira *et al* [173]	PPKTP/bulk	810	0.2	84	42.5*
	U'Ren *et al* [37]	PPKTP/wg	800	2	85	51
	Weston *et al* [174]	PPKTP/bulk	1570	15	80*	64
	Shalm *et al* [175]	PPKTP/bulk	1550	-	83.1*	75.6
	Giustina *et al* [176]	PPKTP/bulk	810	-	82.7*	78.6
	Ramelow *et al* [177]	PPKTP/bulk	810	0.5	86.3*	82
PIGTAILED	Zhong *et al* [57]	PPKTP/wg	1316	1.3	13.7*	2.8
	Oesterling *et al* [58]	PPLN/wg	1550	60	30.9*	3.1*
	Ngah *et al* [59]†	PPLN/wg	1540	0.25	42	7.1
	This work	**PPLN/wg**	**1560**	**1.8**	**54.4**	**46.2**

Table 4.2.: Comparison of state-of-the-art sources taken from literature [60]. * was mathematically estimated from reported data. † shows a source that is pigtailed only on the output side.

much improvement in terms of fibre-optic component losses needs to be made to compete with bulk sources. A higher degree of optimised device integration is a possible solution, for e.g. integrated PBSs [55] and/or wavelength division multiplexers [178, 179] on chip for splitting of the photon pairs and pump suppression respectively.

4.2. Brightness and non-classicality

Source brightness is defined as the rate at which photon pairs are generated within the Ti:PPLN waveguide. It is determined by $\mathcal{B}_{chip} = \frac{S_s \cdot S_i}{C \cdot t \cdot P_{chip}}$, where t is the integration time and P_{chip} is the pump power coupled into the chip. The normalised brightness is estimated when the heralding arm is attached to a filter by $\mathcal{B}_{filtered}^{norm} = \mathcal{B}_{filtered}/\Delta\lambda_{filter}$, where $\Delta\lambda_{filter}$ is the FWHM bandwidth of the heralding arm obtained from the joint spectral intensity. Table 4.3 shows the brightness of our source at a mean photon number $\langle n \rangle \approx 0.01 \frac{\text{photons}}{\text{pulse}}$ (pump energy, $E_{pump} = 3\,\text{pJ/pulse}$) in unfiltered and filtered (before splicing to source) configurations.

Configuration	$\mathcal{B}_{chip}$ $(\frac{pairs}{s \cdot mW})$	$\Delta\lambda_{filter}$ (nm)	$\mathcal{B}_{chip}^{norm}$ $(\frac{pairs}{s \cdot mW \cdot nm})$
Both arms are unfiltered	$3.84 \cdot 10^7$	-	-
Signal arm is filtered	$1.87 \cdot 10^7$	$\Delta\lambda_s = 1.06 \pm 0.02$	$(1.76 \pm 0.04) \cdot 10^7$
Idler arm is filtered	$1.68 \cdot 10^7$	$\Delta\lambda_i = 1.07 \pm 0.04$	$(1.57 \pm 0.07) \cdot 10^7$
Both arms are filtered	$0.43 \cdot 10^7$	-	-

Table 4.3.: Comparison of chip brightness between different source configurations.

Since the best source performance was obtained when the signal arm was filtered, the final source design consisted of a fully spliced device. A small drop in the brightness to $\mathcal{B}_{filtered}^{norm} = (1.39 \pm 0.04) \cdot 10^7 \frac{\text{pairs}}{\text{s} \cdot \text{mW} \cdot \text{nm}}$ was also observed.

The source showed high generation rates, as expected from the nonlinear conversion efficiency measurement. It is higher than or similar to the brightness of other waveguide SPDC sources [55, 57, 58, 165, 172, 180]. In over two years of operation since pigtailing, we have found no degradation in the heralding efficiency or brightness of our source.

Being a quantum photonic source, it is of great importance to confirm the non-classicality of the source as mentioned in Section 2.5. This can be performed by analysing the photon number correlations between the signal and idler photons given by the second-order cross-correlation function, $g^{(2)}_{cross}(0)$. It is measured to be $g^{(2)}_{cross}(0) = \frac{C \cdot N_p}{S_s \cdot S_i} = 73.6 \pm 1.3$ at $\langle n \rangle \approx 0.01 \frac{\text{photons}}{\text{pulse}}$ where N_p is the number of pump trigger counts. This violates the Cauchy-Schwartz inequality [181] by more than 50 standard deviations which confirms the quantum nature of our source in the photon number basis.

4.3. Spectral measurement

The spectral properties of SPDC sources depend on the pump profile and the phase-matching characteristics of the waveguide as described in Section 2.4.1. The pump profile is fixed to a pulse duration of $\Delta\tau_{pump} \approx 2\,\text{ps}$ resulting in a pump bandwidth of $\Delta\lambda_{pump} \approx 0.3\,\text{nm}$ for $sech^2$-shaped pulses. SHG characterisation of the source provides information on the phasematching bandwidth and spectral degeneracy at temperature, $T = 25\,°\text{C}$.

We characterise the spectral properties of our source by implementing a fibre-based time-of-flight spectrometer [182, 183]. As shown in Figure 4.1 (b), the experimental setup consists of long dispersive fibres to stretch the various spectral components of the photon. Due to this, different wavelengths of the photon arrive at different timings on the SNSPDs. A fast time-to-digital converter (TDC) records the time-of-arrival of the photons accurately. On mapping the arrival times, we obtain a joint spectral intensity (JSI) using the coincidences between signal and idler photons. The marginal distribution of each photon can be obtained from the corresponding singles clicks, however, since this is a heralded single photon source, we plot the marginals using the projection of the JSI on each axis.

The JSI and marginal spectral distribution (Section 2.5) of the four combinations of our source are shown in Figure 4.3 - 4.6. In the case where both photons are unfiltered,

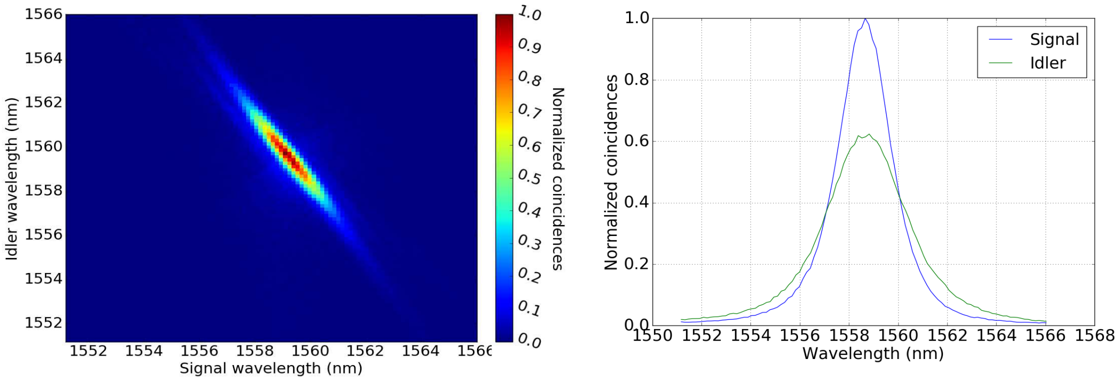

Figure 4.3.: JSI measurement of the source when unfiltered in both arms (left) and its corresponding marginals distribution (right).

we clearly observe discernible side lobes arising from the sinc-shaped phasematching curve. By using a filter separately in each arm, we are able to limit the effect of these undesirable side lobes and decrease the spectral correlations to improve the purity of the photons. As seen in the JSI and the marginals, filtering also helps to greatly decrease the background counts. When a filter is applied to the signal arm, the brightness of the source is less affected than when the filter is attached to the idler arm. This is because the signal photon has a narrower bandwidth than the idler due to the tilt in our JSI (see Figure 4.3). When filters are applied to both arms, the JSI distribution gets clipped as shown in Figure 4.6 due to the imperfect matching of the filter transmission characteristics. The measured FWHM bandwidths for all four configurations are shown in Table 4.4.

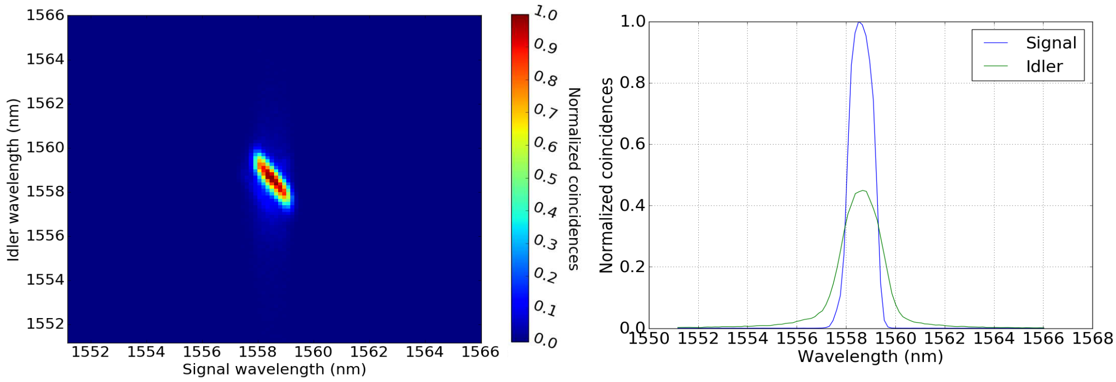

Figure 4.4.: JSI measurement of the source when signal is filtered (left) and its corresponding marginals distribution (right).

The spectral correlations of the SPDC photons provide valuable information into determining single photon coherence times and finally, their usability in quantum applications involving long distances. The coherence time of a single photon can be estimated from the temporal width of single photon wave packet. This is performed by taking a Fourier transform on the marginal spectrum of the idler photon, obtained from the JSI, after

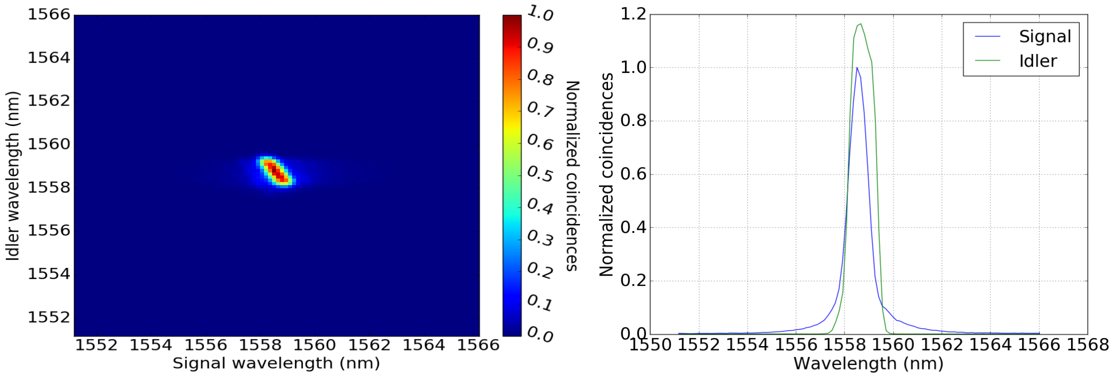

Figure 4.5.: JSI measurement of the source when idler is filtered (left) and its corresponding marginals distribution (right).

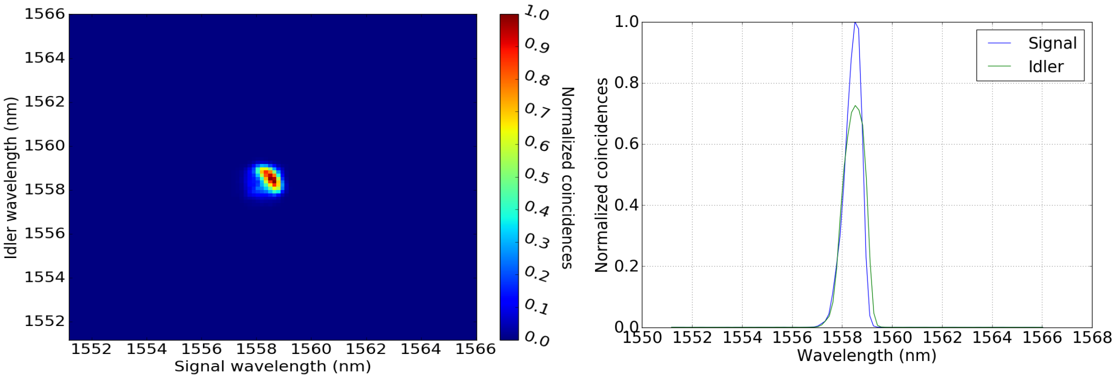

Figure 4.6.: JSI measurement of the source when both arms are filtered (left) and its corresponding marginals distribution (right).

heralding with the signal photon. We measured a coherence time of $\Delta\tau_{sp} = (5.8 \pm 0.3)$ ps for the heralded photon. This implies that at a repetition rate of 1 GHz, the idler photon can travel > 130 km in a standard optical fibre before it starts to overlap with its neighbouring pulses. Femtosecond pulses with coherence time $\Delta\tau_{sp} = 100$ fs travels a distance of one order of magnitude lower than our source for all repetition rates. Thus, picosecond sources such as ours makes for a very valuable resource for long distance quantum communication applications.

Configuration	$\Delta\lambda_s$ (nm)	$\Delta\lambda_i$ (nm)
Both arms are unfiltered	2.80 ± 0.12	3.68 ± 0.27
Signal arm is filtered	1.06 ± 0.02	1.83 ± 0.04
Idler arm is filtered	0.95 ± 0.02	1.07 ± 0.04
Both arms are filtered	0.77 ± 0.03	0.99 ± 0.03

Table 4.4.: FWHM spectral bandwidths estimated from the JSI for each configuration.

Using the JSI shown the above-mentioned figures, we can also predict the expected purity of the single photons generated from our source [184]. We estimate the spectral purity to be $\mathcal{P}_s = 0.7$ and $\mathcal{P}_i = 0.9$, when the filter is applied to the signal and idler arm respectively. Due to the tilt in our JSI, the purity of the idler photon shows higher purity than the signal on filtering. Unfortunately, filtering also reduces the brightness of the source. The purity calculated from the JSI serves as an upper bound predictions for the configurations in use. The $\mathcal{P}$ will be verified using the second-order autocorrelation function, which is a standard measure to determine the indistinguishability of photons (Refer Section 2.5).

4.4. Unheralded $g^{(2)}(0)$

An important feature for a single photon source is the spectral purity of the SPDC photons. Due to the emission of pairs of photons in SPDC, any entanglement between them can lower the purity of one photon when its twin is used as herald. A good estimate for the purity can be obtained from the JSI as mentioned in the previous Section. To quantify the purity of photons non-spectrally, we measure the degree of spectral entanglement present between signal and idler photons by the unheralded second-order Glauber function, $g^{(2)}(0)$ (as mentioned in Section 2.5). The presence of spectral correlations between the photons will lower the $g^{(2)}(0)$ from the ideal value of $g^{(2)}(0) = 2$, where a maximally entangled state will result in a Poissonian distribution with $g^{(2)}_P(0) = 1$.

The unheralded $g^{(2)}(0)$ can be measured using the setup shown in Figure 4.1 (c),where the heralding (signal) arm is attached to a 50:50 fibre coupler before being detected. The results are shown in Table 4.5. The raw $g^{(2)}(0)$, $g^{(2)}_{raw}(0) = (C_{1,2} \cdot N_p)/(S_1 \cdot S_2) = 1.07 \pm 0.03$, where $C_{1,2}$ are the coincidences between the two splitter ports, N_p are the pump counts, S_1 and S_2 are the singles counts in each splitter port. We can hence, quantify the spectral properties of our source by estimating the number of spectral modes (Refer Section 2.5) generated given by $\mathcal{K} = 1/\mathcal{P}$ where $\mathcal{K}$ is the Schmidt number. The purity of the photon is given by $\mathcal{P} = g^{(2)}(0) - 1$. In this case, we obtain $\mathcal{K} \approx \infty$ indicating a high degree of spectral entanglement between the signal and idler photons.

Configuration	photon	$g^{(2)}_{raw}(0)$	$\mathcal{P}^{raw}$	$g^{(2)}_{corr}(0)$	$\mathcal{P}^{corr}$	$\mathcal{K}^{corr}$
Both arms are unfiltered	signal	1.07 ± 0.03	0.07	1.38 ± 0.03	0.38	2.63
	idler	1.09 ± 0.03	0.09	1.41 ± 0.03	0.41	2.44
Signal arm is filtered	signal	1.37 ± 0.01	0.37	1.66 ± 0.01	0.66	1.52
Idler arm is filtered	idler	1.63 ± 0.06	0.63	1.91 ± 0.06	0.91	1.1

Table 4.5.: The measured unheralded $g^{(2)}(0)$ for all configurations. $g^{(2)}_{raw}(0)$ is the raw $g^{(2)}(0)$ value and $g^{(2)}_{corr}(0)$ is the corrected value after considering the measured noise counts [185] for each channel. The raw and corrected purity $\mathcal{P}$ and the corrected Schmidt numbers $\mathcal{K}^{corr}$ are also listed for comparison.

Since the signal and idler photons share the same joint spectrum after filtering and heralding, the purity of the heralded photon can be determined by measuring the purity of the heralding photon. When the signal was filtered, we measured $\mathcal{P}_s = 0.37$; and when the idler was filtered, we measured $\mathcal{P} = 0.63$. Both quantities are significantly lower than the value predicted from the JSI. The corresponding Schmidt number is $\mathcal{K}^{raw}_s = 2.70$

and $\mathcal{K}_i^{raw} = 1.59$, still showing large amount of correlations between the photons. The purity of the idler photon is higher, due to the tilt in the JSI.

To investigate the reduction in purity, we measured the background counts arising from fluorescence or other parasitic processes that can strongly degrade our $g^{(2)}(0)$ value. The noise counts are measured by tuning the SPDC spectrum away from the filter transmission band and recording only the triggered singles counts in both arms of the splitter. When unfiltered, both arms showed ≈ 12% noise counts. On filtering, the background events dropped slightly to ≈ 9.1% of the total singles counts. On correcting the $g^{(2)}(0)$ value to include these noise counts [185], we estimated $g^{(2)}_{corr}(0)$ which is shown in Table 4.5. The corresponding $\mathcal{P}^{corr}$ was estimated to show a significant improvement in the spectral purity of the photons. The corrected value closely matches the purity estimated from the JSI. This can be further improved by using filters of narrower bandwidth to minimise the spectral correlations but at the cost of lowering the brightness and the heralding efficiency of the source [186–188].

4.5. Heralded $g^{(2)}(0)$

The quality of SPDC-based single photon sources are highly affected by multi-photon components and noise. As described in Section 2.5, we quantify these effects by measuring the heralded $g^{(2)}(0)$ ($g_h^{(2)}(0)$). Unfiltered photons did not produce reliable $g_h^{(2)}(0)$ values due to high background noise. When the signal photon was filtered, the idler arm was attached to a 50:50 fibre coupler and then detected (see Figure 4.1 (d)) while being heralded by the signal photon. The heralded second order correlation s determined by $g_h^{(2)}(0) = \frac{C_{1,2,3} \cdot N_3}{C_{1,3} \cdot C_{2,3}}$, where the number of two- and three-fold coincidences are given by $C_{l,k}$ and $C_{l,k,m}$ respectively, where $l, k, m = \{1, 2, 3\}$ label the 3 outputs and N_3 denotes the number of events in the heralding (signal) arm. We measure $g_h^{(2)}(0) = 0.014 \pm 0.001$ at $\mathcal{E}_{pump}$ =2.4 pJ/pulse, well below the criterion in [189]. The measured value agrees well with the calculated value from multi-pair events [124, 190], $g_{h,i}^{(2)}(0) \approx 0.013$, and is thus negligibly affected by other background light. A similar $g_h^{(2)}(0)$ value of $g_h^{(2)}(0) \approx 0.015$ was obtained when the idler photon was used as the herald.

4.6. Hong-Ou-Mandel measurement

Another important feature of photon pair sources is the indistinguishability of the generated photons. As mentioned in Section 2.5, the standard method to demonstrate indistinguishability is performed by using Hong-Ou-Mandel (HOM) interference between the signal and idler photons. The setup used for HOM measurement is shown in Figure 4.1 (e). In this case, we couple the photons exiting from our unfiltered source to overlap on a 50:50 beam splitter. To precisely measure the indistinguishability of the photons, the measurement apparatus should take into consideration three main factors: (i) time of arrival, (ii) polarisation and (iii) spectrum of both photons arriving at the coupler. Since we generate orthogonally polarised photons, the waveguide induces a group velocity mismatch between the photons which causes a temporal shift between them. Also, the fibre lengths of the source are carefully measured to estimate the delays required in each

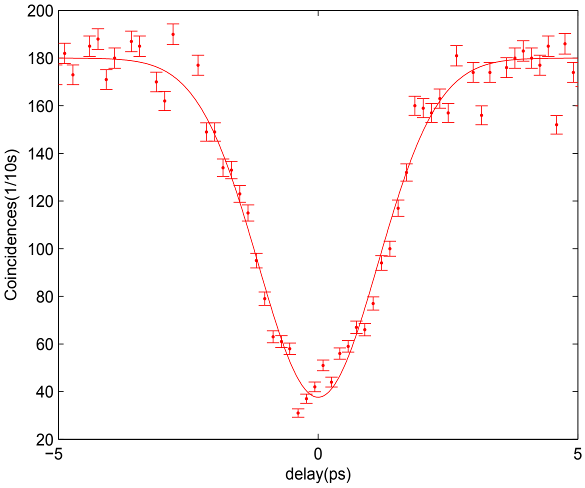

Figure 4.7.: HOM interference measurement between signal and idler photons.

arm for interference at the beam splitter. A motorised stage is introduced into the signal line to fine tune the residual difference in delays between the two photons. A half- and two quarter-wave plates are incorporated into each line for polarisation control. DWDM filters are inserted into both arms to reduce spectral distinguishability between the two photons. The source is pumped at $\langle n \rangle \approx 0.07$ pairs/pulse and the coincidences between the two interacting photons are recorded on scanning the signal delay.

The measured experimental data is reported in Figure 4.7. Indistinguishability of the photons are given by the visibility (See Section 2.5) of the HOM dip, $\mathcal{V} = \frac{C_{max}-C_{min}}{C_{max}+C_{min}}$, where C_{max} and C_{min} are the maximum and minimum coincidences recorded between the signal and idler photons. The visibility in our source is measured to be $\mathcal{V} = 0.67 \pm 0.05$, which is above the classical limit of 0.5 [189, 191] thereby confirming the quantum nature of the source. This value doesn't reach unity, meaning that there exists some distinguishability between our signal and idler photons. A cause for this reduction in the visibility arises from our 50:50 beam splitter which has a slightly imperfect splitting ratio of 47.1:52.9. However, we speculate that the main reason for the lowered visibility comes from the remaining spectral correlations that could not be removed despite the filtering, as well as a slight mismatch of the central wavelength of the two filters. The visibility can be improved by pumping the source using narrower and identical filters for spectral selection, but at the cost of lowered heralding efficiency and brightness. A more convenient solution is to pump the source with a CW laser to obtain high HOM visibilities.

From this measurement, we can also estimate the two-photon correlation time of the photon pair source. This is determined from the FWHM width of the HOM dip to be $\Delta\tau_{tp} = (5.4 \pm 0.4)$ ps. Being a picosecond source, our source suffers from low dispersion and hence highly suitable for applications involving long distance quantum communications.

Chapter 5

Spectral filtering

SPDC-based sources are one of the most commonly seen photon pair devices, where either both of the generated photons are used directly or a heralded single photon scheme is used. The biggest drawback of such sources is the spectral correlations between the signal and idler photons arising from the overlap between the pump and phasematching bands. Figure 5.1 shows the spectral correlation seen in LN where there exists an anti-correlation between the photon pairs resulting in the generation of a highly mixed state. Despite their usefulness in certain applications [192], frequency entangled states show very little promise in multi-photon interference [193–195] or entanglement-swapping experiments [196–198]. Over the years, much investigation has been done in studying the phasematching properties of materials and pump bandwidths to intrinsically generate pure states without compromising on other important source attributes like heralding efficiency and brightness [100, 115, 170, 199].

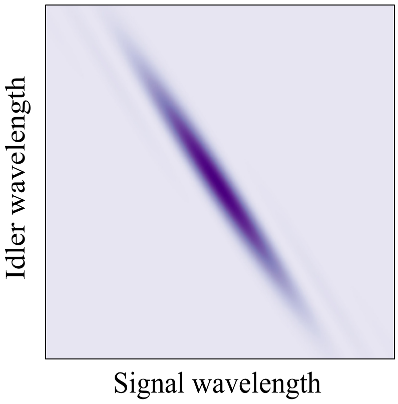

Figure 5.1.: Spectral correlation seen in LN waveguides

The spectral purity of a source depends on the angle of the JSI distribution. For e.g. telecom wavelength sources that have phasematching angles of $\theta \in [90^\circ, 180^\circ]$ results in the purity of photons, $\mathcal{P} \rightarrow 1$; in contrast LN-based sources show low purity ($\mathcal{P} \approx 0.3$) due to a $\theta = 60.5^\circ$ phasematching angle. In such sources, a convenient solution is narrowband filtering of photons to get rid of frequency entanglement by forcing only the transmission of a single spectral mode. This technique can be quite useful in heralded single photon schemes, where the purity of the heralding state is improved by filtering; and since both - the heralding and heralded photon shares the same joint spectrum, we obtain the same purity for the unfiltered heralded state as well (See Section 4.4). Such a configuration helps improve the purity of the heralded photon, while preserving the single-sided heralding efficiency and brightness of the source [157,187,200,201].

However this solution falls short when both photons are required in quantum experiments and hence, alternate schemes need to be considered when developing high quality sources. Here, we consider photon-pair sources where both photons must be generated in spectrally pure states and with high efficiencies, unlike the heralded single-photon source shown in the previous chapters, where only one photon requires a high heralding efficiency. High purity photons are crucial for high visibility interference experiments; and high heralding efficiency is critical for large data rates. One of the best methods to achieve this is by adopting source engineering strategies where we can produce intrinsically pure states by controlling the dispersion and pump bandwidths [100, 115, 117, 172, 202–208]. However, due to material and technological limitations, this solution may prove to be too cumbersome for certain crystals. An alternate solution is to place the source in a high finesse cavity which also results in the production of highly pure states without lowering the source heralding efficiency [209,210]. In most cases, filters are still needed for single-mode operation as multiple longitudinal modes are obtained due to broad phasematching bandwidths of the cavity [157,211–214]; fortunately, on using narrowband pumps and filters, a decrease in heralding efficiency is not observed because each filter intersects only with one cavity mode. For the case where both photons are to be used from non-engineered and non-cavity sources, spectral filtering is the most widely used solution. Literature hints on its incompatibility with high heralding efficiency for both photons numerous times [100, 115, 170, 202], and a simple model for heralding efficiency after filtering was developed by Reference [199]; but so far no experiments have studied the effect of filtering on purity and heralding efficiency simultaneously.

5.1. Fundamentals on filtering

As shown in Equation 2.37, the spectral features of a SPDC generated state is defined by the joint spectral amplitude (JSA) of the process. Mathematically, it is given by

$$|\psi_{SPDC}\rangle = \int\int d\omega_s d\omega_i f(\omega_s,\omega_i)\,|\omega_s\rangle\,|\omega_i\rangle \tag{5.1}$$

Equation 2.38 describes the JSA as $f(\omega_s,\omega_i) = \alpha(\omega_s+\omega_i)\cdot\phi(\omega_s,\omega_i)$ where $\alpha(\omega_s+\omega_i)$ the pump distribution with $\omega_p = \omega_s+\omega_i$ due to energy conservation and $\phi(\omega_s,\omega_i)$ is the phasematching band. Equation 5.1 does not reveal the complete quantum properties of the emitted SPDC state and hence a singular-value decomposition or Schmidt decomposition [100,215] needs to be performed on the JSA as described in Section 2.5. In LN, we get a strongly correlated state resulting in the generation of multiple longitudinal modes. A simple, effective and robust technique to suppress these higher order frequency modes is by narrowband spectral filtering which comes at the cost of increased losses. Till date, filtering has been adopted to develop high quality heralded single photon devices and entangled photon pair sources [188,194,216–219].

Equation 5.1 describing the photon-pair state after the application of filters is written as

$$|\psi_{SPDC,fil}\rangle = \int\int d\omega_s d\omega_i f(\omega_s,\omega_i)\mathcal{F}_s(\omega_s)\mathcal{F}_i(\omega_i)\,|\omega_s\rangle\,|\omega_i\rangle \tag{5.2}$$

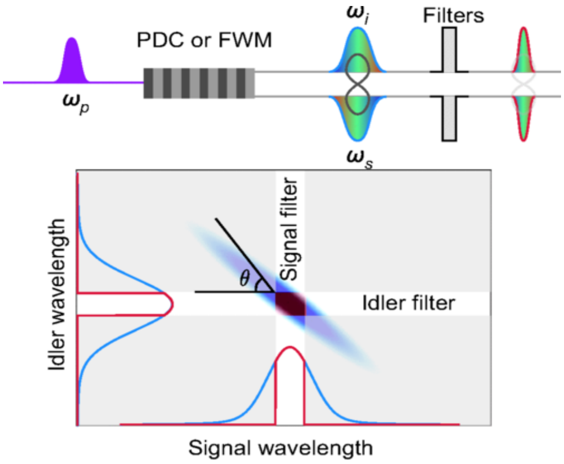

Figure 5.2.: Generation of photon pairs from PDC or FWM processes and the incorporation of spectral filters (top) and the resultant outcome when the JSI is plotted.

where functions $\mathcal{F}_s$ and $\mathcal{F}_i$ represent the spectral filters on the signal and idler photons respectively. The filter transmission profile can be of any shape: in our model however, we consider top-hat and gaussian filters. Experimentally, we measure the joint spectral intensity (JSI) which is given by $|f(\omega_s, \omega_i)\mathcal{F}_s(\omega_s)\mathcal{F}_i(\omega_i)|^2$.

To obtain an understanding on the effect of filtering, the JSI of a Ti:PPLN waveguide is modelled using the parameters of our experiment: pump bandwidth of 0.42 nm, phasematching bandwidth of 0.46 nm and phasematching angle of $\theta = 60.5°$. Figure 5.2 shows the resultant JSI overlaid with narrowband filters on the signal and idler photons. When both photons are filtered, we need to consider the pair-symmetric heralding efficiency (PSHE) which is defined as the product of the signal and idler heralding efficiencies. For a high PSHE, the two-photon amplitudes transmitted by each filter individually must overlap; otherwise, signal photons will pass through the filter without having corresponding idler photons and vice versa. Hence, we define the filtered heralding efficiency of the signal photon as the probability that the signal photon passes its filter given that the idler photon has also passed its filter and vice versa for the idler photon's heralding efficiency. Taking the probability that both photons pass their filters as Γ_{both} and the probability that each passes individually as Γ_s and Γ_i, we find the filtered heralding efficiency of the signal photon is $\eta_{f,s} = \frac{\Gamma_{both}}{\Gamma_i}$ and the idler photon is $\eta_{f,i} = \frac{\Gamma_{both}}{\Gamma_s}$. Then, the PSHE is given by $\eta_{f,s}\eta_{f,i}$. These efficiencies will drop to a value lower than 1 whenever the JSIs passed by each filter individually do not match [199, 220] and with losses in the optical channel. This would suggest the lack of filtering will present the highest PSHE for our photon source.

On the other hand, a spectrally pure state can be achieved only when the filtered JSI is uncorrelated between the two photons, meaning, the JSI should be either a circle or an ellipse oriented along the horizontal or vertical axis. From Figure 5.2 it is evident that narrower filter bandwidths improve the spectral purity unlike with PSHE. The spectral purity of either photon can be estimated using $P = Tr(\rho_s^2)$ given that both photons pass

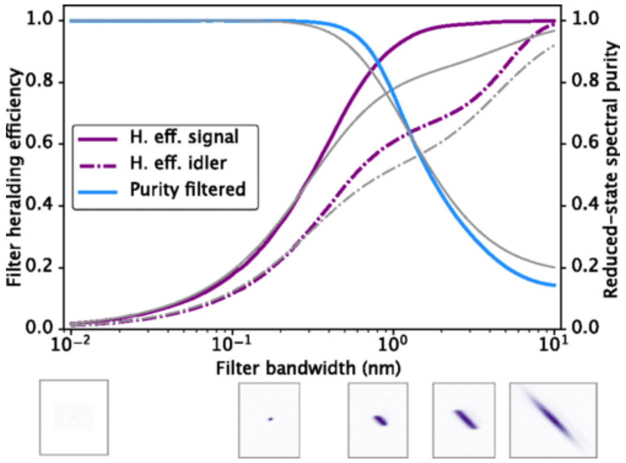

Figure 5.3.: Theoretical predictions on the dependance of the heralding efficiencies and purity on top-hat filter bandwidths. The same metrics are also investigated using Gaussian filter (grey curves). Some JSIs are also shown below their corresponding filter bandwidths (the leftmost is very small on this scale).

their respective filters, where

$$\begin{aligned}\rho_s &= Tr_i(|\psi\rangle\langle\psi|) \\ &= \int\int\int d\omega_i d\omega_s' f(\omega_s,\omega_i) f^*(\omega_s',\omega_i) \times \mathcal{F}_s(\omega_s)\mathcal{F}_s(\omega_s')\mathcal{F}_i(\omega_i)^2 \, |\omega_s\rangle \, |\omega_s'\rangle\end{aligned} \tag{5.3}$$

is the reduced density matrix. We calculate the effect of ideal top-hat filters with varying bandwidths and with perfect transmission/rejection properties on PSHE and spectral purity. Figure 5.3 shows the increment of photon purity on narrowing the bandwidth of the filter which instead causes an opposite effect on the PSHE. The kink in Figure 5.3 around 3-nm filter bandwidth in the idler heralding efficiency is due to the asymmetry of the JSI [221]. At lower filter bandwidths, the heralding efficiencies of the signal and idler photons follow the same trend. However, at larger filter bandwidths, despite the identical tuning of the filter bandwidths in both of the photon channels, the slight angle of the JSI towards the idler axis causes a higher influence of the idler filter on the heralding efficiency.

The combined effect of filtering on PSHE and spectral purity can be determined by the symmetrised fidelity [186] defined as

$$F = \sqrt{\eta_{f,s}\eta_{f,i}}\frac{2P}{1+P} \tag{5.4}$$

Figure 5.4 shows the change in the symmetrised fidelity (See Equation 5.4) with respect to the phasematching angle after optimising the pump and filter bandwidths. In this case, the phasematching bandwidth (which depends on the crystal length) does not play a role, on the other hand, the pump and filter bandwidths needs to be optimised to obtain the maximum symmetrised fidelity. For sources with phasematching angle equal to $\theta \in [90°, 180°]$, filtering is not required as the optimal filter bandwidth tends to infinity,

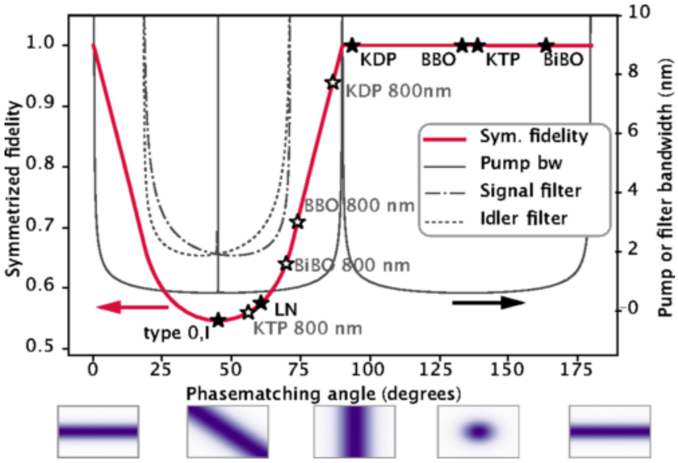

Figure 5.4.: Theoretical estimations on the dependence of symmetrised fidelity versus phasematching angles (solid red line). The pump bandwidth (black solid line) and the signal (black dot-dashed line) and idler (black dashed line) filter bandwidths are optimised to achieve the highest fidelity for each phasematching angle. Using Reference [222], degenerate type-II 1550 nm SPDC are modelled (solid stars). Data points with open stars shows non-degenerate photons at 800 nm and other wavelengths, many different phasematching angles can be achieved [223]. Unfiltered JSI plots are shown under certain phasematching angles at 45° intervals.

resulting in a symmetrised fidelity of $F \to 1$. However, when sources deviate from these phasematching angles, the symmetrised fidelity drops dramatically. On considering our source that is fabricated on a LN platform, the maximum fidelity achievable is only $F = 0.57$ due to its phasematching angle $\theta = 60.5°$. In Section 4.1, we show the importance of using filters and their resultant consequences on the heralding efficiency of the source. By applying a filter of bandwidth roughly equal to 1.5 nm to one arm did not degrade the source performance in terms of brightness but improved the heralding efficiency significantly due to background noise suppression. But when a similar filter was applied to the other arm as well, the overall heralding efficiency of the source reduced significantly. For sources like LN, filtering is absolutely crucial for removing spurious counts, but it comes at a very heavy cost in regard to the symmetrised fidelity.

To understand the impact of filtering on spectral purity and symmetrised fidelity, in Figure 5.5, we vary the signal and idler bandwidths by keeping a constant pump and phasematching bandwidth of 0.38 nm and 1.5 nm respectively. The phasematching angle of LN is taken as $\theta = 60.5°$. As predicted and shown in experiments, the highest signal heralding efficiency is obtained when no filter or a broadband filter is applied to the signal arm and a small bandwidth filter is used in the idler arm. For highest idler efficiencies, the opposite configuration is required. Hence, obtaining a high symmetrised fidelity is impossible. F is relatively constant at a mean value of approximately 0.45, and shows a maximum value of 0.57. The largest purity is achieved when extremely small filters are used in both arms, but on narrowing the filters too much, the symmetrised fidelity falls to zero.

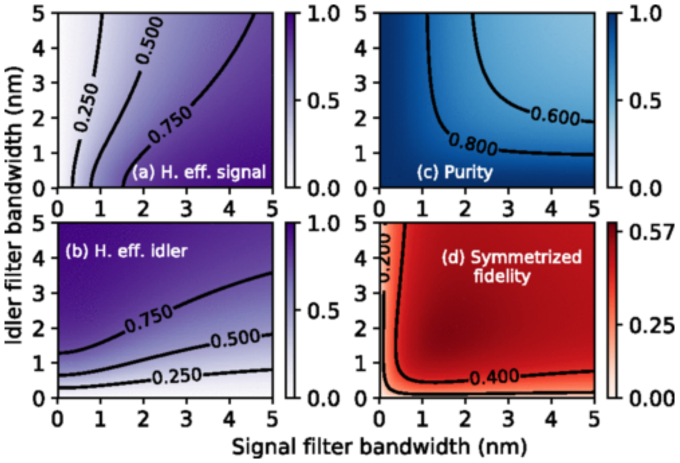

Figure 5.5.: Dependence of heralding efficiencies (a) and (b), purity (c) and symmetrised fidelity (d) on spectral filter bandwidths. On the x-axis, the FWHM bandwidths of Gaussian filters are used.

5.2. Heralding efficiency and reduced-state spectral purity

As a proof of concept, we design an experiment to measure the heralding efficiencies of the signal and idler photons and the joint spectral intensities of a SPDC-based photon pair source under varying filtering conditions. We use the unfiltered configuration of our source [60] mentioned in Section 4.1 and pumped it with mode-locked Ti:Sapphire laser at $\lambda_p = 778\,\mathrm{nm}$ with a FWHM pulse width of 3 ps. To ensure single photon operation, the source is pumped with a low pump power of $P_{pump} = 5\,\mu\mathrm{W}$ resulting in a mean photon number of $< n > \approx 0.02$ pairs/pulse before filtering. The output of the source is coupled to a WaveShaper 4000 (Finisar Corp.) which is used as spectral filters and to separate the non-degenerate photons at central wavelengths of $\lambda_s = 1562\,\mathrm{nm}$ and $\lambda_i = 1549\,\mathrm{nm}$. The singles and coincidences are recorded before and after passing the photons through a time-of-flight fibre spectrometer [182, 183] shown in Figure 4.1 to measure the PSHE and joint spectrum (to estimate spectral purity) respectively.

Filter characteristics

The spectral properties of the Waveshaper was determined by injecting light from a broadband white light source into the filter and measuring its output using an optical spectrum analyser. Figure 5.6 shows the output characteristics of the Waveshaper by varying the transmission bandwidth of the filter. We confirm that the peak filter transmission is independent of the Waveshaper's filter bandwidth and the transmission characteristics are nearly square for all filter settings. The transmission losses of the Waveshaper was measured to be 4.8 dB and 4.4 dB for the signal and idler photon respectively.

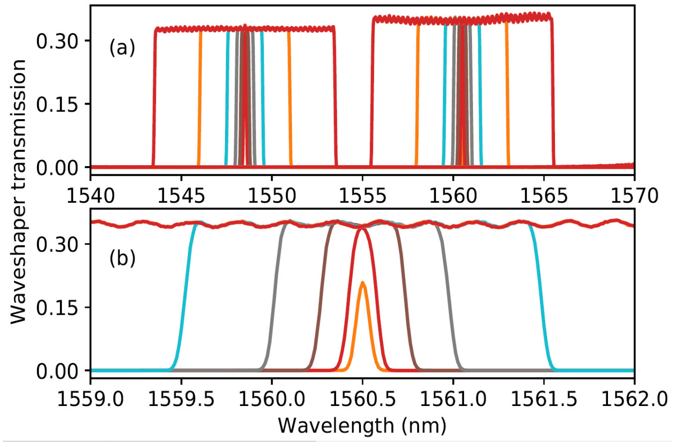

Figure 5.6.: Measured transmission of the WaveShaper for various top-hat filter settings. (a) shows the full bandwidth of the signal and idler filters for each filter setting and (b) shows a closer inspection of the output characteristics of the signal filter. It is observed that the peak transmission is constant for all settings $> 0.2\,\mathrm{nm}$.

Results

The heralding efficiency (or Klyshko efficiency) of the source is estimated using $\eta_s = C/S_i$ and $\eta_i = C/S_s$ for the signal and idler photons respectively (same as in Section 4.1). However, since the addition of filters to each photon causes higher losses than an unfiltered arrangement, a normalisation factor is incorporated to compensate for the loss-induced-reduction of heralding efficiencies. The filter heralding efficiency becomes,

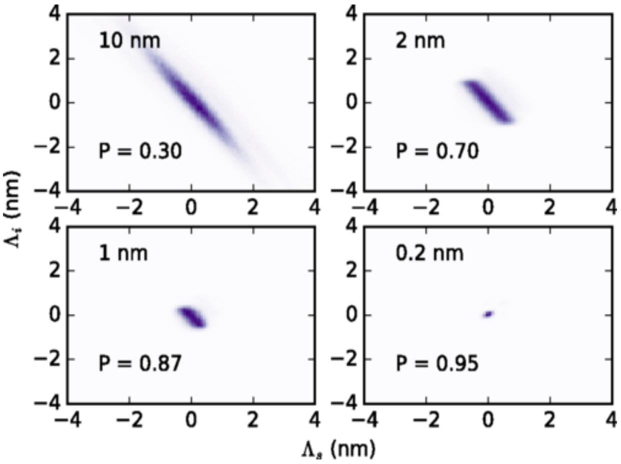

Figure 5.7.: Joint spectral intensity measurements when various filter bandwidths are used. A 10 nm filter shows a nearly unfiltered state since our marginal bandwidth is significantly lower and a 0.2 nm filter yields a spectrally pure state. The x-axis label Γ gives the spectral detuning from the phasematching peak.

$$\eta_s = \frac{C}{\eta_{max,s} S_i}, \quad \eta_i = \frac{C}{\eta_{max,i} S_s}$$

where, the normalisation term ($\eta_{max,s}$ or $\eta_{max,i}$) is determined by estimating the heralding efficiency when the filters are set to maximum bandwidth.

We characterised the purity by using the JSI and assuming a constant phase of the joint spectrum [207]. The purity is calculated using $P = Tr(\rho_a^2)$, where ρ_a is the reduced spectral density matrix of the signal or idler photon [184]. By using a high resolution spectrometer in our experiments, we reduce artificial smoothing effects that can induce errors in our estimation. Figure 5.7 shows the measured JSIs and its resultant purity when four different filter bandwidths are used, *i.e.* 10 nm, 2 nm, 1 nm and 0.2 nm. An additional time filter of twice the filter bandwidth is used during post-processing to remove noise arising from laser instabilities and limited timing resolution of our spectrometer. The highest purity is observed when the filter bandwidth is 0.2 nm, which corresponds reasonably well with the theoretical estimation shown in Section 5.1.

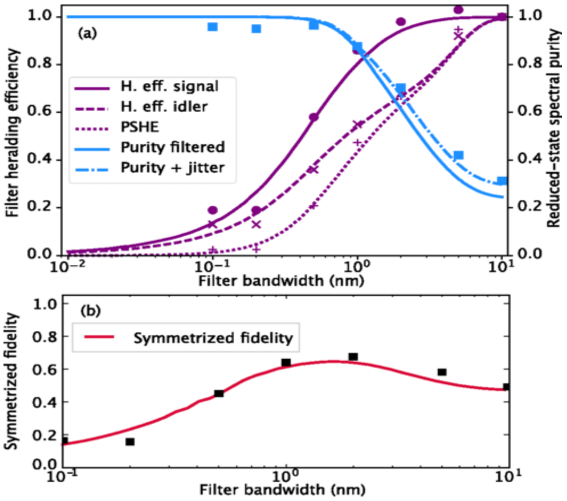

Figure 5.8.: Experimental results showing the dependence of heralding efficiency, PSHE, and spectral purity (a) and symmetrised fidelity (b) versus filter bandwidth. The black data points in (b) shows measured values and the theoretical estimation is shown in a red solid line.

A detailed investigation on the dependence of purity, filter heralding efficiencies, and symmetrised fidelity on filter bandwidth are plotted in Figure 5.8. The results match well with the estimations made in Section 5.1. Minor deviations of the experimental results from the theoretical calculations, especially in the case of large filters, may arise from the detector jitter (approximately equal to 120 ps) or the WaveShaper transmission. By accounting for these two factors in the theoretical JSI, the calculated purity matches perfectly with the experimental measurements of large filters. From theory as well as experiment, the conclusion remains the same - the increase in purity is achievable only by using small bandwidth filters, which results in a lowering of the heralding efficiency. This means that filtering is not the solution to obtain high symmetrised fidelities in heralded single photon sources.

Chapter 6

Future work

The 'plug & play' source presented here is designed to produce telecom wavelength photons at room temperature by using a pulsed pumping system as an input. It shows a high heralding efficiency and brightness along with low noise components when operating in the single photon regime, making it suitable for quantum information protocols and long-distance communication. Its simplistic design provides a good platform for further technological advances in terms of integration of optical components like polarisation beam splitters (PBSs) and wavelength division multiplexers (WDMs) on chip. This source also provides the opportunity to make proof-of-principle tests (for e.g. in chapter 5) due to its ease in handling, flexibility and convenient integration with fibre networks.

6.1. Pulsed vs CW measurements

To obtain a complete understanding on heralding efficiency as a metric for benchmarking sources, we assembled a second fibre-pigtailed source and pumped it with 'pulsed' and 'CW' lasers. The heralding efficiency of the source is characterised using the same setup as shown in Figure 4.1 (a). The pumping laser in the 'pulsed' configuration is the same as in the previous measurements. For 'CW' measurements, we use a Ti:Sapph laser that is modulated to produce 100 ns pulses, which is used as a trigger for SPDC generation. The source configurations chosen remain the same as mentioned in Section 4.1. The measurement outcome is listed in table 6.1.

	PULSED				**CW**			
Configuration	η_s (%)	η_i (%)	η_s^{corr} (%)	η_i^{corr} (%)	η_s (%)	η_i (%)	η_s^{corr} (%)	η_i^{corr} (%)
Both arms are unfiltered	29	24	32	27	20	20	22	22
Signal arm is filtered	-	36	-	40	-	26	-	29
Idler arm is filtered	44	-	49	-	31	-	34	-
Both arms are filtered	23	21	26	23	22	22	24	24

Table 6.1.: Comparison of raw ($\eta_{s/i}$) and detector-corrected ($\eta_{s/i}^{corr}$) heralding efficiencies when different source configurations were pumped with 'pulsed' and 'CW' light.

The maximum heralding efficiency was determined classically (as mentioned in Section 3.4.1) by measuring the losses of each optical component used. The losses are as follows: (i) waveguide losses: α_{TE} =0.15 dB cm^{-1} and α_{TM} =0.2 dB cm^{-1}, (ii) pigtailing efficiency: $\eta_{FC,TE} = 84\%$ and $\eta_{FC,TM} = 80\%$, (iii) spliced fibre-PBS and isolators transmission: $T_{PBS,TE} = 75\%$ and $T_{PBS,TM} = 71\%$, and (iv) an additional fibre connector losses of $\alpha_{conn} = 10\%$ (since the fibre components in this source are not spliced together). TE and TM is considered as the signal and idler photon respectively, same as in the measurement with the first source. The maximum raw heralding efficiency for each photon is estimated using $\eta_{s/i}^{calc} = T_{wg,s/i} \cdot T_{FC,s/i} \cdot T_{PBS,s/i} \cdot T_{conn}$. We obtain $\eta_s^{calc} = 54\%$ and $\eta_i^{calc} = 48\%$ as the maximum classically-estimated raw heralding efficiency for the signal and idler photon.

The measured detector-corrected heralding efficiency, $\eta_{s,i}^{corr}$ has an error of roughly 4 % due to fibre connector and splicing errors. We observe that the 'pulsed' heralding efficiencies are very close to the classically estimated values, however, 'CW' measurements show a reduction of 10 - 13 % in comparison. We speculate that the lowered heralding efficiency in the 'CW' case arises from fluorescence counts being produced due to long pump pulse durations. To investigate this, we measure the accidental counts within different detection-coincidence windows: here, 2 ns, 5 ns and 10 ns for both measurement types. In a 'pulsed' pumping mode, when signal and/or idler arms are unfiltered, we measure a background noise of about 15 %; and when filtered, we measure roughly 5 % of noise counts. For 'CW' measurements, we obtain roughly 2 % lower accidental counts than the 'pulsed' values when the signal and/or idler arm are unfiltered and filtered. Preliminary examination of the source shows no conclusive evidence towards the reason behind the lowered heralding efficiency in 'CW' measurements.

Historically, researchers have been comparing source performance irrespective of the pumping source, *i.e.* 'CW'- or 'pulsed'- pumping systems. The discrepancies in the two have never been noted before and hence a thorough study of SPDC generation processes in both cases should be conducted to confirm and verify this effect.

6.2. Integrated structures

In this work we focus on realising a fully fibre integrated source consisting of a Ti:PPLN channel waveguide. Here, the waveguide is designed to support the fundamental mode for SPDC wavelengths; this results in the waveguide guiding at least three optical modes for the pump. To optimise coupling to single mode fibres and improve source brightness, waveguide tapers suitable for fundamental mode guiding of the pump wavelength must be fabricated. These tapers should show adiabaticity in propagation such that there is high pump mode overlap with the already existing waveguide structures suited for telecom wavelengths. Preliminary simulations suggest an initial taper width, $w_{taper} \approx 3\,\mu m$ and taper length, $l_{taper} \approx 10\,mm$ for adiabatic mode expansion of the pump mode to match a 7 µm waveguide designed for 1550 nm wavelength.

Further integration of our source can be performed by replacing the fibre-PBS that is used to split the SPDC photons with an integrated PBS structure. These fibre-based components introduce a loss of ≈ 1 dB to the SPDC photons. Since quantum devices are highly susceptible to losses, we should adopt schemes for on-chip integration of PBSs or BSs to separate SPDC photons [54–56, 224] dependant on the process type. To couple photons out of the chip, a dual-fibre pigtailing protocol can be developed [224] to obtain the highest coupling efficiency through both outputs. A further step of scaling-up is

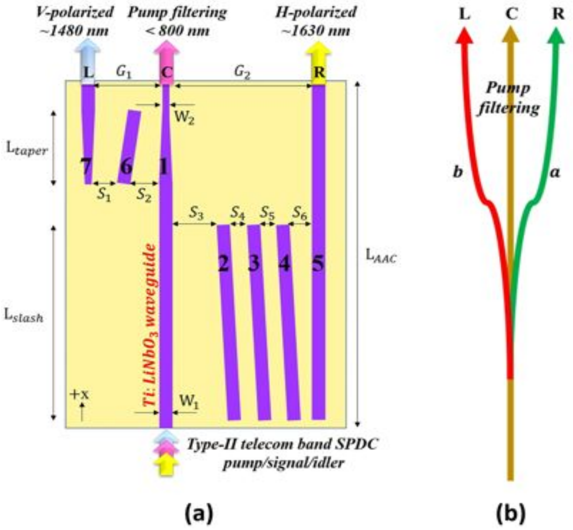

Figure 6.1.: (a) Device schematic of an integrated adiabatic waveguide polarisation-mode splitter for efficient splitting of interacting fields in a type II SPDC process [56], (b) shows the guiding paths for the v- (L) and h- (R) polarised and pump (C) wavelengths.

possible by integrating WDM couplers to remove the pump as shown in Figure 6.2. By minimising the number of interfaces and optimising each element, we can significantly reduce the losses, thereby improving the quantum efficiency of the final device.

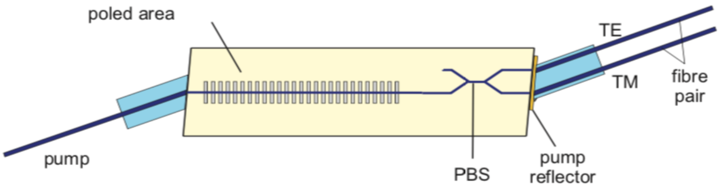

Figure 6.2.: Device schematic for dual fibre pigtail attached to the output end-facet of the chip to collect signal and idler photons after separation [224].

6.3. Cold temperature devices

One of the most advantageous properties of Ti:PPLN waveguides is its frequency tunability by accessing different phasematching conditions by varying temperatures. This is possible due to the temperature-dependent refractive index change expressed by the Sellmeier Equations [65,66] for TE and TM polarisations. The measured SHG peak wavelengths by temperature tuning is plotted in Figure 6.3 (a). We estimate a $-0.14\,\mathrm{nm}\,^{\circ}\mathrm{C}^{-1}$ shift in our source between 20 °C and 70 °C; the temperature tuning is limited by the TEC element used and the stability of the UV curing glue (NOA81) used for pigtailing. The resultant SPDC phasematched wavelengths are shown in Figure 6.3 (b).

The device operation at these temperatures are well-established, however investigations

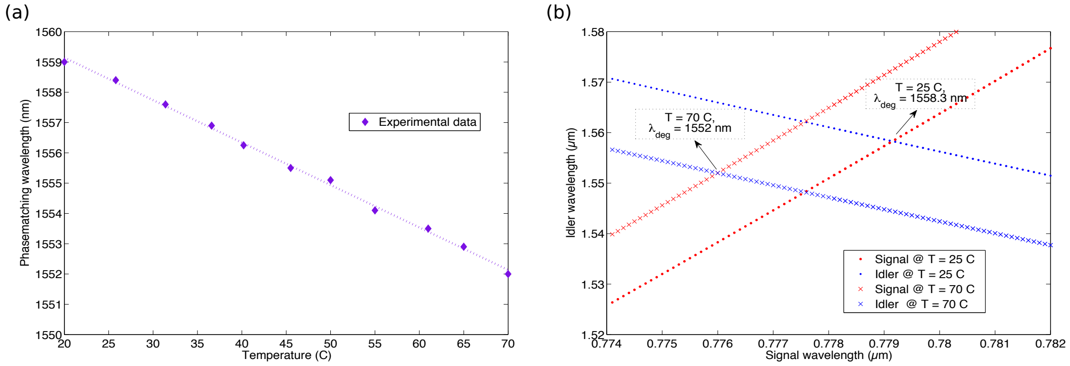

Figure 6.3.: (a) Type II SHG phasematched wavelength tunability with respect to temperature of a Ti:PPLN waveguide, (b) shift in the degenerate SPDC wavelength of our source estimated from the temperature tunability measured from SHG

on source performance at cryogenic temperatures have only recently begun [225–227] . Since high efficiency detectors like SNSPDs and transition-edge sensors (TESs) operate at superconducting temperatures, integrated source-detector chips for low-power optical processing units must be built at these temperatures. One of the main challenges reported is the lowering of detector performance on chip-integration with respect to detection efficiency and polarisation sensitivity. Major investigations are being conducted on the detector material and design structure to improve these metrics of an on-chip detector. Smirnov *et al* [228] reported the highest detection efficiency so far of 6 % for NbN SNSPD-LN chips. Höpker *et al* [227] demonstrated the fabrication and measurement outcomes of tungsten (W) TESs on titanium indiffused LN waveguides. Here, a fully-integrated chip was constructed by having the input and output of a waveguide pigtailed using standard telecom fibres. A maximum detection efficiency of 0.8 % was reported for W TES-Ti:LN waveguide detector.

Chapter 7

Conclusion

Following the increasing demand of stable, efficient, and reliable quantum devices for quantum-information applications, we experimentally demonstrate an efficient picosecond heralded single-photon source via type-II SPDC in Ti:PPLN waveguides. The Ti:PPLN waveguide was designed to generate telecom SPDC photons using a 780 nm pump input. The source is fully integrated with commercially available fibre components: fibre-PBS for photon separation, DWDM filter for spectral filtering and C-band isolators for pump suppression. The combined unit was packaged with an aluminium housing to ensure device protection and ease of usage.

The optimal properties of the Ti:PPLN waveguide was modelled using RSoft FemSIM package to produce low-loss waveguides in the TE and TM polarisations and maximal waveguide to fibre coupling. The titanium strip width and thickness, and indiffusion conditions applied to the software resembled the fabrication procedure used in the cleanroom. The poling period required for the afore-mentioned process was calculated using energy and momentum conservation laws, and Sellmeier Equations for temperature-dependent bulk LN refractive indices. The estimate poling period of $\Lambda \approx 9\,\mu\text{m}$ was fabricated on chip with small variations to adjust for the waveguide-induced refractive index change. The losses and nonlinear conversions of the waveguides were tested to determine the best waveguide for pigtailing.

For maximal transmission and suppression of the SPDC and pump photons respectively, anti- and high-reflective coatings were then deposited at the end-face of the waveguide chip. The chip showed a transmission of 95 % for telecom wavelengths and a 22 dB suppression for pump wavelengths with respect to air. Since the coatings were designed for optimal transmission of light from waveguide to fibre, the measured output characteristics are a slight under-estimation of the tailored design. The best waveguide was then pigtailed at the input and output end facet to show a pump coupling efficiency of $\eta_{pump} > 30\%$ and a 1550 nm coupling efficiency of $\eta_{TE} = 83.8 \pm 1.8\%$ and $\eta_{TM} = 75.7 \pm 1.6\%$ for TE and TM polarisations. The source has shown stable operation since the year 2016.

Quantum characterisation of the source was performed with different configurations to indicate the best schematic for the single photon operation. The measured detector-corrected heralding efficiency of the idler arm $\eta_i^{corr} = 54.4 \pm 3.3\%$ showed the best performance, solely limited by the losses of the fibre-optical components. For further improvement of the heralding efficiency, structures like PBSs and/or WDM couplers need to be integrated on chip to reduce interface losses. The joint spectral intensity of different source configurations were measured to determine the photon bandwidth and single-photon coherence time. The duration of the photon wavepacket was estimated to be $\tau_{sp} = 5.8 \pm 0.3$ ps, thereby confirming the long coherence time of the generated photons. Furthermore, the spectral purity and multi-photon contributions were measured using Glauber's correlation functions. The highest spectral purity of $\mathcal{P} = 0.91$ was obtained when the idler photon was filtered, but at the cost of lowered brightness. When the signal arm was filtered, we measured a brightness of $\mathcal{P} = 0.66$. The contributions from multi-photon pair emissions were low in both these configurations. The Hong-Ou-Mandel interference measurement revealed a visibility of $\mathcal{V} = 0.67 \pm 0.05$ which proves the quantumness of our source. The two-photon correlation time of $\tau_{tp} = 5.4 \pm 0.4$ ps was measured using the FWHM of the HOM dip. The effects of spectral filtering on pair-symmetric heralding efficiency and spectral purity is also investigated. Our results suggest that filtering is not the best solution to obtain high heralding efficiencies of photon pairs and only broadband filters should be used for noise reduction. Instead of spectral filtering, optimal cavity structures, time-frequency filtering or optimised source engineering techniques should be used generate spectrally decorrelated states.

Finally, we discuss the future outlook of this work. Probing measurements with CW and pulsed pumping systems revealed a $10 - 13\%$ lower heralding efficiency with a CW pump. This was confirmed by a second fibre-pigtailed source with the same characteristics as the first. The accidental counts due to fluorescence and other parasitic effects in both pumping measurements revealed no useful information to explain this discrepancy in the heralding efficiency. We also discuss further integration of components like PBSs, WDM couplers and single photon detectors on chip.

Part B.

Compressive sensing for characterising high-dimensional states

Chapter 8

Introduction

Over the past few decades, the world has seen an increasing need for computational and information processing power to help solve complex problems in the fields of science and technology [229–242], data security [5, 16, 17, 36, 243–247] and even, economics [248, 249]. Conventional computers has been an ingenious device which so far has played a leading role in every application known to man. Unfortunately, present-day computers are classical systems that are heavily restricted by its physical specifications [250, 251]. This implies that physical systems rely on their hardware architecture (for e.g. computer processors) for information processing. This introduces serious obstacles as the speed of such systems are limited by the

- energy required to process data - large amounts of data requires high processing power, which causes severe heating of hardware and hence, increases costs for additional hardware for cooling [252, 253]
- the number of degrees of freedom possessed by the particle, also known as particle dimensionality, used for data transfer - electrons used in present-day devices are binary states, therefore complex algorithms has to process copious quantities of data which increases the processing time significantly. [254–256]

A variety of technologies - most recent and successful of them being integrated circuits [257–259], have come push the boundaries of Moore's law [260] which has enabled massive processing rates otherwise deemed to be impossible. Despite this gross progress, at some point classical computers will become obsolete.

Quantum mechanics has long been predicted to be the solution to realise tasks considered to be hard with classical approaches. Major advances have been made in various areas of research like communication [229, 261–263], cryptography [17, 246, 264, 265] and simulation [230–232, 235, 238, 266], thereby proving the indispensability of quantum technologies. Primary candidates used for encoding quantum information are photons [267–272], electron or nuclear spins [273–279], superconducting circuits [280, 281], solid-state devices [282–284] etc. Unlike classical bits (*i.e.* 0 and 1), quantum bits or qubits include 0, 1 and all coherent superpositions of the two, thereby theoretically increasing the dimensionality of the encoded particle to near infinity.

The challenge in using quantum states lies in the ability to:

i. manipulate these different dimensions in particles
ii. route the encoded data through an inert medium
iii. decode it with high accuracy.

i. has been implemented in physical systems by accessing different degrees of freedom of particles to encode and decode qubits. Table 8.1 shows a list of a few major particles and their possible encoding methods. Each encoding method offers advantages/drawbacks and must be carefully chosen dependant on the application. Multiple degrees of freedom can also be used to create hybrid platforms for encoding data that results in the generation of very high-dimensional states for information processing but at the cost of increased complexity in decoding protocols.

Particle	**Degree of freedom**	**Encoding**
Photons	Number	0 / 1 photons
	Polarisation	Horizontal / Vertical Diagonal / Anti-diagonal
	Spectral or temporal	Time-of-flight
	Spatial	Multiple optical modes on / off x, y co-ordinates
	Orbital angular momentum	Left / Right
Electrons	Spin	up / down
	Charge	0 / 1 electrons
Atoms	Spin	up / down

Table 8.1.: A list of a few particles whose degrees of freedom can be accessed to encode information.

With regards to ii., photonic states present several advantages over other platforms as mentioned in Chapter 1. It has been demonstrated that on increasing the dimensionality of single photons, larger amounts of data can be encoded into the state, which can reduce the particle requirement significantly [285]. Consequently, high-dimensional photonic states represent important information resources. As for iii., the apparatus required to extract information from the carrier particle will depend on the degree of freedom and type of encoding used. In this work, we use two methods - direct measurement technique or raster-scan and compressive sensing (CS), to decode spatial degree of freedom and a time-of-flight spectrometer [182, 183] to discretise the spectral degree of freedom of photonic states.

Organisation of Part B: Chapter 9 reviews the fundamental knowledge on signal processing tools described in this thesis. The advantages and drawbacks of the raster-scan and compressive methods are briefly explained. Using these methods, SPDC modes are reconstructed in Chapter 10 in the spatial and spectral domains. The dimensionality and fidelity of the reconstructed states are presented. The correlations between the spatio-spectral modes are also demonstrated here. Chapter 11 provides a conclusion of our results and the possible future impact.

Chapter 9

Basics

Signal processing (or image reconstruction) is a broad field with a variety of problems ranging from resolution-related effects resulting in blurry images to low-light exposures that causes noise. Here, we discuss the raster-scan and compressive sensing methods for image reconstruction.

9.1. Direct measurement or raster-scan

Raster-scanning method is a technique for reconstructing an image by sweeping the imaging sensor in a line-by-line manner, equivalent to a data mapping scheme between one and two dimensional spaces. In this method, scans are carried out on the entire area of the imaging sensor generally from left to right while progressing from top to bottom as shown in Figure 9.1. Raster-scanning is the underlying mechanism behind most of today's display and video devices as it is a simple method which produces high quality images. The refresh rate of this technique is independent on the information contained in the image and hence this is the best method to project complex images. Unfortunately, for large data applications, the processing speed is quite low and the memory required for data storage is very high.

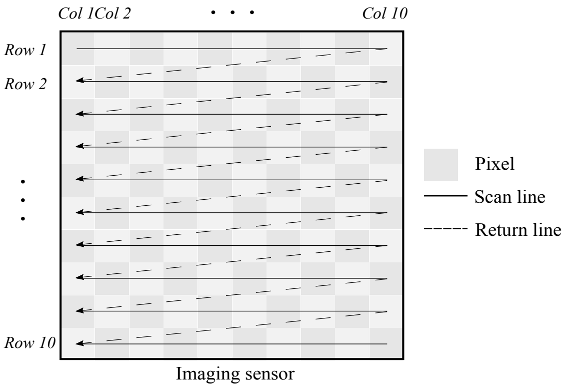

Figure 9.1.: Process of data mapping through raster-scanning method: Here, the imaging sensor consists of 10 × 10 pixel array. The image projected on the sensor is retrieved by measuring the output from individual pixels. This method collects data pixel-by-pixel from a single row; on reaching the last pixel on the sensor, the scan line is returned to the first pixel of the consecutive row. This action is performed until all pixels are scanned on the sensor array.

9.2. Compressive sensing

Compressive sensing is a measurement technique that was first introduced by Candes *et al* [286] and Donoho [287] by developing a mathematical approximation for signal processing. The key idea behind this method is to recover signals which are either sparse or compressible. Sparsity expresses the notion that most signals contain information that may be represented with only a few significant elements rather than the total composition of the signal. A suitable example is shown in Figure 9.2 [288]. Although nearly all pixels have non-zero coefficients, it is evident that only few coefficients (large peaks in Figure 9.2 (right)) capture most of the information.

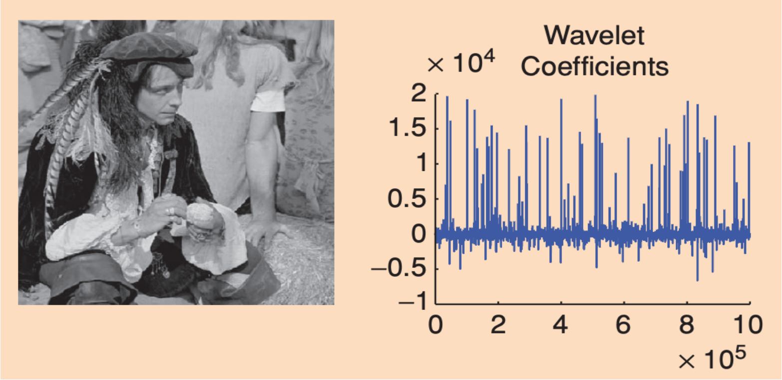

Figure 9.2.: The original image (left) and its wavelet transform coefficients in random order (right).

Information present in such sparse sets of data was conventionally acquired by sampling using the Nyquist-Shannon theorem which essentially set a minimal limit on the sampling rate (number of samples per second) to acquire reliable signal reconstructions [289]. Regrettably, this method proved to be too tedious since the number of samples required were significantly higher than the relevant information contained within the signal. The compressive sensing method solved this problem by computing only the necessary coefficients for all samples and recovering signals by retaining only large coefficients that contained information. A comparison between the Nyquist sampling method and compressive sensing is shown in Figure 9.3 [290].

Theory

The theory behind CS can be mathematically described as follows: Consider a sparse input signal x where $x \in \mathbb{R}^n$ with a signal length of n. The number of measurements m, where $m \ll n$, is the sampling rate of the reconstruction process. The size of m is dependent on the sparsity of the input signal. The data acquisition and reconstruction model used in CS is well demonstrated in [290] (as shown in Figure 9.4). Firstly, the input signal x interacts with a sensing matrix φ with length $m \times n$ to produce an m-dimensional measurement matrix y,

$$y = \varphi x \tag{9.1}$$

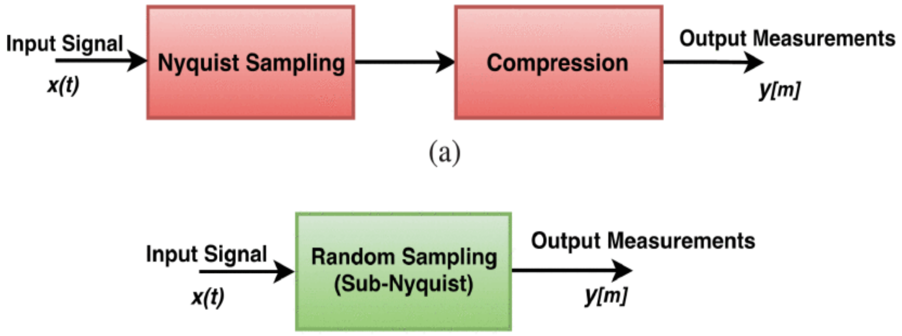

(a)

(b)

Figure 9.3.: (a) The Nyquist sampling model and (b) compressive sampling technique [290].

and x can be reconstructed using

$$x = \varphi^{-1} y$$

.

Figure 9.4 [290] shows the process used for image reconstruction using CS. Since CS requires small sampling rates and uses only relevant information in the measurement data, the reconstruction algorithm only produces an approximation of the true image. This means, the recovery step produces only a sparsifying basis (ψ) of the signal x given by

$$x = \sum_{i=1}^{n} s_i \psi_i = \psi s$$

where $s \in \mathbb{R}^n$ is the sparse coefficient of length n. To reconstruct the signal, CS uses a minimisation technique (ℓ_1- norm) to select the sparsest signal ($\hat{s}$) that is consistent with all the measurements. This optimisation is carried out by the total variation of augmented Lagrangian alternating direction algorithm (TVAL3) [291]. Thus the solution is:

$$\hat{s} = \arg\min_{s} ||s||_1$$

where $||s||_1$ is the ℓ_1- norm of s, representing the absolute sum of elements of the vector. Through CS, the original signal x can not be determined since it has an infinite number of possible solutions.

SPDC state reconstruction using CS: Down conversion processes result in the generation of photons that are correlated in various degrees of freedom. In this work, we investigate the advantages offered by CS technique in reconstructing photonic features in the spatial and spectral degrees of freedom. The photon pairs generated through an SPDC process can be described using these features as shown in Equation 9.2.

$$|\Psi\rangle = \sum_{\omega=1}^{D_\omega} f_\omega \left|\omega\right\rangle_s \left|\omega\right\rangle_i \otimes \sum_{j=1}^{D_j} s_j \left|x_j\right\rangle_s \left|x_j\right\rangle_i \, , \tag{9.2}$$

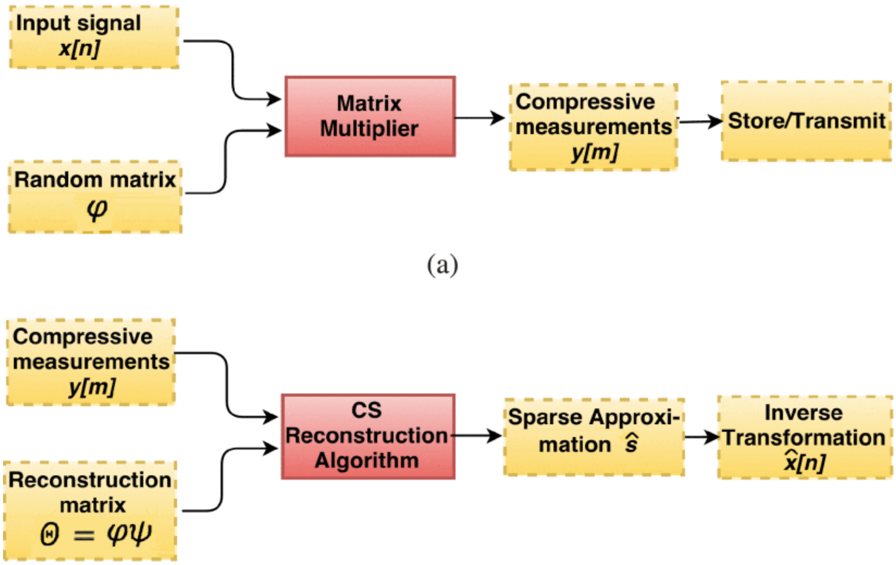

(a)

(b)

Figure 9.4.: CS acquisition [290] (a) and reconstruction (b) model.

where f_ω and s_j is the probability of finding a signal (idler) photon in a given frequency mode $|\omega\rangle_{s(i)}$ and spatial (in this work, "pixel" states) mode $|x_j\rangle_{s(i)}$ respectively.

Experimentally, as shown in Section 10.1, we use a series of sensing matrices (projected on a DMD) given by $\hat{A}$ to probe interesting features of our SPDC state (here, the spatial and spectral degrees of freedom). The measured state, $|\phi\rangle$ is given by

$$|\Phi\rangle = \hat{A}\,|\Psi\rangle = \sum_{\omega=1}^{D_\omega} \hat{T} f_\omega \,|\omega\rangle_s \,|\omega\rangle_i \otimes \sum_{j=1}^{D_j} \hat{O} s_j \,|x_j\rangle_s \,|x_j\rangle_i \,. \tag{9.3}$$

The spectral operator $\hat{T}$ uses the time of arrival (can be obtained from a time-of-flight spectrometer, similar to the one used in Section 4.3) to map the spectral components of SPDC photons. The spatial operator $\hat{O}$ uses the pixel basis of the DMD to map the spatial profiles of the photon pairs. D describes the dimensionality of the frequency (ω) and spatial (j) bins. Since we use only 'm' number of measurements to successfully reconstruct our SPDC photons, Equation 9.3 reduces to

$$|\Phi\rangle = \sum_{t=1}^{D_t} \hat{f}_t \,|t\rangle_s \,|t\rangle_i \otimes \sum_{j=1}^{D_j} \sum_{l} \hat{O}_{m,l} s_j \,|x_l\rangle_s \,|x_l\rangle_i \,. \tag{9.4}$$

where l represents a pixel index.

We can re-write this equation in the form $\hat{\Phi} = \hat{S}\hat{\psi}$ as described in Equation 9.1. The full representation is shown in Equation 9.5.

$$\begin{pmatrix} \phi_1 \\ \phi_2 \\ \vdots \\ \phi_M \end{pmatrix} = \begin{pmatrix} A_{1,1} & A_{1,2} & \dots & A_{1,N} \\ A_{2,1} & A_{2,2} & \dots & A_{2,N} \\ \vdots & \vdots & \ddots & \vdots \\ A_{M,1} & A_{M,2} & \dots & A_{M,N} \end{pmatrix} \begin{pmatrix} \psi_1 \\ \psi_2 \\ \vdots \\ \psi_N \end{pmatrix} . \tag{9.5}$$

The input state $\hat{\Psi}$ can be obtained by inverting Equation 9.5. Since we use only a fraction of the total number of measurements, we reconstruct an approximation of the target state $\hat{\Psi}$, given by $\hat{\Psi}'$ using TVAL3 optimisation techniques [291]. This algorithm performs a minimisation of the following quantity

$$min_{\Psi'} \sum_{l} \|\nabla \Psi'_l\|_{\ell_1} + \frac{\mu}{2} \|\hat{A}\hat{\Phi} - \hat{\Psi}|^2_{\ell_2}. \tag{9.6}$$

and produces an approximate reconstruction of the input state. At pixel location x_l, the gradient of Ψ' is given by $\nabla \Psi'_l$. The regularisation term, μ can be optimised to account for our measurement conditions [291]. The solution of Equation 9.7 produces the approximate state $|\Psi'\rangle$ through CS.

Chapter 10

SPDC mode reconstruction

Single photons act as excellent carriers of information since they are intrinsically robust against noise and decoherence and can be transmitted over large distances without being affected by environmental conditions. Information can be encoded in various degrees of freedom of a photon, for e.g. spatial distribution, polarisation, frequency etc. and can be decoded using specific quantum decryption algorithms. In this work, we use raster scan and compressive sensing techniques to extract information that is present in its spatial and spectral degrees of freedom.

10.1. Spatial reconstruction of SPDC states

The spatial distribution of the SPDC optical modes can be mapped out by using the setup shown in Figure 10.1. The signal and idler photons exiting from the source is projected on to a digital micromirror device (DMD) prior to separation by the PBS. The DMD in-use is an array of discrete, individually controllable micromirrors, with a maximum device resolution of 1024×768 pixels. Each micromirror acts as a 'pixel' that can be turned on and off by switching between two tilted states. In our case, the "on" state corresponds to an arrangement where all the incoming light is reflected back into the optical path of the setup, while the "off" state directs light out of the setup. We used two methods - a) direct measurement technique and b) compressive sensing method to reconstruct the spatial modes of our light source.

In either of the methods, once the light is reflected from the DMD, it starts to disperse. In order to minimise the losses induced by the DMD, we inserted a folded 4-f imaging system that re-collimated the beam. The transmission efficiency of the 4-f system was roughly 10%. Both photons were then passed through a PBS, split based on their polarisation and then coupled into standard single mode telecom (SMF28) fibres which were then connected to SNSPDs.

Source of single photons

Heralded single photons were generated from a type II SPDC process in two types of sources:

I Source I: a periodically poled potassium titanyl phosphate (PPKTP) bulk crystal with a length of $L \approx 8\,\mathrm{mm}$ and a poling period of $\Lambda \approx 46\,\mu\mathrm{m}$.

II Source II: a periodically poled potassium titanyl phosphate (PPKTP) crystal consisting of Rubidium exchanged waveguides with a length of $L \approx 8$ mm and a poling period of $\Lambda \approx 46.1$ µm. [292].

The sources were designed to produce degenerate photons in the telecom regime ($\lambda_{s,i} \approx$ 1570 nm) at room temperature.

Basic setup

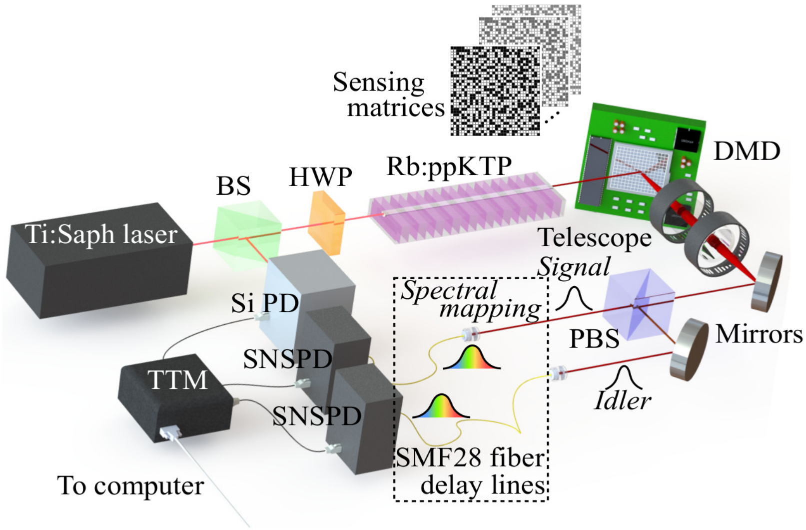

Figure 10.1.: Experimental setup for spatial reconstruction of SPDC photons. For spectral information along with the spatial properties, long fibres are introduced prior to the SNSPDs, to separate the photons based on their time-of-arrival.

The experimental setup for the generation and detection of single photons is displayed in Figure 10.1. It is similar to the setup shown in Figure 4.1 (a) except that all optical components in this arrangement were aligned in freespace. The source is pumped at half the degeneracy wavelength of the SPDC process (λ_{pump} =785 nm) using a Ti:Sapphire laser. The pump is mode-locked to produce picosecond pulses with a pulse width of approximately 2 ps. The repetition rate of the pulses is fixed to 3.64 MHz by using a pulse-picker to the 76 MHz pump source. A beam splitter (BS) is used in the optical line to separate out a few percent of the pump power and is detected by a silicon photodiode (Si PD), which was used as a trigger for the SPDC photon detection.

A half-wave plate (HWP) is used to manipulate the input polarisation to the photon pair source in order to ensure maximum efficiency. The light is coupled then into the source, which produces orthogonally polarised signal and idler photons that are split using a polarising beam splitter (PBS). Low jitter SNSPDs with a detection efficiency of 85% are used for the detection of the generated photons [109]. Both SNSPDs and the trigger photodiode (Si PD) is connected to a fast time-tagging module (TTM), Hydraharp, to record the counts in each arm. Source I is designed to show high heralding efficiencies,

$\eta_{s,i} > 80\%$ for the each of the SPDC photons, however, at the cost of low generation rates. On the other hand, Source II shows high brightness, but $\eta_{s,i}$ of only 20%.

10.1.1. Spatial mode reconstruction using the direct measurement technique

The most common method to map optical spatial modes is by using the direct measurement technique. This measurement technique uses a pixel-by-pixel scanning routine to measure the mode distributions of the incoming photons. Essentially this means, that during any instance of the measurement time only one pixel is "on" and all the others are turned "off" as shown in Figure 9.1. The light reflected from this single pixel is detected using our SNSPDs and recorded. Then the consecutive pixel is turned "on" and the rest are switched off, the reflected counts get recorded and the same process is repeated until all pixels are individually switched "on" and "off". Using the collected intensities, the spatial distributions of any source can be reconstructed. In SPDC-based sources such as ours, the raster-scan method can provide information on the spatial correlations between the photons [293].

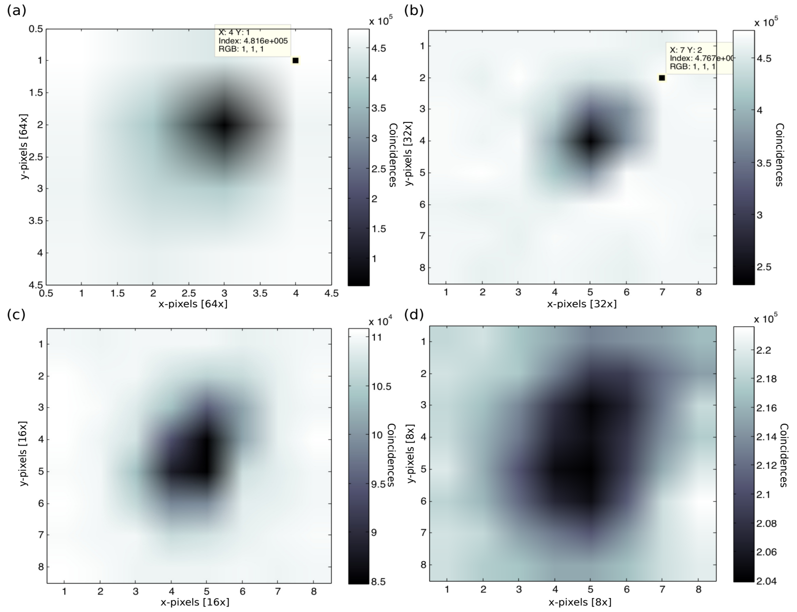

Figure 10.2.: Spatial reconstruction of the signal mode using (a) super-pixel size = 64 pixels and DMD area = 256 ×256 pixels, (b) super-pixel size = 32 pixels and DMD area = 256 ×256 pixels, (c) super-pixel size = 16 pixels and DMD area = 128 ×128 pixels and (d) super-pixel size = 8 pixels and DMD area = 64 ×64 pixels.

Due to the large DMD area and high integration times per pixel, the direct measurement technique can become extremely tedious and time consuming. In order to minimise the effort on these measurements, we scan the entire DMD area by turning on pixel clusters ("super-pixels"), *i.e.* more than one pixel, at a time and measuring the counts reflected by these mirrors. In our case, we choose super-pixel sizes consisting of 64, 32, 16 and 8 pixels. The measurement time in all cases was $t_{int} = 3\,\text{s}$.

The reconstruction of the signal and idler photons using the above-mentioned (standard) technique yielded poor reconstruction results due to high noise counts and hence we modified the pixel-by-pixel scan slightly. Instead of turning only one (super)pixel on and the others off, we used the opposite setting; meaning, we turned one (super)pixel off and the others on. The idea behind this setting was a speculation that in a noisy environment, it would be easier to see a dark (super)pixel amidst a surrounding of white pixels as opposed to the previous configuration.

The spatial mode reconstructions for Source I using this technique and the aforementioned super-pixel sizes are shown in Figure 10.2. On decreasing the super-pixel sizes, the measured DMD area was also decreased in order to compensate for the increasing measuring time and create a zoomed-in reconstruction of the photon spatial mode. By decreasing the super-pixel sizes further, *i.e.* ≤ 4, the image reconstruction began to show a poor contrast between the illuminated and dark regions of the DMD. To decrease the noise on the measured intensity profiles, the integration time was increased to $t_{int} \geq 16\,\text{s}$. Unfortunately, an improvement in the reconstructed image was not observed despite the long measurement times. This heavily limits the application of the raster-scan method as an effective tool to image SPDC modes and study correlations between the two photons.

10.1.2. Spatial mode reconstruction using compressive sensing

In this work, we use compressive sensing (CS) as an alternate method to characterise the spatial modes of SPDC photons. Similar to the raster-scan method, the SPDC modes are projected onto the DMD and the reflected intensity profiles are mapped onto the SNSPDs. However, unlike the raster-scan method which uses "on" and "off" pixels for mode reconstruction, in CS we use a series of random pixel patterns on the DMD.

The DMD is controlled as follows: Each pixel on the DMD can be turned "on" or "off", where the "on" state allows the light to propagate in to the optical setup, while the "off" state reflects light away. Sensing matrices, constructed by randomly turning each of these pixels "on" or "off", are used to probe the spatial features of the photons as shown in Figure 10.1. Each measurement gathers small pieces of information about the spatial distributions, and by solving Equation 9.7 through TVAL3 algorithm [291], we can estimate an approximation of the spatial mode profiles of the SPDC photons.

A series of sensing matrices are projected onto the DMD which interacts with the incoming light from the photon source. In each pattern, the ratio between the "on" and "off" pixels are always maintained to be 0.5. We pre-select the location of the spatial modes by maximising the counts on the SNSPDs. An area of $N = 64 \times 64 = 4096$ DMD pixels is chosen as the active area for each sensing matrix, of which $N/2 = 2048$ pixels are turned "on". Due to a large number of "on" pixels when compared to the raster-scan method, high photon counts are obtained on the detectors thereby requiring an integration time of only $t_{int} = 1\,\text{s}$ per pattern.

The number of sensing matrices can be varied dependent on the level of detail we wish to obtain from the measured signal. The maximum number of sensing matrices that can be used is given by the area of the sensing region, which is equal to the pixel-by-pixel raster-scan with a super-pixel size equal to one. The sampling ratio (SR) is defined as

$$SR = \frac{\text{number of projected sensing matrices}}{\text{active DMD area}} \text{ x } 100\ \% \tag{10.1}$$

Spatial mode reconstruction using CS: Source I

Firstly, we performed a spatial mapping of the signal and idler modes emitted from Source I (refer Section 10). The reconstructed spatial distributions with sampling ratios, $SR = 20$ %, 50 %, 100 % are shown in Figure 10.3. The average detected photon rate was about 6000 counts per second. A slight elongation was seen in the reconstructed beams due to aberrations from multiple optical components utilised for collimation along the propagation length of the SPDC modes.

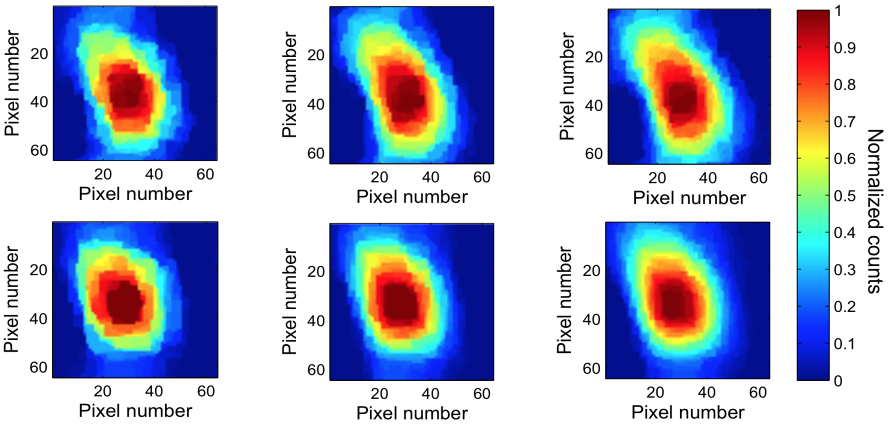

Figure 10.3.: Signal (top) and idler (bottom) spatial profiles of Source I with sampling ratios, $SR = 20$ %, 50 % and 100 % (left to right). The sensing matrix contains $N = 64 \times 64 = 4096$ elements.

Next, we determined the dimensionality of the reconstructed spatial modes of the generated SPDC states. We used the pixels on the DMD to discretise the spatial degree of freedom of SPDC photons. In this work, we estimated the spatial dimensionality by assessing only the illuminated region on the DMD rather than the entire surface of

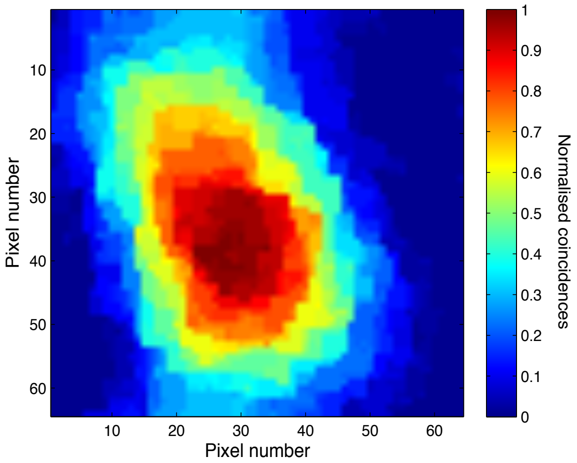

Figure 10.4.: Joint spatial distribution of the signal and idler modes of Source I in the pixel basis.

our measurement device given by the matrix $\hat{A}$. By using the $1/e^2$ diameter of the spatial mode of the quantum state, we determined the spatial dimensionality of each reconstructed mode [294]. Thus, the dimensionality of the signal (s) and idler (i) states were estimated to be $\mathcal{N}_s = 47 \times 60 = 2820$ and $\mathcal{N}_i = 45 \times 53 = 2385$ spatial bins respectively. The joint spatial distribution, which is a measure of photon correlations, of the signal and idler photons was reconstructed by mapping out the measured coincidences between the two. The reconstruction is shown in Figure 10.4. The dimensionality of the joint spatial probability distribution was estimated to be $\mathcal{N}_{JSD} = \mathcal{N}_s \times \mathcal{N}_i = 6.7 \times 10^6$.

From Figure 10.3, it was observed that the main features of the photon states were retrieved using just 20 % of the measurements and beyond this sampling ratio, only a slight improvement was seen in the reconstructed modes. However, in order to quantify the accuracy of the measurements, we estimated the fidelity of our reconstructions as a function of sampling ratio ($SR = 5$ %, 10 %, 15 %,..., 100 %.). The highest accuracy is

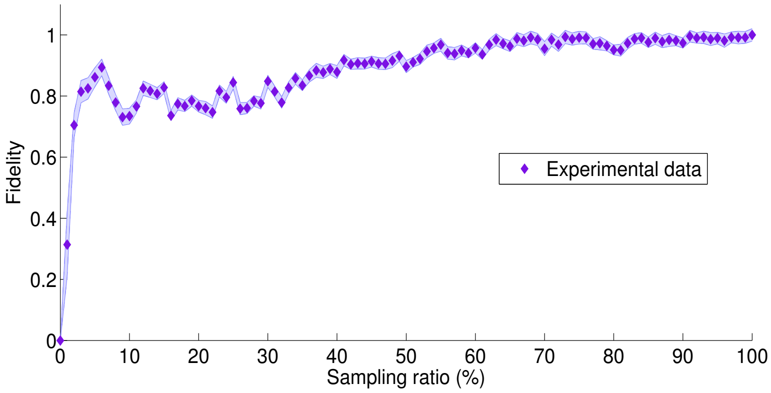

Figure 10.5.: The fidelity of the reconstructed state of Source I as a function of number of measurements.

observed in a full measurement scan that represents a sampling ratio of 100 %. Hence, $SR = 100$ % was taken as the target state (ψ_T). The accuracy of the spatial reconstruction was estimated by calculating the fidelity (see Figure 10.5) of the retrieved states (ψ_R) as a function of sampling ratio. This was defined as $\mathcal{F} = |\langle\psi_R|\psi_T\rangle|^2$. The error on the fidelity in Figure 10.5 was determined using Monte-Carlo simulations on a sample size of (100 signal x 100 idler) matrices, generated using a Poissonian error distribution on the detected signal and idler counts. Figure 10.5 clearly shows that on increasing the sampling ratios of the measurement, there is no significant improvement in the fidelity of the reconstructed state.

Spatial mode reconstruction using CS: Source II

Using the information obtained from the spatial mapping of Source I, we use a sampling ratio of $SR = 20$ % for the reconstruction of Source II (refer Section 10). Being a waveguide source, the photon generation rate is significantly higher when compared to the bulk source (Source I). The average number of accumulated counts per frame for the signal and idler mode is 545172 and 543326 respectively. The spatial reconstruction of the signal and idler photons of Source II is shown in Figure 10.6 (a), (b), and their joint spectral distribution is shown in Figure 10.6 (c). The measured signal-to-noise ratios are 27.1 and 18.5 for the signal and idler modes respectively. The time required for the reconstruction of each spatial profile was about 1 s.

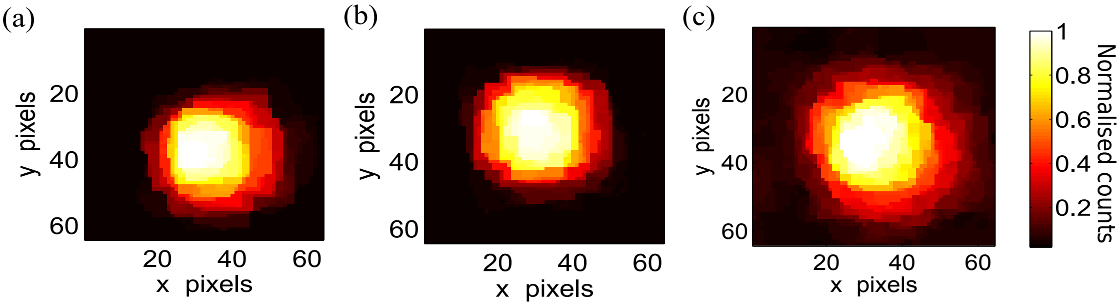

Figure 10.6.: Reconstructed spatial profiles of signal (a), idler (b) and the coincidences between them, also known as the joint spatial distribution, (c), using a sampling ratio, $SR = 20$ %. The sensing area consists a pixel array of $N = 64 \times 64 = 4096$ elements.

A slight displacement was observed in the reconstructed modes along the vertical axis. This arises from the imperfect polishing along the end-face of the waveguide. As a result, the signal and idler photons experience different effective refractive indices that causes a small spatial displacement between them (See Figure 10.6 (a), (b)).

The dimensionality of the signal (s) and idler (i) states of Source II were determined using the same technique as mentioned above. They were estimated to be $\mathcal{N}_s = 40 \times 40$ and $\mathcal{N}_i = 43 \times 43$ spatial bins respectively. The dimensionality of the joint spatial probability distribution was estimated to be $\mathcal{N}_{JSD} = \mathcal{N}_s \times \mathcal{N}_i = 2.96 \times 10^6$.

10.2. Spatio-spectral mode reconstruction of SPDC states

Apart from the spatial degree of freedom, the spectral properties of SPDC photons can also be exploited for data encoding. To access this information, the photons are separated on the basis of their wavelength using the same technique as Section 4.3. A fibre-based-time-of-flight spectrometer [182,183] consisting of long single mode (SMF28) fibres were incorporated into the setup, prior to detection, to characterise the spectral features of the source. SMF28 fibres have low losses, thereby resulting in a higher transmission medium for the measurement when compared to dispersive fibres mentioned in Section 4.3. After propagation, the time of arrival of each photon was accurately recorded with a fast time tagging module (Hydraharp) and high efficiency, low jitter SNSPDs. Using our measurement setup, large quantities of data stored in single photons can be decoded in the spatial and spectral degrees of freedom simultaneously [295–300].

Resolution of the time-of-flight spectrometer

The spectral resolution of the spectrometer is an important factor as it determines the dimensionality of the photon state that can be accessed by our measurement technique.

In this case, the spectral resolution depends on the dispersion introduced by the propagation medium (SMF28 fibres) and the detection jitter on the SNSPDs. The fibres have a dispersion of 17 ps nm^{-1} km^{-1}. The detection jitter was determined by injecting a source with a line-width bandwidth, and measuring the width of the time-of-flight curve. We tested eight SNSPDs and measured a detection jitter ranging from 100 ps to 150 ps. In order to obtain the best possible results from this technique, we chose two SNSPDs that showed the lowest jitter time and highest detection efficiency ($\eta_{det} \approx 80\%$). The detection jitter and spectral resolution of the measurement apparatus is listed in Table 10.1.

SOURCE	**SPDC photon**	**Fibres** Length (km)	Dispersion ($\frac{ps}{nm}$)	**SNSPD jitter** (ps)	**Resolution** (nm)
Source I	Signal	2.5	110	43	2.6
	Idler	5	140	85	1.6
Source II	Signal	10	120	170	0.7
	Idler	10	120	170	0.7

Table 10.1.: Detector jitter and spectral resolution of the measurement apparatus used for spatio-spectral reconstruction of SPDC states.

Spatial and spectral reconstruction of Source I

Firstly, we performed a spectral mapping of the signal and idler photons of Source I using a time-of-flight spectrometer shown in Figure 10.1. The fibre length, dispersion and detection jitter of the measurement is as shown in Table 10.1. Due to a higher jitter on the idler detector, the idler photon was transmitted through a longer fibre to compensate for the decreased spectral resolution but at the cost of increased losses. The transmission of the fibres used in the signal and idler arm were 90 % and 79 % respectively.

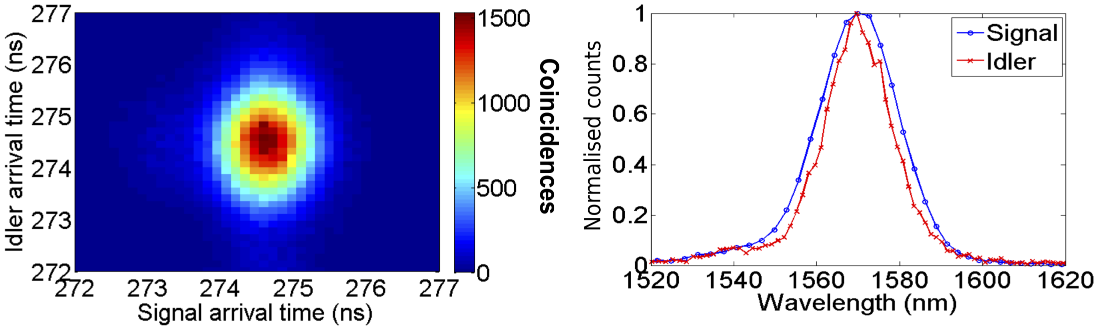

Figure 10.7.: Joint photon time-of-flight (left) and marginal spectra (right) of signal and idler.

The joint arrival time of the SPDC photons is shown in Figure 10.7 (left). The marginals were estimated by taking the transfer function of the arrival time of the down-converted photons (See Figure 10.7 (right)). The spectral $1/e^2$ bandwidth of the signal

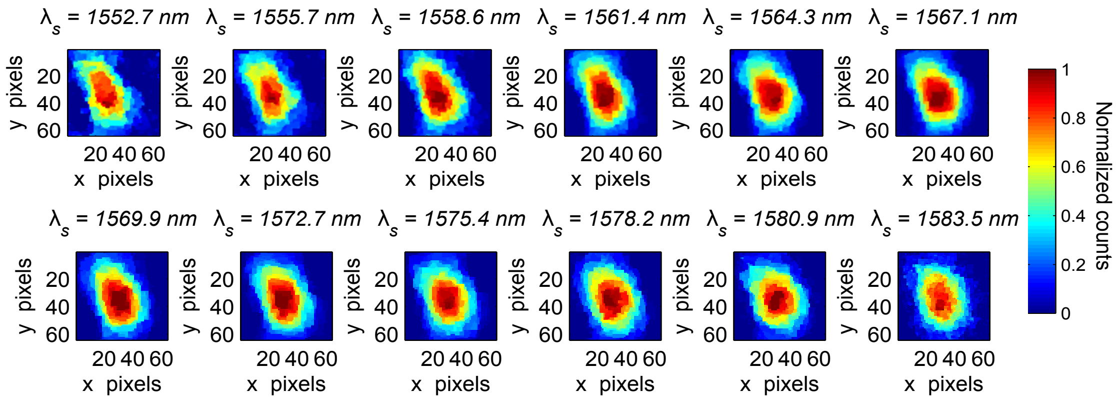

Figure 10.8.: Spatial reconstruction of the signal photons for each spectral bin using a sampling ratio of 45 % on a 64 × 64 pixel array. Number of successfully reconstructed spectral bins for the signal photons are $\mathcal{S}_s = 12$.

and idler photons measured were 40 nm and 32 nm respectively with their degeneracy point at twice the wavelength of the pump photons.

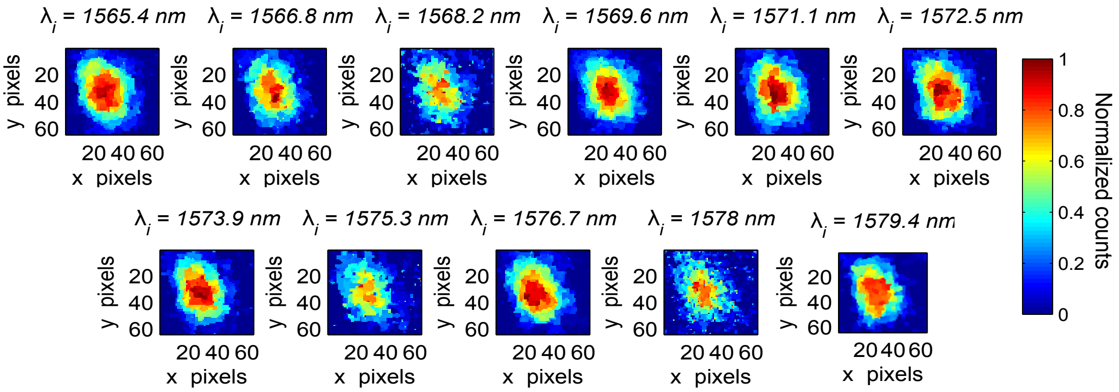

Figure 10.9.: Spatial reconstruction of the idler photons for each spectral bin using a sampling ratio of 45 % on a 64 × 64 pixel array. Number of successfully reconstructed spectral bins for the idler photons are $\mathcal{S}_i = 11$.

Next, the spatio-spectral features were reconstructed by resolving spatial profiles of the photon pairs with respect to their spectrum. Due to the low photon count rate of bulk sources, we used a sampling ratio of 45% for this measurement. Figure 10.8 - 10.9 shows the spatio-spectral features of our source on the same DMD area, $\mathcal{N} = 64 \times 64$ pixels. Due to losses introduced by the fibre delay lines and low external brightness of the bulk source, a higher integration time of $t = 15\,\mathrm{s}$ was used. The signal (s) and idler (i) fields delivered $\mathcal{S}_s = 12$ and $\mathcal{S}_i = 11$ successful spectrally-resolved spatial reconstructions respectively, where $\mathcal{S}$ is the number of spectral bins. The lower spectral dimensionality on the idler photon arises from the higher losses incurred from using longer fibres for spectral decomposition.

The dimensionality of the quantum state was estimated from the product of the spatial and the spectral bins given by $\mathcal{D}_s = \mathcal{N}_s \times \mathcal{S}_s = 33840$ for the signal photon and $\mathcal{D}_i =$

$\mathcal{N}_i \times \mathcal{S}_i = 26235$ for the idler photon.

Spatial and spectral reconstruction of Source II

The time-of-flight spectrometer specifications used to characterise Source II is shown in Table 10.1. The fibre transmission of the signal and idler arms were measured to be 63 % and 64 % respectively. The joint arrival time of the photons are shown in Figure 10.10 (a) and the estimated marginal spectrum is plotted in Figure 10.10 (b). The primary phasematching peak was at 1570 nm showing a spectral $1/e^2$ bandwidth of 26 nm and 43 nm for the measured signal and idler photons respectively. The spectral peaks at shorter wavelengths arises from a slightly multi-mode pump spectrum which can be easily filtered out by the use of bandpass filters in the setup or post-processing on the collected data.

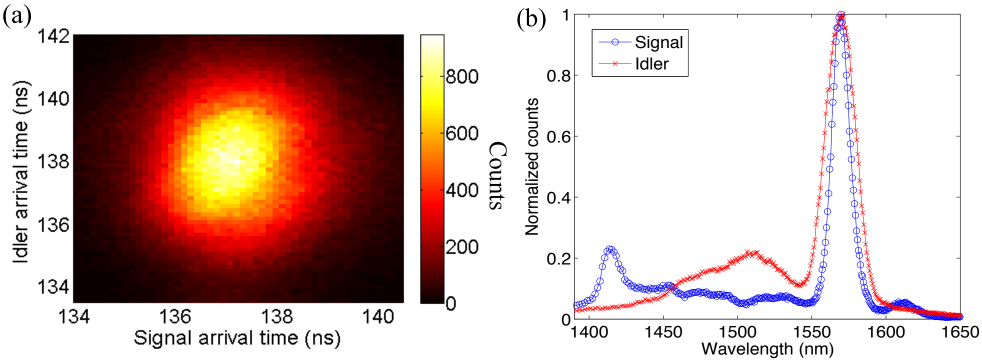

Figure 10.10.: (a) Joint photon arrival time and (b) full marginal spectra of signal and idler photons.

The spatio-spectral reconstruction of Source II was performed using a sampling ratio of 20 %. First, we characterised the noise peaks at lower wavelengths, $\lambda_s \approx 1414$ nm and $\lambda_i \approx 1515$ nm. Due to higher mode excitations of the pump field within the waveguide, parasitic SPDC processes can be triggered [301]. We speculate that the sharp peak at $\lambda_s =$1414 nm is generated due to this and can be easily suppressed by using broadband spectral filters or by post-processing. On the other hand, we conclude that the broader peak at $\lambda_i =$1515 nm is caused by optical Cherenkov radiation that is phase-matched in our waveguide [302]. This arises when short pump pulses induce a nonlinear polarisation in an electro-optic medium (here, PPKTP waveguide) that radiates in a Cherenkov-like cone along the propagation direction of the pump pulse [303]. We study these parasitic modes by performing spatial reconstructions of the signal and idler mode within this wavelength range. Figure 10.11 (b) and (c) shows the outcome of these reconstructions at $\lambda_s \approx 1414$ nm and $\lambda_i \approx 1515$ nm, and at an intermediate wavelength to demonstrate the trend in the signal and idler profiles.

A slight distortion in the reconstructed modes shown in Figure 10.11 (b) and (c) is attributed to lateral chromatic aberration [304] induced by the collimation lens used in our experiment. Due to the large spectral range used in our investigation, the size of the spatial modes increases due to varying refractive indices experienced by different

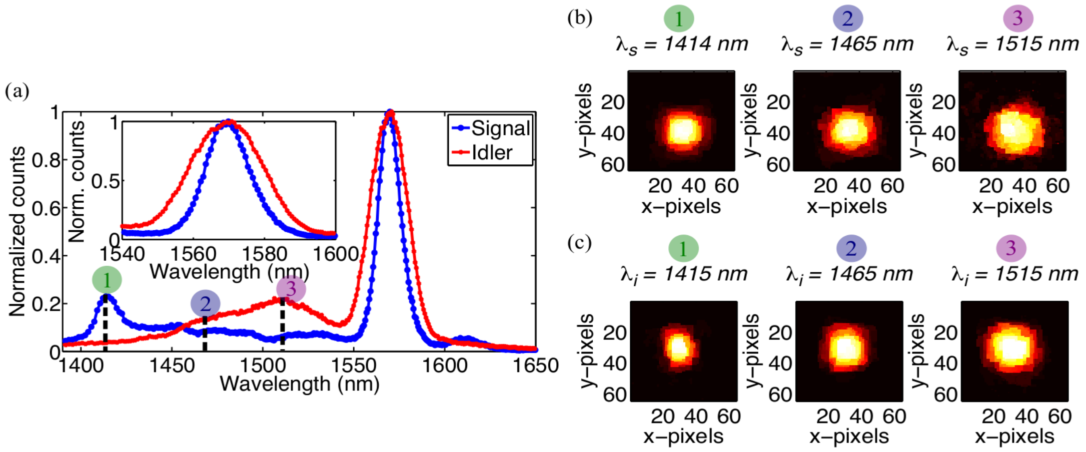

Figure 10.11.: (a) Full marginal spectra of signal and idler photons with phase matching peak at 1570 nm, (inset) shows a zoomed depiction of the phasematched peak; noise peaks are marked at $\lambda_s \approx 1414$ nm and $\lambda_i \approx 1515$ nm and an intermediate wavelength at $\lambda_{s,i} \approx 1465$ nm and the reconstructed spatial profiles for signal (b) and idler (c) photons at the chosen wavelengths.

wavelength components in the marginal spectrum. This can be corrected by the use of digital filters during post-processing as demonstrated in Reference [305].

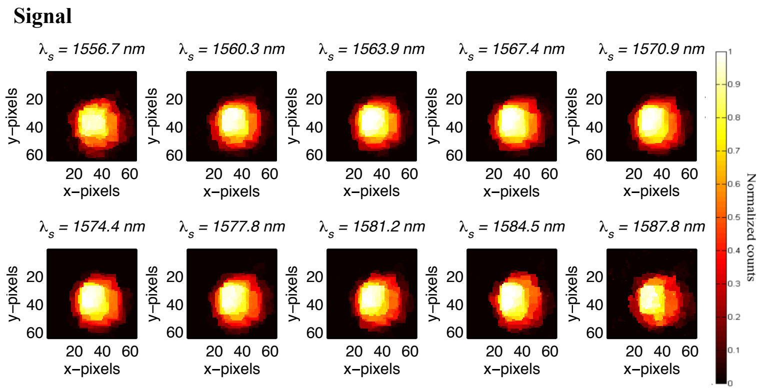

Figure 10.12.: Spatial reconstruction of the signal photons for a few spectral bins using a sampling ratio of 20 % on a 64 × 64 pixel array. Number of successfully reconstructed spectral bins are $\mathcal{S}_s = 60$, of which ten spatial profiles each are reconstructed at an interval of $\delta\lambda = (3.4 \pm 0.2)$ nm.

In the next step, we looked more closely at the primary phasematching peak of the source. The measurement setup had the ability to spectrally resolve changes of the order of $\delta\lambda \approx 0.7$ nm (see Table 10.1), which was also experimentally verified from the wavelength difference between two consecutive spectral bins plotted in Figure 10.11 (a). This allows us to define high-dimensional states for the signal and idler photons with a dimension of $\mathcal{S}_s = 54$ and $\mathcal{S}_i = 60$ respectively. In Figure 10.12 - 10.13 we show a few reconstructions within the primary peak of the photon pairs performed with a sampling ratio equal to 20 %. The dimensionality ($\mathcal{D}$) of the measured quantum state in the spatio-

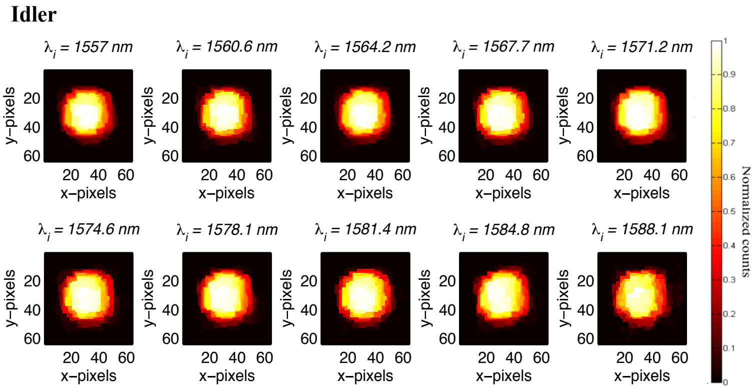

Figure 10.13.: Spatial reconstruction of the idler photons for a few spectral bins using a sampling ratio of 20 % on a 64 × 64 pixel array. Number of successfully reconstructed spectral bins are $\mathcal{S}_i = 54$, of which ten spatial profiles each are reconstructed at an interval of $\delta\lambda = (3.4 \pm 0.2)$ nm.

spectral domain was estimated to be $\mathcal{D}_{s/i} = \mathcal{N}_{s/i} \times \mathcal{S}_{s/i}$. In this way, the spatio-spectral dimensionality of the signal and idler photons were determined to be $\mathcal{D}_s = 40 \times 40 \times 54$ and $\mathcal{D}_i = 43 \times 43 \times 60$ respectively. Hence, the joint spatio-spectral distribution (JSSD) of the reconstructed states was estimated to be $\mathcal{D}_{JSSD} = \mathcal{D}_s \times \mathcal{D}_i = 11.98 \times 10^9$ dimensions.

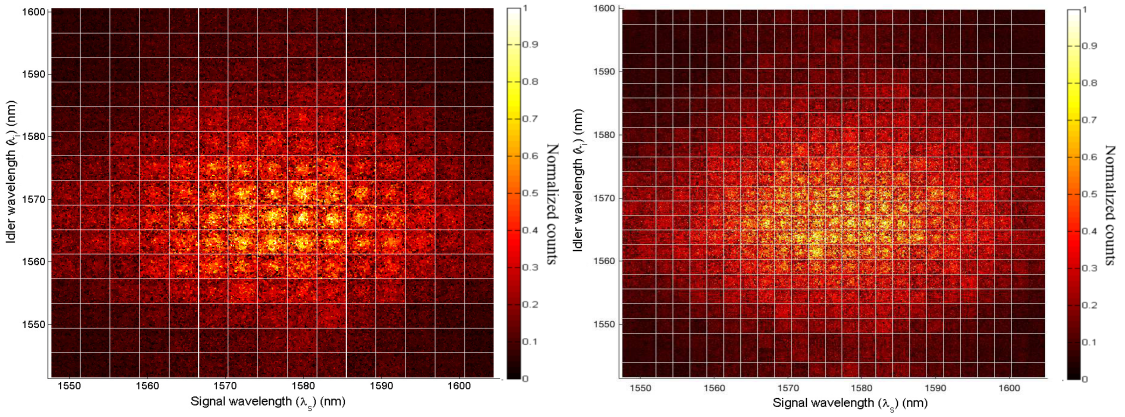

Figure 10.14.: The reconstruction of the joint spatio-spectral intensity distributions are plotted using a sampling ratio of 20 % on a 64 × 64 pixel array. Each frame shows a spatial reconstruction that is integrated from data obtained from 15 (left) and 25 (right) spectral bins.

Joint spectral intensity distributions are shown in Figure 10.14. This reconstruction was performed by measuring the coincidences between the signal and idler photons and plotting them against their spectral range obtained from the time-of-flight spectrometers. As opposed to Figure 10.7, here we reconstruct spatial profiles by resolving the entire phasematching spectrum in to 15 bins (See Figure 10.14 (left)). Each frame is a spatial reconstruction of the total measured coincidences within each spectral bin in a 64 × 64 pixel array. In order to obtain sufficient number of coincidences, each pattern on the sensing matrix was exposed to the photon beams for 4 s. Using the same measurement data, we also spatially reconstructed a 25×25 spectral array on a 64×64 sensing array in Figure 10.14 (right). Despite a lowered coincidence rate per spectral bin, a clear trend in the joint spectral intensity distribution can be observed.

Chapter 11

Conclusion

Complex states of light offer the possibility of encoding and processing many bits of information in a single photon. However, extraction of information from these encoded states are quite challenging due to technological limitations of quantum protocols. In this work, we utilise two reconstruction techniques to demonstrate the characterisation of the spatial and spectral properties of quantum correlated photon pairs produced through a SPDC process.

The reconstruction process involves the use of a DMD to project the spatial profile of the object, here, SPDC source. For the spectral discretisation, we use a time-of-flight spectrometer. Photons generated from PPKTP sources were initially reconstructed using conventional means of image reconstruction, *i.e.* raster-scan technique. This method collects information by switching on a single pixel at a time and integrating over the entire area. The outcomes were extremely noisy; and despite the drastic increment in integration times, the reconstruction results were poor. This limitation reduces the applicability of this method in quantum and low-light applications.

Then, we utilise CS to demonstrate a proof-of-principle characterisation of quantum correlated photon pairs. This technique extracts chunks of information by projecting random sensing matrices on the DMD. The integration time and the number of measurements required for successful reconstructions were significantly lower than the Nyquist limit. We were able to generate spatial mode reconstructions with an accuracy of $\geq 75\%$ with just 20 % measurements. The spatial mode dimensionality of signal and idler photons were estimated from the $1/e^2$ diameter from the reconstructions. The signal and idler had a dimensionality of 47×60 pixels and 45×53 pixels for the bulk PPKTP source; and the waveguide source showed a dimensionality of 40×40 pixels and 43×43 pixels respectively. The joint spatial probability distribution of both photons consisted of nearly seven- and three- million dimensions for the bulk and waveguided source. The spectral features were measured using long single-mode fibres that had a resolution of 0.7 nm. The properties of the main phasematching peak as well as the parasitic peaks were reconstructed and studied. The bulk source showed a joint spatio-spectral dimensionality of 0.89 billion, more than one order of magnitude lower than that of the waveguide source, due to significantly lesser brightness in terms of photon generation.

Despite the complexity of the photonic state, CS was able to reconstruct states with billions of dimensions with just a fraction of the acquisition time and sampling rate required by conventional means. The dramatic reduction in the time required to characterise SPDC sources makes our technique a powerful diagnosis tool for complex quantum photonic states.

Acknowledgements

I would like to take this opportunity to thank Christine Silberhorn for taking me under her wing and introducing me to a new area of science (with respect to my previous background). Over the four years of my Ph.D, I learned a lot and achieved a rather intriguing profile involving technological and experimental exposure in the field of quantum optics. Being part of her group gave me a platform to network with an exceptional group of scientists and I am immensely grateful for the motivation she has provided me throughout my stay in Paderborn. She opened out new doors for me by providing me with the support to visit IdQuantique and NIST, and also, when I wished to commercialise our quantum source.

I want to thank Harald Herrmann for educating me on device building strategies and the characterisation techniques involved. He has supported me during my entire Ph.D and was always available to lend a helping hand and provide constructive feedback. I regard him as one of the most valuable mentors of my life. I would also like to thank Linda Sansoni who spent hours with me discussing various quantum-related topics and assisting me in the lab. Her presence was dearly missed during the final years of my Ph.D. I thank Evan Meyer-Scott for helping me with the theoretical estimations of my project and providing me with a deeper insight into the fundamental issues faced by quantum sources.

I wish to ardently thank Rita Prevor for the enormous support she provided me with all sorts of complicated documentation and administration work. She played a huge role in making my Ph.D days (and even after I left) run smoothly. I also thank Kerstin Falke and Irmgard Zimmermann for their help.

I would like to acknowledge Raimund Ricken for teaching me various clean-room techniques and providing me with samples whenever I needed them. He exercised a tremendous amount of patience during my training days and was ready to assist me whenever I needed help. I also want to thank Viktor Quiring and Christof Eigner for optimising the coating machines and providing me with exceptional samples, without which, all of my experiments would have suffered dramatically. Let me take this opportunity to also thank Sebastian Lengeling and Florian for an enjoyable time in the clean room.

I had several office mates over the years, but I can not write this acknowledgement without mentioning Stephan Krapick who was like a big brother to me. As soon as I reached Paderborn, he helped me with the relocation to my new apartment, all the bureaucratic work and also with lab work. He was an enjoyable companion to have in the office and he never failed to elevate my mood when I was feeling blue. I would also like to thank my other office mates, Melanie Engelkemeier and Georg Harder for the fun discussions we had during our brief time together.

I want to show my appreciation to Thomas Gerrits and Omar Magana-Loaiza for my experience at NIST. I had a wonderful two months with them. I also want to thank Tim Bartley for assisting me with writing up the paper with NIST and giving me helpful

suggestions on how to make it more appealing. I wish to thank Daniel Stucki and Giusseppi Scalia for a great experience at IDQuantique.

Next, I would like to thank the rest of the IQO team and alumni. Hubertus Suche, Benjamin Brecht, Helge Rütz, Michael Stefszky, Thomas Nitsche, Regina Kruse, Kai Hong Luo, Marcello Massaro, Felix vom Bruch, Vahid Ansari, Matteo Santandrea, Johannes Tiedau, Sonja Barkhofen, Laura Padberg, Markus Allgaier, Fabian Elster, Sebastian Brauner, Jano Gil López and Lennart Lorz. Please forgive me if I have failed to mention someone's name, the group is rather big. So once again, thank you to all the names I have and have not mentioned.

Lastly, I would like to thank my family and friends. My mother who was always there to support me unconditionally and my sister, Samantha, who gave me professional advice and kept in touch with me everyday, despite the distance between us. I want to thank my best friend in the whole world, Manoj Kumar, for being part of my life for over 10 years. I also wish to thank my close friend, Anupam Yadav, for being there whenever I needed him.

Thank you!

Major author contributions

- **Nicola Montaut**, Linda Sansoni, Evan Meyer-Scott, Raimund Ricken, Viktor Quiring, Harald Herrmann, and Christine Silberhorn, "*High-efficiency Plug-and-Play Source of Heralded Single Photons*", Phys. Rev. Applied 8, 024021.
- Evan Meyer-Scott, **Nicola Montaut**, Johannes Tiedau, Linda Sansoni, Harald Herrmann, Tim J. Bartley, and Christine Silberhorn, "*Limits on the heralding efficiencies and spectral purities of spectrally filtered single photons from photon-pair sources*", Phys. Rev. A 95, 061803(R).
- **Nicola Montaut**, Omar S. Magana-Loaiza, Tim J. Bartley, Varun B. Verma, Sae Woo Nam, Richard P. Mirin, Christine Silberhorn, and Thomas Gerrits, "*Simultaneous characterization of telecom photon pairs in the spatial and spectral degrees of freedom using compressive sensing*", Optica 5 (11), 1418-1423.
- Marcello Massaro, Evan Meyer-Scott, **Nicola Montaut**, Harald Herrmann, Christine Silberhorn, "*Improving SPDC single-photon sources via extended heralding and feed-forward control*", New Journal of Physics 21 (5), 053038.
- Philip Georgi, Marcello Massaro, Kai-Hong Luo, Basudeb Sain, **Nicola Montaut**, Harald Herrmann, Thomas Weiss, Guixin Li, Christine Silberhorn, Thomas Zentgraf, "*Metasurface interferometry towards quantum sensors*", Nature, Light: Science & Applications 8 (1), 1-7.

Bibliography

[1] Dirk Bouwmeester and Anton Zeilinger. The physics of quantum information: basic concepts. In *The physics of quantum information*, pages 1–14. Springer, 2000.

[2] Jonathan P Dowling and Gerard J Milburn. Quantum technology: the second quantum revolution. *Philosophical Transactions of the Royal Society of London. Series A: Mathematical, Physical and Engineering Sciences*, 361(1809):1655–1674, 2003.

[3] Peter W Shor. Algorithms for quantum computation: Discrete logarithms and factoring. In *Proceedings 35th annual symposium on foundations of computer science*, pages 124–134. Ieee, 1994.

[4] C. H. Bennett and G. Brassard. Quantum cryptography: Public key distribution and coin tossing. In *Proceedings of IEEE International Conference on Computers, Systems and Signal Processing*, pages 175 – 179. IEEE, 1984.

[5] Nicolas Gisin, Grégoire Ribordy, Wolfgang Tittel, and Hugo Zbinden. Quantum cryptography. *Rev. Mod. Phys.*, 74:145–195, Mar 2002.

[6] Richard P Feynman. Simulating physics with computers. *International journal of theoretical physics*, 21(6):467–488, 1982.

[7] JG Rarity, PCM Owens, and PR Tapster. Quantum random-number generation and key sharing. *Journal of Modern Optics*, 41(12):2435–2444, 1994.

[8] I. L. Chuang and M. A. Nielsen. *Quantum Information and Quantum Computation.* Cambridge University Press, Cambridge, 2000.

[9] Emanuel Knill, Raymond Laflamme, and Gerald J Milburn. A scheme for efficient quantum computation with linear optics. *nature*, 409(6816):46, 2001.

[10] Matthew D Eisaman, Jingyun Fan, Alan Migdall, and Sergey V Polyakov. Invited review article: Single-photon sources and detectors. *Review of scientific instruments*, 82(7):071101, 2011.

[11] Christopher J Chunnilall, Ivo Pietro Degiovanni, Stefan Kück, Ingmar Müller, and Alastair G Sinclair. Metrology of single-photon sources and detectors: a review. *Optical Engineering*, 53(8):081910, 2014.

[12] Frank Diedrich and Herbert Walther. Nonclassical radiation of a single stored ion. *Physical review letters*, 58(3):203, 1987.

[13] Vittorio Giovannetti, Seth Lloyd, and Lorenzo Maccone. Quantum-enhanced measurements: beating the standard quantum limit. *Science*, 306(5700):1330–1336, 2004.

[14] Jeremy L O'brien. Optical quantum computing. *Science*, 318(5856):1567–1570, 2007.

[15] Stefan Strauf. Quantum optics: Towards efficient quantum sources. *Nature Photonics*, 4(3):132, 2010.

[16] Artur K Ekert. Quantum cryptography based on bell's theorem. *Physical review letters*, 67(6):661, 1991.

[17] Charles H Bennett, François Bessette, Gilles Brassard, Louis Salvail, and John Smolin. Experimental quantum cryptography. *Journal of cryptology*, 5(1):3–28, 1992.

[18] Fulvio Flamini, Nicolò Spagnolo, and Fabio Sciarrino. Photonic quantum information processing: a review. *Reports on Progress in Physics*, 82(1):016001, 2018.

[19] Matthew Pelton, Charles Santori, Jelena Vucković, Bingyang Zhang, Glenn S Solomon, Jocelyn Plant, and Yoshihisa Yamamoto. Efficient source of single photons: a single quantum dot in a micropost microcavity. *Physical review letters*, 89(23):233602, 2002.

[20] Stefan Strauf, Nick G Stoltz, Matthew T Rakher, Larry A Coldren, Pierre M Petroff, and Dirk Bouwmeester. High-frequency single-photon source with polarization control. *Nature photonics*, 1(12):704, 2007.

[21] Dan Dalacu, Khaled Mnaymneh, Vera Sazonova, Philip J Poole, Geof C Aers, Jean Lapointe, Ross Cheriton, Anthony J SpringThorpe, and Robin Williams. Deterministic emitter-cavity coupling using a single-site controlled quantum dot. *Physical Review B*, 82(3):033301, 2010.

[22] KG Lee, XW Chen, Hadi Eghlidi, P Kukura, R Lettow, A Renn, Vahid Sandoghdar, and Stephan Götzinger. A planar dielectric antenna for directional single-photon emission and near-unity collection efficiency. *Nature Photonics*, 5(3):166, 2011.

[23] Brahim Lounis and Michel Orrit. Single-photon sources. *Reports on Progress in Physics*, 68(5):1129, 2005.

[24] P Michler, A Kiraz, C Becher, WV Schoenfeld, PM Petroff, Lidong Zhang, E Hu, and A Imamoglu. A quantum dot single-photon turnstile device. *science*, 290(5500):2282–2285, 2000.

[25] Julien Claudon, Joël Bleuse, Nitin Singh Malik, Maela Bazin, Périne Jaffrennou, Niels Gregersen, Christophe Sauvan, Philippe Lalanne, and Jean-Michel Gérard. A highly efficient single-photon source based on a quantum dot in a photonic nanowire. *Nature Photonics*, 4(3):174, 2010.

[26] T Heindel, C Schneider, M Lermer, SH Kwon, T Braun, S Reitzenstein, S Höfling, M Kamp, and A Forchel. Electrically driven quantum dot-micropillar single photon source with 34% overall efficiency. *Applied Physics Letters*, 96(1):011107, 2010.

[27] Dieter Bimberg, Marius Grundmann, and Nikolai N Ledentsov. *Quantum dot heterostructures*. John Wiley & Sons, 1999.

[28] Christian Kurtsiefer, Sonja Mayer, Patrick Zarda, and Harald Weinfurter. Stable solid-state source of single photons. *Physical review letters*, 85(2):290, 2000.

[29] I Aharonovich, S Castelletto, DA Simpson, CH Su, AD Greentree, and S Prawer. Diamond-based single-photon emitters. *Reports on progress in Physics*, 74(7):076501, 2011.

[30] S Castelletto, BC Johnson, Viktor Ivády, N Stavrias, T Umeda, A Gali, and T Ohshima. A silicon carbide room-temperature single-photon source. *Nature materials*, 13(2):151, 2014.

[31] Thomas M Babinec, Birgit JM Hausmann, Mughees Khan, Yinan Zhang, Jeronimo R Maze, Philip R Hemmer, and Marko Lončar. A diamond nanowire single-photon source. *Nature nanotechnology*, 5(3):195, 2010.

[32] Niels Gregersen, Torben Roland Nielsen, Jesper Mørk, Julien Claudon, and Jean-Michel Gérard. Designs for high-efficiency electrically pumped photonic nanowire single-photon sources. *Optics express*, 18(20):21204–21218, 2010.

[33] David C Burnham and Donald L Weinberg. Observation of simultaneity in parametric production of optical photon pairs. *Physical Review Letters*, 25(2):84, 1970.

[34] Artur K Ekert, John G Rarity, Paul R Tapster, and G Massimo Palma. Practical quantum cryptography based on two-photon interferometry. *Physical Review Letters*, 69(9):1293, 1992.

[35] AV Sergienko, M Atatüre, Z Walton, G Jaeger, BEA Saleh, and MC Teich. Quantum cryptography using femtosecond-pulsed parametric down-conversion. *Physical Review A*, 60(4):R2622, 1999.

[36] Thomas Jennewein, Christoph Simon, Gregor Weihs, Harald Weinfurter, and Anton Zeilinger. Quantum cryptography with entangled photons. *Physical Review Letters*, 84(20):4729, 2000.

[37] Alfred B U'Ren, Christine Silberhorn, Konrad Banaszek, and Ian A Walmsley. Efficient conditional preparation of high-fidelity single photon states for fiber-optic quantum networks. *Phys. Rev. Lett.*, 93(9):093601, 2004.

[38] Edo Waks, Eleni Diamanti, and Yoshihisa Yamamoto. Generation of photon number states. *New Journal of Physics*, 8:4–4, jan 2006.

[39] Alexandre Soujaeff, Shigeki Takeuchi, KEIJI Sasaki, Toshio Hasegawa, and Mitsuru Matsui. Heralded single photon source at 1550 nm from pulsed parametric down conversion. *J. Mod. Opt*, 54(2-3):467–471, 2007.

[40] Jingyun Fan and Alan Migdall. A broadband high spectral brightness fiber-based two-photon source. *Optics express*, 15(6):2915–2920, 2007.

[41] E. A. Goldschmidt, M. D. Eisaman, J. Fan, S. V. Polyakov, and A. Migdall. Spectrally bright and broad fiber-based heralded single-photon source. *Phys. Rev. A*, 78:013844, Jul 2008.

[42] WH Louisell, A Yariv, and AE Siegman. Quantum fluctuations and noise in parametric processes. i. *Physical Review*, 124(6):1646, 1961.

[43] B Ya Zel'dovichand DN Klyshko. Field statistics in parametric luminescence. *JETP Lett*, 9(1):40–43, 1969.

[44] Sven Ramelow, Alessandro Farsi, Stéphane Clemmen, Kevin Luke, Michal Lipson, and Alexander L Gaeta. Monolithic source of tunable narrowband photons for future quantum networks. In *2015 Conference on Lasers and Electro-Optics (CLEO)*, pages 1–2. Ieee, 2015.

[45] Xiang Guo, Chang-ling Zou, Carsten Schuck, Hojoong Jung, Risheng Cheng, and Hong X Tang. Parametric down-conversion photon-pair source on a nanophotonic chip. *Light: Science & Applications*, 6(5):e16249, 2017.

[46] Fabien Boitier, Adeline Orieux, Claire Autebert, Aristide Lemaître, Elisabeth Galopin, Christophe Manquest, Carlo Sirtori, Ivan Favero, Giuseppe Leo, and Sara Ducci. Electrically injected photon-pair source at room temperature. *Physical review letters*, 112(18):183901, 2014.

[47] Claire Autebert, Natalia Bruno, Anthony Martin, Aristide Lemaitre, Carmen Gomez Carbonell, Ivan Favero, Giuseppe Leo, Hugo Zbinden, and Sara Ducci. Integrated algaas source of highly indistinguishable and energy-time entangled photons. *Optica*, 3(2):143–146, 2016.

[48] Marius A Albota and Eric Dauler. Single photon detection of degenerate photon pairs at 1.55 μm from a periodically poled lithium niobate parametric downconverter. *journal of modern optics*, 51(9-10):1417–1432, 2004.

[49] Daniel Ljunggren and Maria Tengner. Optimal focusing for maximal collection of entangled narrow-band photon pairs into single-mode fibers. *Physical Review A*, 72(6):062301, 2005.

[50] Stefania Castelletto, Ivo P Degiovanni, V Schettini, and A Migdall. Optimizing single-photon-source heralding efficiency and detection efficiency metrology at 1550 nm using periodically poled lithium niobate. *Metrologia*, 43(2):S56, 2006.

[51] Matthew Pelton, Philip Marsden, Daniel Ljunggren, Maria Tengner, Anders Karlsson, Anna Fragemann, Carlota Canalias, and Fredrik Laurell. Bright, single-spatial-mode source of frequency non-degenerate, polarization-entangled photon pairs using periodically poled ktp. *Optics Express*, 12(15):3573–3580, 2004.

[52] Marco Fiorentino, Gaétan Messin, Christopher E Kuklewicz, Franco NC Wong, and Jeffrey H Shapiro. Generation of ultrabright tunable polarization entanglement without spatial, spectral, or temporal constraints. *Physical Review A*, 69(4):041801, 2004.

[53] Kaoru Sanaka, Karin Kawahara, and Takahiro Kuga. New high-efficiency source of photon pairs for engineering quantum entanglement. *Physical Review Letters*, 86(24):5620, 2001.

[54] E. A. J. Marcatili. Dielectric rectangular waveguide and directional coupler for integrated optics. *The Bell System Technical Journal*, 48(7):2071–2102, Sep. 1969.

[55] Linda Sansoni, Kai Hong Luo, Christof Eigner, Raimund Ricken, Viktor Quiring, Harald Herrmann, and Christine Silberhorn. A two-channel, spectrally degenerate polarization entangled source on chip. *npj Quantum Inf.*, 3(1):5, 2017.

[56] Hung-Pin Chung, Chieh-Hsun Lee, Kuang-Hsu Huang, Sung-Lin Yang, Kai Wang, Alexander S Solntsev, Andrey A Sukhorukov, Frank Setzpfandt, and Yen-Hung Chen. Broadband on-chip polarization mode splitters in lithium niobate integrated adiabatic couplers. *Optics express*, 27(2):1632–1645, 2019.

[57] Tian Zhong, Franco N. C. Wong, Tony D. Roberts, and Philip Battle. High performance photon-pair source based on a fiber-coupled periodically poled ktiopo4 waveguide. *Opt. Express*, 17(14):12019–12030, Jul 2009.

[58] Lee Oesterling, Fernando Monteiro, Sean Krupa, David Nippa, Richard Wolterman, Donald Hayford, Eric Stinaff, Bruno Sanguinetti, Hugo Zbinden, and Rob Thew. Development of photon pair sources using periodically poled lithium niobate waveguide technology and fiber optic components. *J. Mod. Opt*, 62(20):1722–1731, 2015.

[59] Lutfi Arif Ngah, Olivier Alibart, Laurent Labonté, Virginia D'Auria, and Sébastien Tanzilli. Ultra-fast heralded single photon source based on telecom technology. *Laser Photon. Rev.*, 9(2):L1–L5, 2015.

[60] Nicola Montaut, Linda Sansoni, Evan Meyer-Scott, Raimund Ricken, Viktor Quiring, Harald Herrmann, and Christine Silberhorn. High-efficiency plug-and-play source of heralded single photons. *Physical Review Applied*, 8(2):024021, 2017.

[61] O. Alibart, D. B. Ostrowsky, P. Baldi, and S. Tanzilli. High-performance guided-wave asynchronous heralded single-photon source. *Opt. Lett.*, 30(12):1539–1541, Jun 2005.

[62] A Zavriyev, A Leverrier, V Denchev, and A Trifonov. Improving the performance of quantum key distribution apparatus. *Journal of Modern Optics*, 54(2-3):305–313, 2007.

[63] ML Bortz. *Quasi-Phase Matched Optical Frequency Conversion in Lithium Niobate Waveguides.* PhD thesis, 1994.

[64] Robert W Boyd. *Nonlinear optics.* Elsevier, 2003.

[65] GJ Edwards and M Lawrence. A temperature-dependent dispersion equation for congruently grown lithium niobate. *Optical and quantum electronics*, 16(4):373–375, 1984.

[66] Dieter H Jundt. Temperature-dependent sellmeier equation for the index of refraction, n e, in congruent lithium niobate. *Optics letters*, 22(20):1553–1555, 1997.

[67] G Nataf. *New approaches to understand conductive and polar domain walls by Raman spectroscopy and low energy electron microscopy.* PhD thesis, 10 2016.

[68] Makoto Minakata, Shoichi Saito, Masashi Shibata, and Shintaro Miyazawa. Precise determination of refractive-index changes in ti-diffused linbo3 optical waveguides. *Journal of Applied Physics*, 49(9):4677–4682, 1978.

[69] WK Burns, PH Klein, EJ West, and LE Plew. Ti diffusion in ti: Linbo3 planar and channel optical waveguides. *Journal of Applied Physics*, 50(10):6175–6182, 1979.

[70] RL Holman, PJ Cressman, and JA Anderson. Processing and properties of diffused lithium niobate planar optical waveguides. *Ferroelectrics*, 27(1):77–80, 1980.

[71] AM Glass, Ivan P Kaminow, Albert A Ballman, and DH Olson. Absorption loss and photorefractive-index changes in ti: Linbo 3 crystals and waveguides. *Applied optics*, 19(2):276–281, 1980.

[72] H Hu, R Ricken, and W Sohler. Low-loss ridge waveguides on lithium niobate fabricated by local diffusion doping with titanium. *Applied Physics B*, 98(4):677–679, 2010.

[73] DA Bryan, Robert Gerson, and HE Tomaschke. Increased optical damage resistance in lithium niobate. *Applied Physics Letters*, 44(9):847–849, 1984.

[74] KL Sweeney, LE Halliburton, DA Bryan, RR Rice, Robert Gerson, and HE Tomaschke. Point defects in mg-doped lithium niobate. *Journal of applied physics*, 57(4):1036–1044, 1985.

[75] DA Bryan, RR Rice, Robert Gerson, HE Tomaschke, KL Sweeney, and LE Halliburton. Magnesium-doped lithium niobate for higher optical power applications. *Optical Engineering*, 24(1):241138, 1985.

[76] U Schlarb and K Betzler. Influence of the defect structure on the refractive indices of undoped and mg-doped lithium niobate. *Physical Review B*, 50(2):751, 1994.

[77] L Arizmendi, JM Cabrera, and F Agullo-Lopez. Optical absorption spectra of nickel doped lithium niobate. *Ferroelectrics*, 26(1):823–826, 1980.

[78] Marcus Paul, Mitsuharu Tabuchi, and Anthony R West. Defect structure of ni, co-doped linbo3 and litao3. *Chemistry of materials*, 9(12):3206–3214, 1997.

[79] TR Volk, VI Pryalkin, and NM Rubinina. Optical-damage-resistant linbo 3: Zn crystal. *Optics letters*, 15(18):996–998, 1990.

[80] F Abdi, M Aillerie, M Fontana, P Bourson, T Volk, B Maximov, S Sulyanov, N Rubinina, and M Wöhlecke. Influence of zn doping on electrooptical properties and structure parameters of lithium niobate crystals. *Applied Physics B*, 68(5):795–799, 1999.

[81] U Schlarb, M Wöhlecke, B Gather, A Reichert, K Betzler, T Volk, and N Rubinina. Refractive indices of zn-doped lithium niobate. *Optical Materials*, 4(6):791–795, 1995.

[82] G Malovichko, V Grachev, E Kokanyan, and O Schirmer. Axial and low-symmetry centers of trivalent impurities in lithium niobate: Chromium in congruent and stoichiometric crystals. *Physical Review B*, 59(14):9113, 1999.

[83] Rajeev Bhatt, Sujan Kar, KS Bartwal, and VK Wadhawan. The effect of cr doping on optical and photoluminescence properties of linbo3 crystals. *Solid state communications*, 127(6):457–462, 2003.

[84] Yinfeng Dong, Shiguo Liu, Wei Li, Yongfa Kong, Shaolin Chen, and Jingjun Xu. Improved ultraviolet photorefractive properties of vanadium-doped lithium niobate crystals. *Optics letters*, 36(10):1779–1781, 2011.

[85] P Sheng, F Zeng, GS Tang, F Pan, WS Yan, and FC Hu. Structure and ferromagnetism in vanadium-doped linbo3. *Journal of Applied Physics*, 112(3):033913, 2012.

[86] Luca Razzari, Paolo Minzioni, Ilaria Cristiani, Vittorio Degiorgio, and Edvard P Kokanyan. Photorefractivity of hafnium-doped congruent lithium–niobate crystals. *Applied Physics Letters*, 86(13):131914, 2005.

[87] Paolo Minzioni, Ilaria Cristiani, Jin Yu, Jacopo Parravicini, Edvard P Kokanyan, and Vittorio Degiorgio. Linear and nonlinear optical properties of hafnium-doped lithium-niobate crystals. *Optics express*, 15(21):14171–14176, 2007.

[88] Mustapha Abarkan, Michel Aillerie, Jean-Paul Salvestrini, Marc D Fontana, and Edvard P Kokanyan. Electro-optic and dielectric properties of hafnium-doped congruent lithium niobate crystals. *Applied Physics B*, 92(4):603, 2008.

[89] TR Volk and NM Rubinina. A new optical damage resistant impurity in lithium niobate crystals: indium. *Ferroelectrics Letters Section*, 14(1-2):37–43, 1992.

[90] Yongfa Kong, Jinke Wen, and Huafu Wang. New doped lithium niobate crystal with high resistance to photorefraction—linbo3: In. *Applied physics letters*, 66(3):280–281, 1995.

[91] RV Schmidt and IP Kaminow. Metal-diffused optical waveguides in linbo3. *Applied Physics Letters*, 25(8):458–460, 1974.

[92] John Crank et al. *The mathematics of diffusion.* Oxford university press, 1979.

[93] G Bava, I Montrosset, WOLFGANG Sohler, and HUBERTUS Suche. Numerical modeling of ti: Linbo 3 integrated optical parametric oscillators. *IEEE journal of quantum electronics*, 23(1):42–51, 1987.

[94] Makoto Minakata, Shoichi Saito, and Masashi Shibata. Two dimensional distribution of refractive index changes in ti diffused linbo3 strip waveguides. *Journal of Applied Physics*, 50(5):3063–3067, 1979.

[95] E Strake, GP Bava, and Ivo Montrosset. Guided modes of ti: Linbo/sub 3/channel waveguides: a novel quasi-analytical technique in comparison with the scalar finite-element method. *Journal of lightwave technology*, 6(6):1126–1135, 1988.

[96] Toshiaki Suhara, Yuichi Handa, Hiroshi Nishihara, and Jiro Koyama. Analysis of optical channel waveguides and directional couplers with graded-index profile. *JOSA*, 69(6):807–815, 1979.

[97] Ramesh Kumar and Joyee Ghosh. Spdc in ppln ridge waveguide: an analysis for efficient twin photon generation at 1550 nm. *arXiv preprint arXiv:1709.09456*, 2017.

[98] Takahiro Inagaki, Nobuyuki Matsuda, Osamu Tadanaga, Masaki Asobe, and Hiroki Takesue. Entanglement distribution over 300 km of fiber. *Opt. Express*, 21(20):23241–23249, Oct 2013.

[99] Karolina Sedziak, Mikołaj Lasota, and Piotr Kolenderski. Reducing detection noise of a photon pair in a dispersive medium by controlling its spectral entanglement. *Optica*, 4(1):84–89, Jan 2017.

[100] Warren P Grice and Ian A Walmsley. Spectral information and distinguishability in type-ii down-conversion with a broadband pump. *Physical Review A*, 56(2):1627, 1997.

[101] Chandra M Natarajan, Michael G Tanner, and Robert H Hadfield. Superconducting nanowire single-photon detectors: physics and applications. *Superconductor science and technology*, 25(6):063001, 2012.

[102] G. N. Gol'tsman, O. Okunev, G. Chulkova, A. Lipatov, A. Semenov, K. Smirnov, B. Voronov, A. Dzardanov, C. Williams, and Roman Sobolewski. Picosecond superconducting single-photon optical detector. *Applied Physics Letters*, 79(6):705–707, 2001.

[103] WK Wooters and WK Zurek. Quantum no-cloning theorem. *Nature*, 299:802, 1982.

[104] Philippe H. Eberhard. Background level and counter efficiencies required for a loophole-free Einstein-Podolsky-Rosen experiment. *Phys. Rev. A*, 47:R747–R750, Feb 1993.

[105] Michael Varnava, Daniel E. Browne, and Terry Rudolph. How good must single photon sources and detectors be for efficient linear optical quantum computation? *Phys. Rev. Lett.*, 100:060502, Feb 2008.

[106] D Rosenberg, AJ Kerman, RJ Molnar, and EA Dauler. High-speed and high-efficiency superconducting nanowire single photon detector array. *Optics express*, 21(2):1440–1447, 2013.

[107] Shigehito Miki, Taro Yamashita, Hirotaka Terai, and Zhen Wang. High performance fiber-coupled nbtin superconducting nanowire single photon detectors with gifford-mcmahon cryocooler. *Optics express*, 21(8):10208–10214, 2013.

[108] Varun B Verma, Boris Korzh, Felix Bussieres, Robert D Horansky, Shellee D Dyer, Adriana E Lita, Igor Vayshenker, Francesco Marsili, Matthew D Shaw, Hugo Zbinden, et al. High-efficiency superconducting nanowire single-photon detectors fabricated from mosi thin-films. *Optics express*, 23(26):33792–33801, 2015.

[109] F Marsili, Varun B Verma, Jeffrey A Stern, S Harrington, Adriana E Lita, Thomas Gerrits, Igor Vayshenker, Burm Baek, Matthew D Shaw, Richard P Mirin, et al. Detecting single infrared photons with 93% system efficiency. *Nature Photonics*, 7(3):210, 2013.

[110] Andrew J Kerman, Eric A Dauler, William E Keicher, Joel KW Yang, Karl K Berggren, G Gol'Tsman, and B Voronov. Kinetic-inductance-limited reset time of superconducting nanowire photon counters. *Applied physics letters*, 88(11):111116, 2006.

[111] Bryan S Robinson, Andrew J Kerman, Eric A Dauler, Richard J Barron, David O Caplan, Mark L Stevens, John J Carney, Scott A Hamilton, Joel K Yang, and Karl K Berggren. 781 mbit/s photon-counting optical communications using a superconducting nanowire detector. *Optics letters*, 31(4):444–446, 2006.

[112] F. Marsili, F. Najafi, E. Dauler, R. J. Molnar, and K. K. Berggren. Afterpulsing and instability in superconducting nanowire avalanche photodetectors. *Applied Physics Letters*, 100(11):112601, 2012.

[113] Andrew J Kerman, Bryan S Robinson, Richard J Barron, David O Caplan, Mark L Stevens, John J Carney, Scott A Hamilton, William E Keicher, Eric A Dauler, Joel KW Yang, et al. Superconducting nanowire single-photon detectors. In *2006 Digest of the LEOS Summer Topical Meetings*, pages 9–10. IEEE, 2006.

[114] D N Klyshko. Use of two-photon light for absolute calibration of photoelectric detectors. *Soviet Journal of Quantum Electronics*, 10(9):1112–1117, sep 1980.

[115] P J Mosley, J S Lundeen, B J Smith, and I A Walmsley. Conditional preparation of single photons using parametric downconversion: a recipe for purity. *New Journal of Physics*, 10(9):093011, sep 2008.

[116] P. G. Evans, R. S. Bennink, W. P. Grice, T. S. Humble, and J. Schaake. Bright source of spectrally uncorrelated polarization-entangled photons with nearly single-mode emission. *Phys. Rev. Lett.*, 105:253601, Dec 2010.

[117] Andreas Eckstein, Andreas Christ, Peter J. Mosley, and Christine Silberhorn. Highly efficient single-pass source of pulsed single-mode twin beams of light. *Phys. Rev. Lett.*, 106:013603, Jan 2011.

[118] Masahiro Yabuno, Ryosuke Shimizu, Yasuyoshi Mitsumori, Hideo Kosaka, and Keiichi Edamatsu. Four-photon quantum interferometry at a telecom wavelength. *Phys. Rev. A*, 86:010302, Jul 2012.

[119] J.H. Eberly. Schmidt analysis of pure-state entanglement. *Laser Phys.*, 16(921), 2006.

[120] Roy J Glauber. The quantum theory of optical coherence. *Physical Review*, 130(6):2529, 1963.

[121] Mark Fox. *Quantum optics: an introduction*, volume 15. OUP Oxford, 2006.

[122] Jeff H. Kimble, Mario Dagenais, and Leonard Mandel. Photon antibunching in resonance fluorescence. *Physical Review Letters*, 39(11):691, 1977.

[123] E Bocquillon, C Couteau, M Razavi, R Laflamme, and G Weihs. Coherence measures for heralded single-photon sources. *Physical Review A*, 79(3):035801, 2009.

[124] Andreas Christ, Kaisa Laiho, Andreas Eckstein, Katiúscia N Cassemiro, and Christine Silberhorn. Probing multimode squeezing with correlation functions. *New Journal of Physics*, 13(3):033027, mar 2011.

[125] C. K. Hong, Z. Y. Ou, and L. Mandel. Measurement of subpicosecond time intervals between two photons by interference. *Phys. Rev. Lett.*, 59:2044–2046, Nov 1987.

[126] TB Pittman, BC Jacobs, and JD Franson. Heralding single photons from pulsed parametric down-conversion. *Optics communications*, 246(4-6):545–550, 2005.

[127] FW Sun, CW Wong, et al. Indistinguishability of independent single photons. *Physical Review A*, 79(1):013824, 2009.

[128] Naoshi Uesugi and Tatsuya Kimura. Efficient second-harmonic generation in three-dimensional linbo3 optical waveguide. *Applied Physics Letters*, 29(9):572–574, 1976.

[129] R Regener and W Sohler. Loss in low-finesse ti: Linbo3 optical waveguide resonators. *Appl. Phys. B*, 36(3):143–147, 1985.

[130] WM Young, RS Feigelson, Martin M Fejer, Michel JF Digonnet, and Herbert J Shaw. Photorefractive-damage-resistant zn-diffused waveguides in mgo: Linbo 3. *Optics letters*, 16(13):995–997, 1991.

[131] WM Young, Martin M Fejer, Michel JF Digonnet, AF Marshall, and RS Feigelson. Fabrication, characterization and index profile modeling of high-damage resistance zn-diffused waveguides in congruent and mgo: lithium niobate. *Journal of lightwave technology*, 10(9):1238–1246, 1992.

[132] F. Schiller, B. Herreros, and G. Lifante. Optical characterization of vapor zn-diffused waveguides in lithium niobate. *J. Opt. Soc. Am. A*, 14(2):425–429, Feb 1997.

[133] Kiyomasa Sugii, Masaharu Fukuma, and Hiroshi Iwasaki. A study on titanium diffusion into linbo3 waveguides by electron probe analysis and x-ray diffraction methods. *J. Mater. Sci.*, 13(3):523–533, 1978.

[134] W Minford, S Korotky, and R Alferness. Low-loss ti: Linbo 3 waveguide bends at λ= 1.3 μm. *IEEE Journal of Quantum Electronics*, 18(10):1802–1806, 1982.

[135] Masaharu Fukuma, Juichi Noda, and Hiroshi Iwasaki. Optical properties in titanium-diffused linbo3 strip waveguides. *Journal of Applied Physics*, 49(7):3693–3698, 1978.

[136] R Keil and F Auracher. Coupling of single-mode ti-diffused linbo3 waveguides to single-mode fibers. *Optics Communications*, 30(1):23–28, 1979.

[137] R Alferness, V Ramaswamy, S Korotky, M Divino, and L Buhl. Efficient single-mode fiber to titanium diffused lithium niobate waveguide coupling for λ= 1.32 μm. *IEEE Journal of Quantum Electronics*, 18(10):1807–1813, 1982.

[138] J Watson, M Milbrodt, and T Rice. A polarization-independent 1× 16 guided-wave optical switch integrated on lithium niobate. *Journal of lightwave technology*, 4(11):1717–1721, 1986.

[139] Wolfgang Sohler, Hui Hu, Raimund Ricken, Viktor Quiring, Christoph Vannahme, Harald Herrmann, Daniel Büchter, Selim Reza, Werner Grundkötter, Sergey Orlov, et al. Integrated optical devices in lithium niobate. *Optics and Photonics News*, 19(1):24–31, 2008.

[140] Pei-Kuen Wei and Way-Seen Wang. A te-tm mode splitter on lithium niobate using ti, ni, and mgo diffusions. *IEEE photonics technology letters*, 6(2):245–248, 1994.

[141] Sébastien Tanzilli, Hugues De Riedmatten, H Tittel, Hugo Zbinden, Pascal Baldi, Marc De Micheli, Daniel Barry Ostrowsky, and Nicolas Gisin. Highly efficient photon-pair source using periodically poled lithium niobate waveguide. *Electron. Lett.*, 37(1):26–28, 2001.

[142] S. Tanzilli, W. Tittel, H. De Riedmatten, H. Zbinden, P. Baldi, M. DeMicheli, D.B. Ostrowsky, and N. Gisin. Ppln waveguide for quantum communication. *EPJ D*, 18(2):155–160, 2002.

[143] Stefania Castelletto, Ivo Pietro Degiovanni, Valentina Schettini, Tommaso Del Rosso, Giancarlo Margheri, Leonardo Papi, and Stefano Sottini. Comparison of photon counting and analog techniques for the measurement of photon pair generation in a ppln waveguide. *JOSA B*, 25(1):7–14, 2008.

[144] Christian Kurtsiefer, Markus Oberparleiter, and Harald Weinfurter. High-efficiency entangled photon pair collection in type-ii parametric fluorescence. *Phys. Rev. A*, 64:023802, Jul 2001.

[145] Go Fujii, Naoto Namekata, Masayuki Motoya, Sunao Kurimura, and Shuichiro Inoue. Bright narrowband source of photon pairs at optical telecommunication wavelengths using a type-ii periodically poled lithium niobate waveguide. *Opt. Express*, 15(20):12769–12776, 2007.

[146] Anthony Martin, Valentina Cristofori, Pierre Aboussouan, Harrald Herrmann, Wolfgang Sohler, Daniel Barry Ostrowsky, Olivier Alibart, and Sébastien Tanzilli. Integrated optical source of polarization entangled photons at 1310 nm. *Optics express*, 17(2):1033–1041, 2009.

[147] Kazuhisa Yamamoto, Hiroaki Yamamoto, and Tetsuo Taniuchi. Simultaneous sum-frequency and second-harmonic generation from a proton-exchanged mgo-doped linbo3 waveguide. *Applied physics letters*, 58(12):1227–1229, 1991.

[148] Kazuya Hayata and Masanori Koshiba. Numerical study of guided-wave sum-frequency generation through second-order nonlinear parametric processes. *JOSA B*, 8(2):449–458, 1991.

[149] T Suhara and H Ishizuki. Integrated qpm sum-frequency generation interferometer device for ultrafast optical switching. *IEEE Photonics Technology Letters*, 13(11):1203–1205, 2001.

[150] H Herrmann and Wolfgang Sohler. Difference-frequency generation of tunable, coherent mid-infrared radiation in ti: Linbo 3 channel waveguides. *JOSA B*, 5(2):278–284, 1988.

[151] EJ Lim, HM Hertz, ML Bortz, and MM Fejer. Infrared radiation generated by quasi-phase-matched difference-frequency mixing in a periodically poled lithium niobate waveguide. *Applied physics letters*, 59(18):2207–2209, 1991.

[152] CQ Xu, H Okayama, K Shinozaki, K Watanabe, and M Kawahara. Wavelength conversions 1.5 μm by difference frequency generation in periodically domain-inverted linbo3 channel waveguides. *Applied physics letters*, 63(9):1170–1172, 1993.

[153] G Schreiber, H Suche, YL Lee, W Grundkötter, V Quiring, R Ricken, and W Sohler. Efficient cascaded difference frequency conversion in periodically poled ti: Linbo3 waveguides using pulsed and cw pumping. *Applied Physics B*, 73(5-6):501–504, 2001.

[154] Katsuaki Komatsu, Michikazu Kondo, and Y Ohta. Titanium/magnesium double diffusion method for efficient fibre-linbo3 waveguide coupling. *Electronics Letters*, 22(17):881–882, 1986.

[155] JR Carruthers, IP Kaminow, and LW Stulz. Diffusion kinetics and optical waveguiding properties of outdiffused layers in lithium niobate and lithium tantalate. *Applied optics*, 13(10):2333–2342, 1974.

[156] Philippe H. Eberhard. Background level and counter efficiencies required for a loophole-free Einstein-Podolsky-Rosen experiment. *Phys. Rev. A*, 47:R747–R750, Feb 1993.

[157] J. S. Neergaard-Nielsen, B. Melholt Nielsen, H. Takahashi, A. I. Vistnes, and E. S. Polzik. High purity bright single photon source. *Opt. Express*, 15(13):7940–7949, Jun 2007.

[158] P. Ben Dixon, Danna Rosenberg, Veronika Stelmakh, Matthew E. Grein, Ryan S. Bennink, Eric A. Dauler, Andrew J. Kerman, Richard J. Molnar, and Franco N. C. Wong. Heralding efficiency and correlated-mode coupling of near-IR fiber-coupled photon pairs. *Phys. Rev. A*, 90:043804, Oct 2014.

[159] JM White and PF Heidrich. Optical waveguide refractive index profiles determined from measurement of mode indices: a simple analysis. *Appl. Opt*, 15(1):151–155, 1976.

[160] Krishnan R. Parameswaran, Roger K. Route, Jonathan R. Kurz, Rostislav V. Roussev, Martin M. Fejer, and Masatoshi Fujimura. Highly efficient second-harmonic generation in buried waveguides formed by annealed and reverse proton exchange in periodically poled lithium niobate. *Opt. Lett.*, 27(3):179–181, Feb 2002.

[161] Yun-Kun Jiang and Akihisa Tomita. The generation of polarization-entangled photon pairs using periodically poled lithium niobate waveguides in a fibre loop. *J. Phys. B*, 40(2):437, 2007.

[162] Shin Arahira, Naoto Namekata, Tadashi Kishimoto, Hiroki Yaegashi, and Shuichiro Inoue. Generation of polarization entangled photon pairs at telecommunication wavelength using cascaded χ (2) processes in a periodically poled linbo 3 ridge waveguide. *Opt. Express*, 19(17):16032–16043, 2011.

[163] Shin Arahira, Tadashi Kishimoto, and Hitoshi Murai. 1.5-μm band polarization entangled photon-pair source with variable bell states. *Opt. Express*, 20(9):9862–9875, 2012.

[164] Thomas Meany, Lutfi A. Ngah, Matthew J. Collins, Alex S. Clark, Robert J. Williams, Benjamin J. Eggleton, M. J. Steel, Michael J. Withford, Olivier Alibart, and Sébastien Tanzilli. Hybrid photonic circuit for multiplexed heralded single photons. *Laser Photon. Rev.*, 8(3):L42–L46, 2014.

[165] Florian Kaiser, Bruno Fedrici, Alessandro Zavatta, Virginia D'Auria, and Sébastien Tanzilli. A fully guided-wave squeezing experiment for fiber quantum networks. *Optica*, 3(4):362–365, 2016.

[166] Alexander Schlehahn, Sarah Fischbach, Ronny Schmidt, Arsenty Kaganskiy, André Strittmatter, Sven Rodt, Tobias Heindel, and Stephan Reitzenstein. A stand-alone fiber-coupled single-photon source. *Scientific reports*, 8(1):1340, 2018.

[167] Fumihiro Kaneda, Karina Garay-Palmett, Alfred B U'Ren, and Paul G Kwiat. Heralded single-photon source utilizing highly nondegenerate, spectrally factorable spontaneous parametric downconversion. *Opt. Express*, 24(10):10733–10747, 2016.

[168] Enrico Pomarico, Bruno Sanguinetti, Thiago Guerreiro, Rob Thew, and Hugo Zbinden. Mhz rate and efficient synchronous heralding of single photons at telecom wavelengths. *Opt. Express*, 20(21):23846–23855, Oct 2012.

[169] Stephan Krapick, Harald Herrmann, Viktor Quiring, Benjamin Brecht, Hubertus Suche, and Ch Silberhorn. An efficient integrated two-color source for heralded single photons. *New J. Phys.*, 15(3):033010, 2013.

[170] Matthias Bock, Andreas Lenhard, Christopher Chunnilall, and Christoph Becher. Highly efficient heralded single-photon source for telecom wavelengths based on a ppln waveguide. *Opt. Express*, 24(21):23992–24001, Oct 2016.

[171] T Guerreiro, Anthony Martin, Bruno Sanguinetti, Natalia Bruno, Hugo Zbinden, and RT Thew. High efficiency coupling of photon pairs in practice. *Opt. Express*, 21(23):27641–27651, 2013.

[172] Georg Harder, Vahid Ansari, Benjamin Brecht, Thomas Dirmeier, Christoph Marquardt, and Christine Silberhorn. An optimized photon pair source for quantum circuits. *Opt. Express*, 21(12):13975–13985, 2013.

[173] Marcelo Da Cunha Pereira, Francisco E Becerra, Boris L Glebov, Jingyun Fan, Sae Woo Nam, and Alan Migdall. Demonstrating highly symmetric single-mode, single-photon heralding efficiency in spontaneous parametric downconversion. *Opt. Lett.*, 38(10):1609–1611, 2013.

[174] Morgan M Weston, Helen M Chrzanowski, Sabine Wollmann, Allen Boston, Joseph Ho, Lynden K Shalm, Varun B Verma, Michael S Allman, Sae Woo Nam, Raj B Patel, et al. Efficient and pure femtosecond-pulse-length source of polarization-entangled photons. *Opt. Express*, 24(10):10869–10879, 2016.

[175] Lynden K. Shalm, Evan Meyer-Scott, Bradley G. Christensen, Peter Bierhorst, Michael A. Wayne, Martin J. Stevens, Thomas Gerrits, Scott Glancy, Deny R. Hamel, Michael S. Allman, Kevin J. Coakley, Shellee D. Dyer, Carson Hodge, Adriana E. Lita, Varun B. Verma, Camilla Lambrocco, Edward Tortorici, Alan L. Migdall, Yanbao Zhang, Daniel R. Kumor, William H. Farr, Francesco Marsili, Matthew D. Shaw, Jeffrey A. Stern, Carlos Abellán, Waldimar Amaya, Valerio

Pruneri, Thomas Jennewein, Morgan W. Mitchell, Paul G. Kwiat, Joshua C. Bienfang, Richard P. Mirin, Emanuel Knill, and Sae Woo Nam. Strong loophole-free test of local realism. *Phys. Rev. Lett.*, 115:250402, Dec 2015.

[176] Marissa Giustina, Marijn A. M. Versteegh, Sören Wengerowsky, Johannes Handsteiner, Armin Hochrainer, Kevin Phelan, Fabian Steinlechner, Johannes Kofler, Jan-Åke Larsson, Carlos Abellán, Waldimar Amaya, Valerio Pruneri, Morgan W. Mitchell, Jörn Beyer, Thomas Gerrits, Adriana E. Lita, Lynden K. Shalm, Sae Woo Nam, Thomas Scheidl, Rupert Ursin, Bernhard Wittmann, and Anton Zeilinger. Significant-loophole-free test of bell's theorem with entangled photons. *Phys. Rev. Lett.*, 115:250401, Dec 2015.

[177] Sven Ramelow, Alexandra Mech, Marissa Giustina, Simon Gröblacher, Witlef Wieczorek, Jörn Beyer, Adriana Lita, Brice Calkins, Thomas Gerrits, Sae Woo Nam, Anton Zeilinger, and Rupert Ursin. Highly efficient heralding of entangled single photons. *Opt. Express*, 21(6):6707–6717, Mar 2013.

[178] Qiang Zhang, Xiuping Xie, Hiroki Takesue, Sae Woo Nam, Carsten Langrock, MM Fejer, and Yoshihisa Yamamoto. Correlated photon-pair generation in reverse-proton-exchange ppln waveguides with integrated mode demultiplexer at 10 ghz clock. *Opt. Express*, 15(16):10288–10293, 2007.

[179] H. Jin, F. M. Liu, P. Xu, J. L. Xia, M. L. Zhong, Y. Yuan, J. W. Zhou, Y. X. Gong, W. Wang, and S. N. Zhu. On-chip generation and manipulation of entangled photons based on reconfigurable lithium-niobate waveguide circuits. *Phys. Rev. Lett.*, 113:103601, Sep 2014.

[180] Harald Herrmann, Xu Yang, Abu Thomas, Andreas Poppe, Wolfgang Sohler, and Christine Silberhorn. Post-selection free, integrated optical source of non-degenerate, polarization entangled photon pairs. *Opt. Express*, 21(23):27981–27991, 2013.

[181] Rodney Loudon. *The quantum theory of light.* OUP Oxford, 2000.

[182] Malte Avenhaus, Andreas Eckstein, Peter J Mosley, and Christine Silberhorn. Fiber-assisted single-photon spectrograph. *Opt. Lett.*, 34(18):2873–2875, 2009.

[183] Thomas Gerrits, Francesco Marsili, Varun B Verma, Lynden K Shalm, Matthew Shaw, RP Mirin, and Sae Woo Nam. Spectral correlation measurements at the hong-ou-mandel interference dip. *Physical Review A*, 91(1):013830, 2015.

[184] Katiúscia N Cassemiro, Kaisa Laiho, and Christine Silberhorn. Accessing the purity of a single photon by the width of the hong–ou–mandel interference. *New J. Phys.*, 12(11):113052, 2010.

[185] Andreas Eckstein, Andreas Christ, Peter J. Mosley, and Christine Silberhorn. Realistic g(2) measurement of a pdc source with single photon detectors in the presence of background. *Phys. Status Solidi C*, 8(4):1216–1219, 2011.

[186] Evan Meyer-Scott, Nicola Montaut, Johannes Tiedau, Linda Sansoni, Harald Herrmann, Tim J Bartley, and Christine Silberhorn. Limits on the heralding efficiencies and spectral purities of spectrally filtered single photons from photon-pair sources. *Physical Review A*, 95(6):061803, 2017.

[187] T Aichele, Alexander I Lvovsky, and S Schiller. Optical mode characterization of single photons prepared by means of conditional measurements on a biphoton state. *EPJ D*, 18(2):237–245, 2002.

[188] Pierre Aboussouan, Olivier Alibart, Daniel B Ostrowsky, Pascal Baldi, and Sébastien Tanzilli. High-visibility two-photon interference at a telecom wavelength using picosecond-regime separated sources. *Phys. Rev. A*, 81(2):021801, 2010.

[189] Matthias Leifgen, Tim Schröder, Friedemann Gädeke, Robert Riemann, Valentin Métillon, Elke Neu, Christian Hepp, Carsten Arend, Christoph Becher, Kristian Lauritsen, and Oliver Benson. Evaluation of nitrogen- and silicon-vacancy defect centres as single photon sources in quantum key distribution. *New J. Phys.*, 16(2):023021, 2014.

[190] K Laiho, A Christ, KN Cassemiro, and C Silberhorn. Testing spectral filters as gaussian quantum optical channels. *Opt. Lett.*, 36(8):1476–1478, 2011.

[191] Raj B Patel, Anthony J Bennett, Ian Farrer, Christine A Nicoll, David A Ritchie, and Andrew J Shields. Two-photon interference of the emission from electrically tunable remote quantum dots. *Nature photonics*, 4(9):632, 2010.

[192] Ayman F Abouraddy, Magued B Nasr, Bahaa EA Saleh, Alexander V Sergienko, and Malvin C Teich. Quantum-optical coherence tomography with dispersion cancellation. *Physical Review A*, 65(5):053817, 2002.

[193] Hiroki Takesue, Shellee D Dyer, Martin J Stevens, Varun Verma, Richard P Mirin, and Sae Woo Nam. Quantum teleportation over 100 km of fiber using highly efficient superconducting nanowire single-photon detectors. *Optica*, 2(10):832–835, 2015.

[194] Raju Valivarthi, Qiang Zhou, Gabriel H Aguilar, Varun B Verma, Francesco Marsili, Matthew D Shaw, Sae Woo Nam, Daniel Oblak, Wolfgang Tittel, et al. Quantum teleportation across a metropolitan fibre network. *Nature Photonics*, 10(10):676, 2016.

[195] Qi-Chao Sun, Ya-Li Mao, Si-Jing Chen, Wei Zhang, Yang-Fan Jiang, Yan-Bao Zhang, Wei-Jun Zhang, Shigehito Miki, Taro Yamashita, Hirotaka Terai, et al. Quantum teleportation with independent sources and prior entanglement distribution over a network. *Nature Photonics*, 10(10):671, 2016.

[196] Hiroki Takesue and Benjamin Miquel. Entanglement swapping using telecom-band photons generated in fibers. *Optics express*, 17(13):10748–10756, 2009.

[197] Yinghong Xue, Akio Yoshizawa, and Hidemi Tsuchida. Polarization-based entanglement swapping at the telecommunication wavelength using spontaneous parametric down-conversion photon-pair sources. *Physical Review A*, 85(3):032337, 2012.

[198] Rui-Bo Jin, Masahiro Takeoka, Utako Takagi, Ryosuke Shimizu, and Masahide Sasaki. Highly efficient entanglement swapping and teleportation at telecom wavelength. *Scientific reports*, 5:9333, 2015.

[199] Jeongwan Jin, M Grimau Puigibert, Lambert Giner, Joshua A Slater, Michael RE Lamont, Varun B Verma, MD Shaw, Francesco Marsili, Sae Woo Nam, Daniel Oblak, et al. Entanglement swapping with quantum-memory-compatible photons. *Physical Review A*, 92(1):012329, 2015.

[200] Agata M Brańczyk, TC Ralph, Wolfram Helwig, and Christine Silberhorn. Optimized generation of heralded fock states using parametric down-conversion. *New Journal of Physics*, 12(6):063001, 2010.

[201] Lei Yang, Xiaoxin Ma, Xueshi Guo, Liang Cui, and Xiaoying Li. Characterization of a fiber-based source of heralded single photons. *Physical Review A*, 83(5):053843, 2011.

[202] Warren P Grice, Alfred B U'Ren, and Ian A Walmsley. Eliminating frequency and space-time correlations in multiphoton states. *Physical Review A*, 64(6):063815, 2001.

[203] Alfred B U'Ren, Christine Silberhorn, Reinhard Erdmann, Konrad Banaszek, Warren P Grice, Ian A Walmsley, and Michael G Raymer. Generation of pure-state single-photon wavepackets by conditional preparation based on spontaneous parametric downconversion. *arXiv preprint quant-ph/0611019*, 2006.

[204] K Garay-Palmett, HJ McGuinness, Offir Cohen, JS Lundeen, R Rangel-Rojo, AB U'ren, MG Raymer, CJ McKinstrie, S Radic, and IA Walmsley. Photon pair-state preparation with tailored spectral properties by spontaneous four-wave mixing in photonic-crystal fiber. *Optics express*, 15(22):14870–14886, 2007.

[205] Matthaeus Halder, Jeremie Fulconis, Ben Cemlyn, Alex Clark, Chunle Xiong, William J Wadsworth, and John G Rarity. Nonclassical 2-photon interference with separate intrinsically narrowband fibre sources. *Optics express*, 17(6):4670–4676, 2009.

[206] Zachary H Levine, Jingyun Fan, Jun Chen, A Ling, and A Migdall. Heralded, pure-state single-photon source based on a potassium titanyl phosphate waveguide. *Optics express*, 18(4):3708–3718, 2010.

[207] Thomas Gerrits, Martin J Stevens, Burm Baek, Brice Calkins, Adriana Lita, Scott Glancy, Emanuel Knill, Sae Woo Nam, Richard P Mirin, Robert H Hadfield, et al. Generation of degenerate, factorizable, pulsed squeezed light at telecom wavelengths. *Optics express*, 19(24):24434–24447, 2011.

[208] Bin Fang, Offir Cohen, Jamy B Moreno, and Virginia O Lorenz. State engineering of photon pairs produced through dual-pump spontaneous four-wave mixing. *Optics express*, 21(3):2707–2717, 2013.

[209] Chih-Sung Chuu, GY Yin, and SE Harris. A miniature ultrabright source of temporally long, narrowband biphotons. *Applied Physics Letters*, 101(5):051108, 2012.

[210] Kai-Hong Luo, Harald Herrmann, Stephan Krapick, Benjamin Brecht, Raimund Ricken, Viktor Quiring, Hubertus Suche, Wolfgang Sohler, and Christine Silberhorn. Direct generation of genuine single-longitudinal-mode narrowband photon pairs. *New Journal of Physics*, 17(7):073039, 2015.

[211] Yasser Jeronimo-Moreno, Saul Rodriguez-Benavides, and Alfred B U'Ren. Theory of cavity-enhanced spontaneous parametric downconversion. *Laser physics*, 20(5):1221–1233, 2010.

[212] Xiao-Hui Bao, Yong Qian, Jian Yang, Han Zhang, Zeng-Bing Chen, Tao Yang, and Jian-Wei Pan. Generation of narrow-band polarization-entangled photon pairs for atomic quantum memories. *Physical review letters*, 101(19):190501, 2008.

[213] Matthias Scholz, Lars Koch, and Oliver Benson. Statistics of narrow-band single photons for quantum memories generated by ultrabright cavity-enhanced parametric down-conversion. *Physical review letters*, 102(6):063603, 2009.

[214] Julia Fekete, Daniel Rieländer, Matteo Cristiani, and Hugues de Riedmatten. Ultranarrow-band photon-pair source compatible with solid state quantum memories and telecommunication networks. *Physical review letters*, 110(22):220502, 2013.

[215] CK Law, Ian A Walmsley, and JH Eberly. Continuous frequency entanglement: effective finite hilbert space and entropy control. *Physical Review Letters*, 84(23):5304, 2000.

[216] Natalia Bruno, E Zambrini Cruzeiro, Anthony Martin, and RT Thew. Simple, pulsed, polarization entangled photon pair source. *Optics Communications*, 327:3–6, 2014.

[217] Xi-Lin Wang, Luo-Kan Chen, Wei Li, H-L Huang, Chang Liu, Chao Chen, Y-H Luo, Z-E Su, Dian Wu, Z-D Li, et al. Experimental ten-photon entanglement. *Physical review letters*, 117(21):210502, 2016.

[218] Panagiotis Vergyris, Thomas Meany, Tommaso Lunghi, Gregory Sauder, James Downes, MJ Steel, Michael J Withford, Olivier Alibart, and Sébastien Tanzilli. On-chip generation of heralded photon-number states. *Scientific reports*, 6:35975, 2016.

[219] Luo-Kan Chen, Zheng-Da Li, Xing-Can Yao, Miao Huang, Wei Li, He Lu, Xiao Yuan, Yan-Bao Zhang, Xiao Jiang, Cheng-Zhi Peng, et al. Observation of ten-photon entanglement using thin bib 3 o 6 crystals. *Optica*, 4(1):77–83, 2017.

[220] Jefferson Flórez, Omar Calderón, Alejandra Valencia, and Clara I Osorio. Correlation control for pure and efficiently generated heralded single photons. *Physical Review A*, 91(1):013819, 2015.

[221] CI Osorio, N Sangouard, and Robert Thomas Thew. On the purity and indistinguishability of down-converted photons. *Journal of Physics B: Atomic, Molecular and Optical Physics*, 46(5):055501, 2013.

[222] A. V. Smith. Snlo nonlinear optics code.

[223] Fabian Laudenbach, Hannes Hübel, Michael Hentschel, Philip Walther, and Andreas Poppe. Modelling parametric down-conversion yielding spectrally pure photon pairs. *Optics Express*, 24(3):2712–2727, 2016.

[224] Abu Thomas. *Photon Pair Sources in Periodically Poled Ti: LiNbO3 Waveguides*. PhD thesis, Universitätsbibliothek, 2011.

[225] MG Tanner, L San Emeterio Alvarez, W Jiang, RJ Warburton, ZH Barber, and RH Hadfield. A superconducting nanowire single photon detector on lithium niobate. *Nanotechnology*, 23(50):505201, 2012.

[226] Damien Bonneau, Mirko Lobino, Pisu Jiang, Chandra M Natarajan, Michael G Tanner, Robert H Hadfield, Sanders N Dorenbos, Val Zwiller, Mark G Thompson, and Jeremy L O'Brien. Fast path and polarization manipulation of telecom wavelength single photons in lithium niobate waveguide devices. *Physical review letters*, 108(5):053601, 2012.

[227] Jan Philipp Höpker, Thomas Gerrits, Adriana Lita, Stephan Krapick, Harald Herrmann, Raimund Ricken, Viktor Quiring, Richard Mirin, Sae Woo Nam, Christine Silberhorn, et al. Integrated transition edge sensors on titanium in-diffused lithium niobate waveguides. *APL Photonics*, 4(5):056103, 2019.

[228] E Smirnov, A Golikov, P Zolotov, V Kovalyuk, M Lobino, B Voronov, A Korneev, and G Goltsman. Superconducting nanowire single-photon detector on lithium niobate. In *Journal of Physics: Conference Series*, volume 1124, page 051025. IOP Publishing, 2018.

[229] Charles H Bennett, Gilles Brassard, Claude Crépeau, and Richard Jozsa. Teleporting an unknown quantum state via dual classical and einstein-podolsky-rosen channels. *Phys. Rev. Lett*, 70(13):1895–1899, 1993.

[230] David P DiVincenzo. Quantum computation. *Science*, 270(5234):255–261, 1995.

[231] Seth Lloyd. Universal quantum simulators. *Science*, pages 1073–1078, 1996.

[232] Daniel Loss and David P DiVincenzo. Quantum computation with quantum dots. *Physical Review A*, 57(1):120, 1998.

[233] Peter W Shor. Polynomial-time algorithms for prime factorization and discrete logarithms on a quantum computer. *SIAM review*, 41(2):303–332, 1999.

[234] Michael A Nielsen and Isaac Chuang. Quantum computation and quantum information, 2002.

[235] Michael A Nielsen. Optical quantum computation using cluster states. *Physical review letters*, 93(4):040503, 2004.

[236] H Jeff Kimble. The quantum internet. *Nature*, 453(7198):1023, 2008.

[237] Benjamin P Lanyon, James D Whitfield, Geoff G Gillett, Michael E Goggin, Marcelo P Almeida, Ivan Kassal, Jacob D Biamonte, Masoud Mohseni, Ben J Powell, Marco Barbieri, et al. Towards quantum chemistry on a quantum computer. *Nature chemistry*, 2(2):106, 2010.

[238] Andrew A Houck, Hakan E Türeci, and Jens Koch. On-chip quantum simulation with superconducting circuits. *Nature Physics*, 8(4):292, 2012.

[239] Iulia M Georgescu, Sahel Ashhab, and Franco Nori. Quantum simulation. *Reviews of Modern Physics*, 86(1):153, 2014.

[240] Tomi Johnson, Stephan Clark, and Dieter Jaksch. What is a quantum simulator? *EPJ Quantum Technology*, 1(1-12), July 2014.

[241] John Goold, Marcus Huber, Arnau Riera, Lídia del Rio, and Paul Skrzypczyk. The role of quantum information in thermodynamics—a topical review. *Journal of Physics A: Mathematical and Theoretical*, 49(14):143001, feb 2016.

[242] Jacob Biamonte, Peter Wittek, Nicola Pancotti, Patrick Rebentrost, Nathan Wiebe, and Seth Lloyd. Quantum machine learning. *Nature*, 549(7671):195, 2017.

[243] Bruno Huttner, Nobuyuki Imoto, Nicolas Gisin, and Tsafrir Mor. Quantum cryptography with coherent states. *Physical Review A*, 51(3):1863, 1995.

[244] Dominic Mayers. Unconditional security in quantum cryptography. *Journal of the ACM (JACM)*, 48(3):351–406, 2001.

[245] Alexios Beveratos, Rosa Brouri, Thierry Gacoin, André Villing, Jean-Philippe Poizat, and Philippe Grangier. Single photon quantum cryptography. *Physical review letters*, 89(18):187901, 2002.

[246] Charles H Bennett and Gilles Brassard. Quantum cryptography: public key distribution and coin tossing. *Theor. Comput. Sci.*, 560(12):7–11, 2014.

[247] Peter Komar, Eric M Kessler, Michael Bishof, Liang Jiang, Anders S Sørensen, Jun Ye, and Mikhail D Lukin. A quantum network of clocks. *Nature Physics*, 10(8):582, 2014.

[248] Rajeev Motwani and Prabhakar Raghavan. *Randomized algorithms.* Cambridge university press, 1995.

[249] Carlos Pedro Gonçalves. Quantum financial economics—risk and returns. *Journal of Systems Science and Complexity*, 26(2):187–200, 2013.

[250] Ralph K Cavin, Paolo Lugli, and Victor V Zhirnov. Science and engineering beyond moore's law. *Proceedings of the IEEE*, 100(Special Centennial Issue):1720–1749, 2012.

[251] Igor L. Markov. Limits on fundamental limits to computation. *Nature*, 512:147 EP –, 08 2014.

[252] Rolf Landauer. Irreversibility and heat generation in the computing process. *IBM journal of research and development*, 5(3):183–191, 1961.

[253] https://feverkill.com/post/?i=how-much-cooling-does-your-pc-really-need. October 2017.

[254] Martin Hellman. A cryptanalytic time-memory trade-off. *IEEE transactions on Information Theory*, 26(4):401–406, 1980.

[255] Philippe Oechslin. Making a faster cryptanalytic time-memory trade-off. In *Annual International Cryptology Conference*, pages 617–630. Springer, 2003.

[256] Mark Stamp. Once upon a time-memory tradeoff. *San Jose State University, Department of Computer Science*, 2003.

[257] Robert R Schaller. Moore's law: past, present and future. *IEEE spectrum*, 34(6):52–59, 1997.

[258] Chris A Mack. Fifty years of moore's law. *IEEE Transactions on semiconductor manufacturing*, 24(2):202–207, 2011.

[259] M Mitchell Waldrop. The chips are down for moore's law. *Nature News*, 530(7589):144, 2016.

[260] Gordon E Moore et al. Cramming more components onto integrated circuits, 1965.

[261] Dik Bouwmeester, Jian-Wei Pan, Klaus Mattle, Manfred Eibl, Harald Weinfurter, and Anton Zeilinger. Experimental quantum teleportation. *Nature*, 390(6660):575, 1997.

[262] S. Pirandola, J. Eisert, C. Weedbrook, A. Furusawa, and S. L. Braunstein. Advances in quantum teleportation. *Nature Photonics*, 9:641 EP –, 09 2015.

[263] Costantino Agnesi, Francesco Vedovato, Matteo Schiavon, Daniele Dequal, Luca Calderaro, Marco Tomasin, Davide G Marangon, Andrea Stanco, Vincenza Luceri, Giuseppe Bianco, et al. Exploring the boundaries of quantum mechanics: advances in satellite quantum communications. *Philosophical Transactions of the Royal Society A: Mathematical, Physical and Engineering Sciences*, 376(2123):20170461, 2018.

[264] CL Philip Chen and Chun-Yang Zhang. Data-intensive applications, challenges, techniques and technologies: A survey on big data. *Information sciences*, 275:314–347, 2014.

[265] Vijey Thayananthan and Aiiad Albeshri. Big data security issues based on quantum cryptography and privacy with authentication for mobile data center. *Procedia Computer Science*, 50:149–156, 2015.

[266] Alán Aspuru-Guzik and Philip Walther. Photonic quantum simulators. *Nature physics*, 8(4):285, 2012.

[267] Klaus Mattle, Harald Weinfurter, Paul G Kwiat, and Anton Zeilinger. Dense coding in experimental quantum communication. *Physical Review Letters*, 76(25):4656, 1996.

[268] RM Stevenson, RM Thompson, AJ Shields, I Farrer, BE Kardynal, DA Ritchie, and M Pepper. Quantum dots as a photon source for passive quantum key encoding. *Physical Review B*, 66(8):081302, 2002.

[269] Jeremy L O'brien, Akira Furusawa, and Jelena Vučković. Photonic quantum technologies. *Nature Photonics*, 3(12):687, 2009.

[270] Brian Vlastakis, Gerhard Kirchmair, Zaki Leghtas, Simon E Nigg, Luigi Frunzio, Steven M Girvin, Mazyar Mirrahimi, Michel H Devoret, and Robert J Schoelkopf. Deterministically encoding quantum information using 100-photon schrödinger cat states. *Science*, 342(6158):607–610, 2013.

[271] Lan-Tian Feng, Ming Zhang, Zhi-Yuan Zhou, Ming Li, Xiao Xiong, Le Yu, Bao-Sen Shi, Guo-Ping Guo, Dao-Xin Dai, Xi-Feng Ren, et al. On-chip coherent conversion of photonic quantum entanglement between different degrees of freedom. *Nature communications*, 7:11985, 2016.

[272] Joseph M Lukens and Pavel Lougovski. Frequency-encoded photonic qubits for scalable quantum information processing. *Optica*, 4(1):8–16, 2017.

[273] Bruce E Kane. A silicon-based nuclear spin quantum computer. *nature*, 393(6681):133, 1998.

[274] Paolo Zanardi and Fausto Rossi. Quantum information in semiconductors: Noiseless encoding in a quantum-dot array. *Physical review letters*, 81(21):4752, 1998.

[275] AJ Skinner, ME Davenport, and Bruce E Kane. Hydrogenic spin quantum computing in silicon: a digital approach. *Physical review letters*, 90(8):087901, 2003.

[276] Andrew J Daley, Martin M Boyd, Jun Ye, and Peter Zoller. Quantum computing with alkaline-earth-metal atoms. *Physical review letters*, 101(17):170504, 2008.

[277] Christopher R Moon, Laila S Mattos, Brian K Foster, Gabriel Zeltzer, and Hari C Manoharan. Quantum holographic encoding in a two-dimensional electron gas. *Nature nanotechnology*, 4(3):167, 2009.

[278] Sandra Foletti, Hendrik Bluhm, Diana Mahalu, Vladimir Umansky, and Amir Yacoby. Universal quantum control of two-electron spin quantum bits using dynamic nuclear polarization. *Nature Physics*, 5(12):903, 2009.

[279] R Maurand, X Jehl, D Kotekar-Patil, A Corna, H Bohuslavskyi, R Laviéville, L Hutin, S Barraud, M Vinet, M Sanquer, et al. A cmos silicon spin qubit. *Nature communications*, 7:13575, 2016.

[280] Matthew D Reed, Leonardo DiCarlo, Simon E Nigg, Luyan Sun, Luigi Frunzio, Steven M Girvin, and Robert J Schoelkopf. Realization of three-qubit quantum error correction with superconducting circuits. *Nature*, 482(7385):382, 2012.

[281] Rami Barends, Alireza Shabani, Lucas Lamata, Julian Kelly, Antonio Mezzacapo, Urtzi Las Heras, Ryan Babbush, Austin G Fowler, Brooks Campbell, Yu Chen, et al. Digitized adiabatic quantum computing with a superconducting circuit. *Nature*, 534(7606):222, 2016.

[282] Edo Waks, Kyo Inoue, Charles Santori, David Fattal, Jelena Vuckovic, Glenn S. Solomon, and Yoshihisa Yamamoto. Quantum cryptography with a photon turnstile. *Nature*, 420(6917):762–762, 2002.

[283] W. Pfaff, B. J. Hensen, H. Bernien, S. B. van Dam, M. S. Blok, T. H. Taminiau, M. J. Tiggelman, R. N. Schouten, M. Markham, D. J. Twitchen, and R. Hanson. Unconditional quantum teleportation between distant solid-state quantum bits. *Science*, 345(6196):532–535, 2014.

[284] David D Awschalom, Ronald Hanson, Jörg Wrachtrup, and Brian B Zhou. Quantum technologies with optically interfaced solid-state spins. *Nature Photonics*, 12(9):516, 2018.

[285] S. Etcheverry, G. Cañas, E. S. Gómez, W. A. T. Nogueira, C. Saavedra, G. B. Xavier, and G. Lima. Quantum key distribution session with 16-dimensional photonic states. *Scientific Reports*, 3:2316 EP –, 07 2013.

[286] Emmanuel Candes, Justin Romberg, and Terence Tao. Robust uncertainty principles: Exact signal reconstruction from highly incomplete frequency information. *arXiv preprint math/0409186*, 2004.

[287] David L Donoho et al. Compressed sensing. *IEEE Transactions on information theory*, 52(4):1289–1306, 2006.

[288] E. J. Candes and M. B. Wakin. An introduction to compressive sampling. *IEEE Signal Processing Magazine*, 25(2):21–30, March 2008.

[289] Harald Cramér and Ulf Grenander. *Probability and statistics: the Harald Cramér volume*. Almqvist & Wiksell, 1959.

[290] M. Rani, S. B. Dhok, and R. B. Deshmukh. A systematic review of compressive sensing: Concepts, implementations and applications. *IEEE Access*, 6:4875–4894, 2018.

[291] Chengbo Li, Wotao Yin, Hong Jiang, and Yin Zhang. An efficient augmented lagrangian method with applications to total variation minimization. *Computational Optimization and Applications*, 56(3):507–530, Dec 2013.

[292] Georg Harder, Tim J Bartley, Adriana E Lita, Sae Woo Nam, Thomas Gerrits, and Christine Silberhorn. Single-mode parametric-down-conversion states with 50 photons as a source for mesoscopic quantum optics. *Physical review letters*, 116(14):143601, 2016.

[293] E. C. Paul, M. Hor-Meyll, P. H. Souto Ribeiro, and S. P. Walborn. Measuring spatial correlations of photon pairs by automated raster scanning with spatial light modulators. *Scientific Reports*, 4:5337 EP –, 06 2014.

[294] Daniel J. Lum, Samuel H. Knarr, and John C. Howell. Fast hadamard transforms for compressive sensing of joint systems: measurement of a 3.2 million-dimensional bi-photon probability distribution. *Opt. Express*, 23(21):27636–27649, Oct 2015.

[295] P. Ben Dixon, Gregory A. Howland, James Schneeloch, and John C. Howell. Quantum mutual information capacity for high-dimensional entangled states. *Phys. Rev. Lett.*, 108:143603, Apr 2012.

[296] Gregory A. Howland and John C. Howell. Efficient high-dimensional entanglement imaging with a compressive-sensing double-pixel camera. *Phys. Rev. X*, 3:011013, Feb 2013.

[297] Jonathan Roslund, RennéMedeiros de Araújo, Shifeng Jiang, Claude Fabre, and Nicolas Treps. Wavelength-multiplexed quantum networks with ultrafast frequency combs. *Nature Photonics*, 8:109 EP –, 12 2013.

[298] D. Giovannini, J. Romero, J. Leach, A. Dudley, A. Forbes, and M. J. Padgett. Characterization of high-dimensional entangled systems via mutually unbiased measurements. *Phys. Rev. Lett.*, 110:143601, Apr 2013.

[299] Mohammad Mirhosseini, Omar S. Magaña Loaiza, Seyed Mohammad Hashemi Rafsanjani, and Robert W. Boyd. Compressive direct measurement of the quantum wave function. *Phys. Rev. Lett.*, 113:090402, Aug 2014.

[300] Michael Kues, Christian Reimer, Piotr Roztocki, Luis Romero Cortés, Stefania Sciara, Benjamin Wetzel, Yanbing Zhang, Alfonso Cino, Sai T. Chu, Brent E. Little, David J. Moss, Lucia Caspani, José Azaña, and Roberto Morandotti. On-chip generation of high-dimensional entangled quantum states and their coherent control. *Nature*, 546:622 EP –, 06 2017.

[301] Andreas Christ, Kaisa Laiho, Andreas Eckstein, Thomas Lauckner, Peter J. Mosley, and Christine Silberhorn. Spatial modes in waveguided parametric down-conversion. *Phys. Rev. A*, 80:033829, Sep 2009.

[302] Vipul Rastogi, K. Thyagarajan, M. R. Shenoy, P. Baldi, M. De Micheli, and D. B. Ostrowsky. Modeling of large-bandwidth parametric amplification in the Čerenkov-idler configuration in planar waveguides. *J. Opt. Soc. Am. B*, 14(11):3191–3196, Nov 1997.

[303] D. H. Auston. Subpicosecond electro-optic shock waves. *Applied Physics Letters*, 43(8):713–715, 1983.

[304] P. Mouroulis and J. Macdonald. Geometrical optics optical design. *UK, London: Oxford Univ. Press*, 1997.

[305] John Mallon and Paul F. Whelan. Calibration and removal of lateral chromatic aberration in images. *Pattern Recognition Letters*, 28(1):125 – 135, 2007.